

Discharge ignition, dynamics and chemistry of nanosecond pulsed plasmas in water

Dissertation

zur Erlangung des Grades
"Doktor der Naturwissenschaften"

an der Fakultät für Physik und Astronomie
der Ruhr-Universität Bochum

von Katharina Grosse

aus Witten

Bochum 2020

1. Gutachter: Prof. Dr. Achim von Keudell
2. Gutachter: Prof. Dr. Peter Awakowicz

Datum der Disputation

25. Januar 2021

Contents

1	Introduction	3
1.1	Motivation	3
1.2	Research focus	5
2	Fundamentals	7
2.1	Pulsed discharges in liquids	7
2.1.1	Discharge breakdown phenomena in liquids	8
2.1.2	Discharge propagation in liquids	13
2.1.3	In-liquid chemistry	15
2.2	Characteristics of liquid medium	16
2.2.1	Hydrogen	16
2.2.2	Hydrodynamic phenomena	16
2.3	Emission spectroscopy	19
2.3.1	Fundamental processes	20
2.3.2	Spectral line broadening	20
2.3.3	Continuum spectra	22
3	Experiment, diagnostics and methods	25
3.1	Experimental setup	25
3.1.1	Plasma chamber	25
3.1.2	Nanosecond pulsed plasma source	27
3.1.3	Electromagnetic interference (EMI)	28
3.2	Diagnostics and methods	28
3.2.1	Electrical conductivity	28
3.2.2	Electrical measurements	30
3.2.3	Phase-resolved ICCD imaging	31
3.2.4	Shadowgraphs	32
3.2.5	Optical emission spectroscopy	33
3.2.6	Optical absorption spectroscopy for liquid chemistry analysis	35
3.2.7	Determination of electron density n_e	37

4	Physics of nanosecond pulsed plasmas in distilled water	41
4.1	Electrical discharge properties	41
4.1.1	Pulse shape characteristics	42
4.1.2	Reconstructed pulse at the electrode	47
4.1.3	Dissipated power	49
4.2	Ignition of nanosecond discharge in liquid	50
4.2.1	Field ionisation	50
4.2.2	Electrostrictive forces	54
4.3	Discharge physics and propagation in liquid	55
4.3.1	Primary discharge	56
4.3.2	Re-ignitions and discharge afterglow	78
4.3.3	Electron densities	81
4.4	Cavitation	84
4.4.1	Formation of a cavitation bubble	85
4.4.2	Model I: Cavitation theory	91
4.4.3	Model II: Plasma ignition	99
4.4.4	Combination of model and experiment	100
4.5	Chemistry generated by nanosecond plasma in liquid	103
4.5.1	H ₂ O ₂ production	103
4.5.2	Global chemistry model	105
5	Summary and conclusion	113
6	Outlook	117
	Bibliography	121
	Appendices	
	Appendix A Line broadening calculations	137
	Appendix B Time-resolved emission spectra	139
	Appendix C Global Chemistry Model	143

*“Equipped with his five senses,
man explores the universe around
him and calls the adventure
science.”*

Edwin Powell Hubble

1 | Introduction

1.1 Motivation

Within the universe, over 99% of the visible matter is in the plasma state. The planets which make less than one percent of the visible matter also exhibit plasmas in nature as e.g. the aurora at the poles on earth or as lightning. These plasmas are therefore present within the earths atmosphere but despite that they can also develop in a non-gaseous environment such as liquids.

The earths surface is covered by 71% liquid water and has an essential role for life on earth. In industry, water is used for various applications as for example for energy production in hydroelectric power plants. Today, the challenge of energy storage is a major task since renewable energies such as solar and wind energy are not available 24 hours a day. Hydrogen energy storage is a process in which a surplus of energy from renewable sources is used for running electrolysis resulting in water splitting into hydrogen. The created hydrogen can then be used for many applications as for example for power generation or cleaning natural gas pipelines. Despite that, water and especially hydrogen can also be used in plasma technology for various applications.

The interaction between these two states of matter, plasmas and liquids, has been studied for many years. Discharges above liquids transport the produced chemical species from the atmosphere/gas into the liquid. These plasmas have been used for applications e.g. in the field of plasma medicine for sterilisation of surgical instruments [1, 2]. In contrast, discharges directly initiated inside a liquid environment exhibit many phenomena which favour these plasmas for different applications. Next to the efficient production of radical species such as H_2O_2 , OH and others, UV radiation as well as shock wave formation are observed [3]. This combination of processes enhances the mass transfer of reactive species from the discharge into the liquid. Therefore, liquid treatment or indirect treatment of solid surfaces inside the liquid show enhanced reaction rates of the produced species. This offers a wide range of applications. The most common ones can be divided into three main categories. The use of in-liquid plasmas for *water treatment* is versatile. They are applied in (industrial) wastewater treatment [4–6] and are used for the

decomposition of molecules and materials [7, 8], sterilisation of microorganisms [3], the purification of drinking water through ozone production [9], dye decoloration [10], and plasma electrolysis for hydrogen production [11]. The second field in which in-liquid plasmas are applied is *plasma medicine*. The discharges can destruct and inactivate bacteria [12, 13], can be used for prostate hyperplasia treatment [14] and sterilisation of living tissue [15, 16]. The last main application field is in-liquid *nanoparticle production*, e.g. for the synthesis of silver nanoparticles [17] or carbon nanoparticles [18].

The typical geometry of these discharges is realised by a combination of pin and plane electrodes inside a liquid and a variety of setups has been developed over the past decades accordingly [19]. The study of discharges inside liquids started with Stanley Whitehead, who published his first work on electrical discharges in liquids in 1928 [20]. From then on, especially the processes leading to *discharge breakdown* inside liquids have been discussed intensively. Some of the electrical parameters of the applied voltage pulses seem to govern the ignition process and the underlying physics. Especially the pulse length or more specific its rise time are crucial for the discharge initiation process and are therefore discussed in literature for different setups and applications.

For relatively long rise times of tens of nanoseconds and longer, the liquid has time to react to the negative pressure gradient developing from the high electric field strength resulting in electrostriction [21]. Therefore, cavitation and bubble formation set in due to the gradient in pressure and also local heating can occur resulting from the flowing current. The plasma is then developing inside this previously formed bubble. For shorter rise times, the hydrodynamic response of the liquid is too slow and no cavitation bubble is formed before discharge initiation [22]. However, it has been reported by Jones and Kunhardt [23] that an ignition in a purely liquid phase due to electron collision ionisation is improbable. The close coupling of electrons and the phonon modes of the liquid are assumed to efficiently dissipate any energy the electrons would gain by acceleration in the electric field. Therefore, any kind of vapour phase or nucleation on a small scale must be present in order for ignition to occur inside dielectric liquids.

In 2003, T.J. Lewis [24] first proposed the generation of low-density microcavities on electrode surfaces due to a reduction of interfacial tension for pulsed discharges in dielectric liquids in general. This idea has been further extended to the creation of a low-density region around the electrode for nanosecond pulsed plasmas with short rise times. Nanocavities or nanopores are formed in this region due to a rupture of the liquid [21, 22, 25–28]. The rupture of the liquid is induced by a negative pressure gradient resulting from the high electric field strength [29, 30]. Kolb et al. [31] discussed in detail different field effects induced by the high electric field applied in these

discharge setups as discharge and streamer initiation mechanisms. Next to the influence of the applied voltage, the pulse length and the pulse rise time, other parameters such as the electrode material, the liquid and its conductivity are important to describe the initiation of the streamers and the ignition of the discharge [31].

Despite all the intense discussions concerning the ignition of in-liquid discharges, it is challenging to compare the different proposed ignition mechanisms due to varying setups and liquids used by different researcher groups. In order to get a full view of one of the more recent discussed setups (pin-to-pin electrode configuration inside distilled water), this thesis is dealing with the ignition, streamer propagation, production of chemical species and their interaction with surfaces possibly relevant for CO₂ reduction. Only with a full understanding of the setup and the influence of each parameter on the physical and chemical processes, the industrial application of these plasmas is possible and reasonable.

1.2 Research focus

As already mentioned, the observation of discharges in liquids are investigated intensively. During the last two decades, these discharges gained more interest in association with challenges of our modern society. Especially, the use of these plasmas in the fields of water purification or CO₂ reduction are discussed. The pollution of water by antibiotics or other pharmaceuticals [32] needs to be approached as well as the increasing CO₂ concentration in the atmosphere by e.g. global traffic. For the latter, CO₂ reduction by plasma electrolysis in combination with catalysis is proposed and could be a promising candidate to split CO₂ into useful chemicals such as ethanol.

In order to address these challenges, discharges in liquids need to be fully understood from its ignition to its final chemical products within the liquid. Therefore, the following main research questions are addressed in this thesis:

1. *Which physical processes cause ignition of a high voltage, nanosecond pulsed discharge in a liquid environment?*

The ignition process is crucial for the following chemical reactions and the interaction between discharge and liquid. If the ignition is appearing inside pre-formed gas bubbles on a nano scale (*nanovoids*), the chemistry is different than for a discharge ignited directly inside the liquid. The latter leads to aqueous electrons and higher mass transport of chemical species.

2. *How is the discharge propagating inside the liquid medium and how is this correlating with the chemical species created by the plasma?*

The evolution of the in-liquid discharge is also influencing the chemistry. Especially the lifetime of the propagating discharge is affecting the liquid chemistry, as a longer living plasma is producing more radical species inside the liquid. The created chemical species can be used for indirect surface treatment by placing materials inside the liquid. But to do so, the chemical species need to be identified to discuss possible surface reactions and their use.

2 | Fundamentals

Various types of discharges in liquids were established over the last decades for different purposes. The different setups and their use are described in section 2.1. Furthermore, the ignition inside the liquid is widely discussed in literature and various ignition mechanisms are postulated. In addition, the combination of the discharge physics and the surrounding liquid leads to various chemical reactions. The liquid environment is as important as the discharge itself to influence the evolution of the discharge and is therefore addressed in section 2.2. The observation of the discharge inside the liquid is mainly performed via optical emission spectroscopy, wherefore spectroscopy itself is discussed in detail in section 2.3.

2.1 Pulsed discharges in liquids

There are two main concepts for plasma generation inside a liquid medium. Those concepts were classified by Bruggeman and Leys as (i) *direct liquid phase discharges* and (ii) *discharges in bubbles in liquids* [19]. For both cases, two electrodes are immersed into a liquid container and either gas is bubbled into the liquid to act as an ignition medium or the discharge is directly ignited inside the liquid medium without the presence of gas bubbles. In both cases, electrode configurations of combinations of pin and plane electrodes for the powered and grounded side can be used. A variety of pin-to-pin, plane-to-plane, and pin-to-plane configurations are used in literature, but the latter is the most used electrode assembly [3, 30, 33–36]. A further distinction of direct liquid discharges is depending on the discharge expansion, which either reaches the grounded electrode (*spark* or *arc discharge*) or vanishes before reaching it (*corona* or *streamer-like discharge*).

The setup with immersed gas bubbles inside the liquid can be used with longer voltage pulses in the range of hundreds of nanoseconds as the breakdown inside the gas is faster than directly inside the liquid. Gases are less dense than liquids and electrons can therefore gain higher energies through acceleration in the electric field in a gaseous environment, which therefore can lead to breakdown through electron multiplication. Furthermore, lower voltage amplitudes are necessary for ignition. In comparison to that, the discharges generated without gas bubbles inside a static liquid environment

require very short voltage pulse rise times in the order of a few nanoseconds for the discharge to ignite. Additionally, the powered electrode tip needs to be very sharp to reach high electric field strength in the order of >30 MV/cm [29] which are necessary for ignition. Kolb et al. [31] even estimated lower critical electric field strength of 10-20 MV/cm.

In the case of longer voltage rise times, the discharge can ignite inside the discharge cell. Instead of an ignition directly inside the liquid, gas bubbles form due to vapourisation induced by Joule heating and the discharge is then igniting inside these pre-formed bubbles. Therefore, in the following, the direct liquid phase discharges will be denoted as ignited ‘*directly inside liquid*’.

The short pulses used for discharge ignition directly inside the liquid are usually created by high voltage (HV) nanosecond pulse generators. In literature, mostly HV nanosecond pulsers from FID GmbH are used [29, 30, 36–38], although self-made pulsers based on Blumlein generators are also found [39]. The pulsing system is relevant to compare results from different research groups because small changes in e.g. the voltage pulse rising time or waveform can have a great impact on the observed physics. This will be discussed in section 4.1.

The process of discharge ignition directly inside liquids is widely discussed in literature. Different ignition mechanisms are possible and it is often accepted that the discharge develops inside liquid ruptures - so-called *nanovoids* - generated by a negative pressure gradient induced by the high electric field. Nevertheless, there is no clear experimental evidence for that hypothesis. Furthermore, this theory only describes the ignition by electron multiplication but not the source of the initial electrons starting the initiation process.

2.1.1 Discharge breakdown phenomena in liquids

Discharge breakdown in liquids has been discussed intensively since the first work on discharges in liquids in 1928. There are many processes and mechanisms which can describe the ignition of a discharge inside a liquid. The ignition of nanosecond pulsed plasmas is difficult to monitor due to the short time scale of picoseconds and therefore no experimental evidence of the initiation process of these plasmas has been made. However, there are several theoretical studies discussing different ignition mechanisms and all processes which could lead to ignition of plasmas in liquids in general are presented in the following.

(i) Ignition through bubbles or nanovoids

The ignition of discharges in liquids with DC or AC excitation leads to Joule heating and water vapour formation. The resulting bubble acts as ignition site [19]. For nanosecond pulsed discharges, the time scale is in general too short to form such a vapour bubble [40].

In liquid media it is assumed that there are small impurities or gas bubbles on the micro- or nanoscale present unless it is degassed. These small bubbles are possible ignition sites. In recent literature it is generally accepted that these so-called nanovoids act as ignition sites for HV nanosecond pulsed plasmas. The first report about nanovoids (or microcavities) leading to ignition of streamer discharges in liquids was made by T.J. Lewis [24]. He argued that the processes of field electron emission and nanovoid formation are both necessary for ignition to occur. Furthermore, he discussed the formation of a double layer at the electrode surfaces. The double layer appearance is also reported in the field of electrochemistry [41]. The surface tension at anode and cathode is influenced with increasing applied voltage. Therefore, the lateral cohesion of the liquid at the electrode-liquid interface is influenced and the resulting non-uniformity in interfacial tension is leading to low-density regions. In these regions, nanovoids form according to the electrostriction mechanism [22, 30, 42]. Electrostriction describes the deformation of dielectric materials under the application of an electric field. In the case of water, positive ions will be displaced in electric field direction.

For electric fields with fast rise time, it was shown that the hydrodynamic forces of the fluid are too slow to counteract the fast pressure increase [22, 25]. The total pressure in the electrode vicinity is negative according to [30]:

$$P_{tot} = P_{hydr} - P_{electr} = P_{hydr} - \rho\epsilon_0 \left(\frac{\delta\epsilon}{\delta\rho} \right) E^2, \quad (2.1)$$

with the hydrodynamic pressure P_{hydr} , the electric field E , the liquid dielectric constant ϵ and the density of the liquid ρ . For water with an dielectric constant $\epsilon=81$, a critical negative pressure of -20...-30 MPa leads to a rupture of the fluid close to the electrode [30].

The strong electric field is elongating these nanovoids parallel to the applied field [43, 44]. Electrons which are then created by other effects could be accelerated inside these nanovoids and cause ionisation.

Nanovoid formation requires a minimum critical pressure and a small radius of the tip electrode which is usually in the range of a few μm [42]. This negative pressure zone is surrounded by a compression layer induced by the hydrodynamic forces pushing the liquid towards the tip electrode because of a pressure imbalance.

(ii) Ignition through field effects

The high electric field implies the occurrence of field effects at the different interfaces of solid electrode, liquid medium and gaseous-like nanovoids/bubbles. There are different field effects which are first brought together into context of in-liquid discharge ignition by Kolb et al. [31]. In general, the high applied electric field strength leads to a distortion of the electrical potential. The following processes can result from that:

Electron field emission: Electron field emission is also known as field emission and Fowler-Nordheim tunneling. R.H. Fowler and L.W. Nordheim proposed the theory of field emission from bulk materials in 1928 [45]. This concept describes the tunneling of electrons from bulk metals to other solid materials. However, in 1972 Robert Gomer first applied this theory to the tunneling of electrons from a metal into a liquid [46]. The general idea is that a metal can be described as a potential well containing free electrons. The highest level filled with electrons E_F ('Fermi level') lies several electron volts below the vacuum level. The difference between Fermi-level and vacuum is called work function Φ . This is illustrated in figure 2.1.1(a). Electrons need to be excited above this energy barrier in order for thermionic emission to appear. In the presence of a strong electric field due to a negative applied voltage, this barrier is deformed and electrons can tunnel through the resulting potential barrier. This is visualised in figure 2.1.1(b).

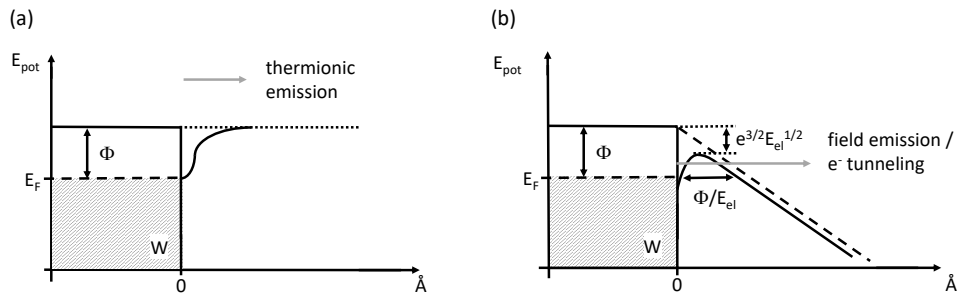


Figure 2.1.1: Potential energy for electrons at a tungsten (W) surface (a) without and (b) with an applied electric field. E_F is the Fermi level of the material and Φ the work function (4.55 eV for tungsten). Adapted from [46].

The relation between current and the applied electric field is described by the Fowler-Nordheim equation which can be simplified to

$$I \propto \exp\left(-\frac{4}{3}\left(\frac{2m}{\hbar^2}\right)^{1/2}\Phi^{3/2} \cdot E^{-1}\right), \quad (2.2)$$

with the work function Φ in eV and the electric field strength E in $\text{V}/\text{\AA}$. For practical purposes the equation is quantified to:

$$I \propto \exp\left(-0.68 \cdot \Phi^{3/2} \cdot E^{-1}\right). \quad (2.3)$$

To reach a current which is large enough, the electric field must be high. This can be achieved by reducing the electrode tip radius r_t which relates to the electric field strength approximately like [46]:

$$E_t \sim \frac{U}{5r_t}. \quad (2.4)$$

Gomer reported that emission from a metal tungsten surface with a work function $\Phi=4.5-5.5$ eV can only occur when electric fields $0.3-0.6$ V/Å are applied [46]. However, for tungsten in hydrogen it was observed that the work function of the metal changes when a liquid layer is surrounding the electrode [47, 48]. In the following, tungsten is always taken as the electrode material to better compare it with the experiments presented later in chapter 4.

Electron initiated Auger process: Electron initiated Auger processes are mentioned to be a possible result from field electron emission by Kolb et al. [31]. This process describes the quick trapping of emitted electrons by the molecules close to the emitting surface due to the relatively short lifetimes of the electrons in liquids. The energy left from the captured electron can be absorbed by other electrons in excited energy levels. Therefore, this could lead to the release of two or more electrons from a molecule. After the release of the electrons, a positive ion in the electrode tip vicinity is left behind and the electrons move away from a negatively charged electrode surface.

Field ionisation: Field ionisation works similar as field emission but with a positive applied electric field. But in this case the electrons from molecules or atoms inside the liquid are tunnelling through the liquid medium into a positively charged metal electrode. Therefore, the electrons must enter the metal electrode above the Fermi level E_F .

In figure 2.1.2(a) the electric potential of a H₂O molecule is illustrated in the presence of an electric field of 2 V/Å. A tungsten electrode is immersed into water influencing the tunnel probability from the water molecule in figure 2.1.2(b).

The image potential V_{im} is included in E_W and describes a correction term which modifies the potential step at the surface by $V_{im} = -e^2/(4r)$ with the distance r in Å. This term corresponds to a decrease in binding energy of any electron in the observed atom or molecule by this image potential.

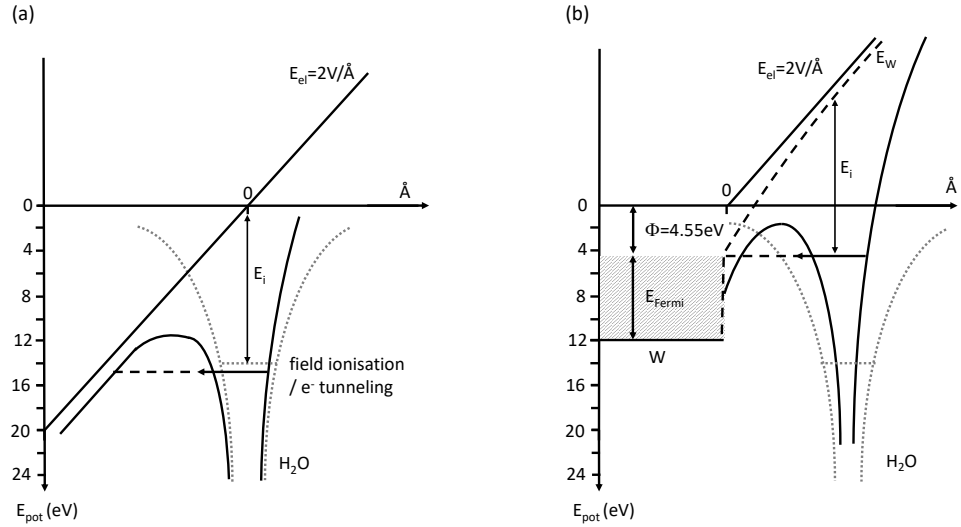


Figure 2.1.2: Potential energy diagram for H_2O in the presence of an electric field with $E_{el}=2\text{ V}/\text{\AA}$ (a) without and (b) with a metal electrode inside the liquid medium. E_i is the ionisation energy, E_F is the Fermi level of the material, E_W is the sum of applied and image potential and Φ the work function (4.55 eV for tungsten). The dotted lines describes the undisturbed electrical potential of the H_2O molecule and the solid lines mark the electrical potential of the H_2O molecule by the influence of the electric field E_{el} . Adapted from [46].

The threshold for field ionisation of H_2O at a tungsten tip was investigated by W. A. Schmidt [49]. He found fields of $0.2\text{ V}/\text{\AA}$ and $0.3\text{ V}/\text{\AA}$, leading to ionisation probabilities of 1% and 5%, respectively. Later, the tunneling fields for H_2 were given to be typically $0.7\text{ V}/\text{\AA}$ [46]. When the threshold is reached, the tunneling of electrons from e.g. a water molecule to a metal surface is possible. Therefore, a layer of positive water ions is left close to the metal electrode surface.

Field-assisted molecular dissociation: Field-assisted molecular dissociation is also known as Zener breakdown in semiconductor physics. This process leads to charge transfer between molecules or atoms and metallic electrodes. In the presence of a high electric field, the electronic wavefunctions and energy eigenvalues of atoms and molecules at the liquid-electrode interface can shift. This can lead to a shift of a bonding molecular orbital above the anti-bonding molecular orbital of a neighbouring molecule or atom. Therefore, field-driven electronic transitions from one molecule into the anti-bonding orbital of a neighbouring molecule or atom are possible leading to molecular dissociation.

In the vicinity of electrodes at high electric fields, it is likely that all of those effects appear, depending on the pulse polarity. The dielectric strength of dis-

tilled H₂O is high so that an electric field of 65-70 MV/m (0.0065-0.007 V/Å) at atmospheric pressure is necessary for an electrical breakdown to occur under pulsed conditions (<μs) [50, 51], but can be as low as 30 MV/m (0.003 V/Å) for different pressures and non-distilled water. Longer pulses result in lower breakdown fields.

2.1.2 Discharge propagation in liquids

The discharge can propagate in different forms through the liquid medium. There are several descriptions found in literature such as corona, streamer, spark, and arc discharges in liquids. The exact meaning of these discharge types can be described as follows.

Corona/corona-like discharge: In general, a corona discharge describes a conductive area induced by electric breakdown of a fluid through an inhomogeneous electric field. Current can flow continuously from the electrode into the fluid when the threshold of dielectric strength of the fluid is reached. The opposite electrode is far away so that no conductive channel can form between the two electrodes. Depending on the polarity of the applied voltage, *positive* or *negative corona* discharges form which are behaving differently. Positive corona discharges are observed as uniform plasmas around the electrode resulting in low electron densities. Negative corona discharges show a longer propagation into the fluid next to higher electron densities.

Streamer/streamer-like discharge: Streamer discharges are similarly induced as corona discharges. A high voltage applied to an electrode results in discharge breakdown inside the surrounding fluid. But in comparison to corona discharges, streamer discharges have a transient/short lived nature and propagate in long filamentary structures.

Spark discharge: A spark is created when a conductive channel forms at an electrode (e.g. during corona or streamer discharges) and reaches the counter electrode. The ionised and conductive channel created by a high electric field applied to the electrode is usually developing in insulating media such as gases or liquids. Sparks are short lived discharges.

Arc discharge: In the case of a spark discharge with continuously supplied current, the discharge forms into an arc discharge.

The most common descriptions for discharges in liquids are corona or streamer discharges, whereas spark discharges are only mentioned and studied by a few groups [52, 53]. The pulsing of HV plasmas in liquids makes it difficult to distinguish between a corona-like and streamer-like behaviour wherefore both terms are found in literature [37, 54–59]. In the following text, the term *streamer discharge* will be used according to the short lifetimes of these

discharges in general. In liquid environments, the discharge propagation is believed to occur in a similar manner than streamer discharges in gases. In general, a streamer is induced by electron multiplication inside a gas. A local electric field is forming at the so-called *streamer head* which is high enough to ionise the surrounding gas.

After the ignition inside the liquid, it is assumed that a streamer is propagating through the gaseous-like medium of the nanopores. Simultaneously, the streamer is ionising the surrounding species at its head (*streamer head*). The streamer propagation for in-liquid discharges can be divided into four phases following the voltage curve, as proposed by Seepersad et al. [30] for positive applied HV pulses:

Initiation: The discharge is initiated due to the presence of a high electric field resulting from a sharp electrode tip and an applied high voltage pulse.

Propagation: In case of a positive applied voltage pulse, the positive ions at the streamer head lead to a local electric field driving the propagation of the streamer through the liquid. With further propagation, the positive charge in the discharge channel increases. This process continues until the voltage pulse reaches a plateau phase resulting in $dV/dt = 0$.

Screening and extinguishing: When a voltage plateau is reached and the ionisation at the streamer head stops, the positive charge is compensated by a radial electron current resulting from a reverse radial electric field. Additionally, the axial electron current inside the discharge channel decreases. Therefore, the streamer head potential decreases and the discharge is likely to extinguish.

Restrike: The discharge is able to ignite again after the voltage pulse plateau during the falling edge of the voltage pulse. The positive space charge formed during the first ignition leads to an electric field which is strong enough to ignite the plasma inside the pre-ionised channels from the first streamers.

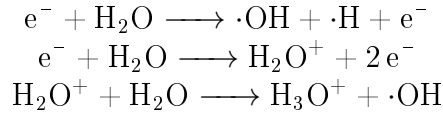
In case of negative applied HV pulses it is argued in [30] that the initiation mechanism is induced by secondary electron emission from the powered electrode and that the discharge propagation behaves similar to a Townsend breakdown mechanism.

The propagation phase of the discharge is usually characterised by many streamers evolving simultaneously. Therefore, bush-like or tree-like structures are observed for discharges in liquids [29, 34, 59, 60]. The velocity of the streamers varies for the different discharges. The following values for streamer velocities are reported: 2.5 km/s during the initial phase, 35 km/s

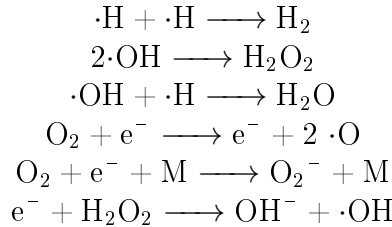
during the restrike (40 ns rise time, 18 kV applied voltage) [34], 5000 km/s (150 ps rise time, 112 kV applied voltage) [29], 3 km/s during bush-like mode, 10-60 km/s during tree-like mode (5 ns rise time, 1.5-9 kV applied voltage) [60, 61] and 200 km/s (fast rise time, 70 kV applied voltage) [59]. The velocity of the streamers seems to be influenced by both, the applied voltage and the rise time of the voltage pulse. The setups themselves are roughly comparable as in each of them distilled/de-ionised water is used and sharp tip electrodes with tip radius curvatures of about 50 μm are mounted.

2.1.3 In-liquid chemistry

The direct ignition of a discharge inside a liquid generates many chemical species inside the expanding streamer channels and the surrounding liquid. The water molecules can be dissociated or ionised by electron collisions, which are produced during ignition. The electron energies are high enough so that the dissociation and ionisation energies of H_2O can be exceeded [62, 63]. Therefore, the following primary reactions are expected [64–66]:



From these primary reactions, secondary ones can follow according to the reaction of the generated radicals ($\cdot\text{X}$) with each other [8, 65]:



Here, M describes a third collisional partner e.g. O_2 within the liquid [8]. In theory, many reactive species such as OH and H_2O_2 are created. These species can be used e.g. for water purification [8]. Pulsed corona discharges in liquids are found to produce high removal efficiencies above 90% for pollutants such as methyl orange, phenol and 4-chlorophenol [65]. The energy yield of H_2O_2 for in-liquid pulsed discharges is found to be between 23.1 mmol/(1-kWh) [67] and 34.1 mmol/(1-kWh) [68].

Nevertheless, it is challenging to monitor the generation of short-lived chemical species such as OH but also longer lived species as H_2O_2 for nanosecond pulsed plasmas. In general, only indirect measurement techniques like optical absorption spectroscopy can be applied for these short discharges. Therefore, Mededovic and Locke [69] developed a model to describe the primary chemical processes induced by spark discharges in water. They distinguish between a hot *core* and a *recombination region*. The latter is the main production

zone of H_2O_2 whereas the *core region* enables the majority of molecular hydrogen and hydroxyl radical production and about 47% of molecular oxygen formation. However, this model was developed for spark discharges in liquids which differ from corona and streamer discharges in liquids. Chauvet et al. [70] attempted to convert this model to streamer-like discharges in water and reported a product efficiency of H_2O_2 of 2 g/kWh. Nevertheless, a detailed experimental study of the possible products is necessary to understand the exact reaction pathways for these in-liquid discharges.

2.2 Characteristics of liquid medium

In-liquid discharges are mostly ignited inside distilled, de-ionised water with low electrical conductivity of a few $\mu\text{S}/\text{cm}$. In most reports in literature, the liquid is not degassed. However, current research by Simek et al. [38] shows that a pre-degassing of the liquid medium increases the emission intensity of the H_α line. The liquid medium is influencing both, the discharge and the resulting chemistry. Therefore, water as a liquid medium is discussed in detail as well as general hydrodynamic processes and cavitation.

2.2.1 Hydrogen

During the discharges in distilled water, atomic hydrogen is produced. The atom can get excited inside the liquid environment by low-energetic electrons which results in line emission during relaxation of the atom. The first spectral lines in the visible range of hydrogen are described as the Balmer-series. This series reflects the optical transitions of electrons from higher levels to the second lowest energy level $n=2$. The transitions from different higher levels to $n=2$ of the Balmer series are denoted as H_α ($3 \rightarrow 2$, 656 nm), H_β ($4 \rightarrow 2$, 486 nm), H_γ ($5 \rightarrow 2$, 434 nm) and so forth. The transitions to other levels such as $n=1$ (Lyman-series) or $n=3$ (Paschen-series) are not within the visible spectrum.

2.2.2 Hydrodynamic phenomena

Two important hydrodynamic phenomena can occur for the discharges in liquids, namely cavitation and the emission of acoustic or shock waves. Both are described in more detail here.

Cavitation

Cavitation describes the rapid change of pressure inside a liquid, leading to the formation of small gaseous cavities or bubbles. The process of cavitation usually comprises vaporisation, bubble generation and bubble collapse.

The initial evaporation of a cavitation inside a liquid can be induced by different methods, such as laser irradiation (*optic cavitation*) or the application of an electric field. Figure 2.2.1 illustrates the cavitation process induced by an electric field.

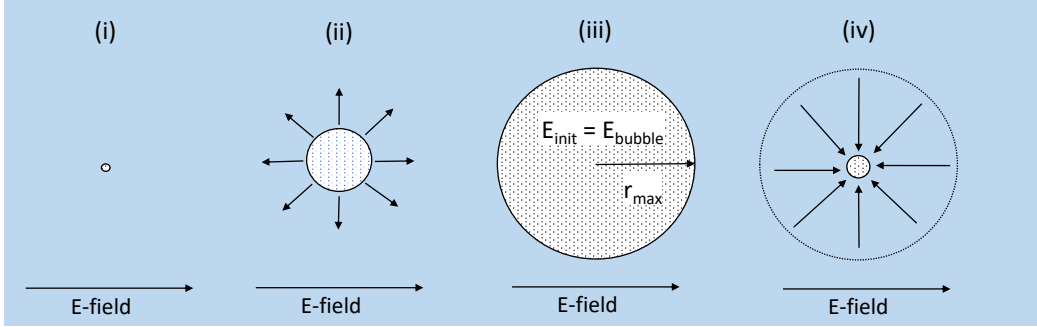


Figure 2.2.1: Sketch of cavitation bubble formation inside a liquid under the influence of an applied electric field.

- (i) *Evaporation*: The applied electric field leads to a re-orientation of the liquid molecules according to its direction. For liquid H_2O , the electric field leads to a strong polarisation of the water molecule and its natural dipole is enhanced by the electric field. This deformation of water as a dielectric medium under the influence of an applied electric field is called *electrostriction*. The electrostriction leads to a pressure difference inside the liquid resulting in evaporation. The evaporated area is called *cavitation nucleus*.
- (ii) *Bubble generation*: The cavitation nucleus starts to grow, either due to adiabatic expansion or evaporation.
- (iii) *Maximum bubble size*: The maximum bubble size is reached when the initial kinetic energy E_{kin} equals the potential energy of the bubble $E_{\text{pot}} = p_{\text{liquid}}V_{\text{bubble}}$, with the liquid pressure p_{liquid} and bubble volume V_{bubble} .
- (iv) *Bubble collapse*: The collapse of the bubble is initiated either by compression due to surface tension or condensation until the bubble reaches a minimum size. The gas inside the bubble can dissipate now inside the surrounding liquid.

Dular and Coutier [71] defined two possible leading processes for the bubble growth (evaporation and expansion) and the bubble collapse (condensation and compression). An estimation of the leading processes can be done by comparing the characteristic time of heat transfer at the bubble interface Δt_r with the bubble lifetime t_{bubble} . This leads to two cases:

$t_{bubble} \gg \Delta t_r$: There is enough time for heat transfer to proceed until thermal equilibrium is reached. The evaporation and condensation of water and water vapour are the main driving mechanisms (isothermal conditions).

$t_{bubble} \ll \Delta t_r$: The bubble evolution is mainly driven by expansion and compression (adiabatic conditions).

The characteristic time of heat transfer is deduced from the energy balance of the gas inside the bubble. Dular and Coutier [71] assumed therefore that the initial bubble is exposed to a pressure drop during the time Δt which leads to a bubble growth from R to $R + \Delta R$ and a temperature change inside the bubble of ΔT :

$$\left(\frac{4}{3}\pi R^3\right)\rho_g c_{vg}\Delta T = \Delta Q - p(4\pi R^2\Delta R), \quad (2.5)$$

with the gas density ρ_g and the specific heat c_{vg} of a constant gas volume inside the bubble, the heat ΔQ the bubble received from the liquid, and the pressure p at the bubble-liquid interface. This energy balance neglects the terms for the kinetic energy and the energy of bubble deformation.

The temperature of the gas inside the bubble changes during the growth process which leads to the formation of a thermal boundary layer around the bubble interfacing the liquid. The resulting temperature gradient inside this boundary layer leads to heat transfer by conduction. Therefore, the heat ΔQ is driven to the bubble. The characteristic time for this heat transfer process can be described as:

$$\Delta t_r = \frac{(\rho_g c_{vg} R)^2}{9\lambda_l \rho_l c_{pl}}, \quad (2.6)$$

with the thermal conductivity of the liquid λ_l , the liquid density ρ_l and the heat capacity of the liquid c_{pl} for constant pressure with the assumption that the temperature variation inside the bubble is only driven by heat exchanges. In the case of water and water vapour with $\rho_g = 0.0173 \text{ kg/m}^3$, $c_{vg} = 717 \text{ J/(kg}\cdot\text{K)}$, $\lambda_l = 0.653 \text{ W/(m}\cdot\text{K)}$, $\rho_l = 999 \text{ kg/m}^3$ and $c_{pl} = 4182 \text{ J/(kg}\cdot\text{K)}$ at 20°C , equation 2.6 is simplifying to:

$$\Delta t_r = 6.2665 \cdot 10^{-6} R^2. \quad (2.7)$$

Already in 1917, Rayleigh [72] discussed the temporal evolution of a small cavity with vacuum inside in an incompressible liquid. The description of the bubble radius $R(t)$ by Rayleigh has been extended later for compressible liquids. This is done with respect to a changing bubble radius \dot{R} propagating at lower velocities than the speed of sound of the liquid medium C and including surface tension which leads to the Rayleigh-Plesset equation describing the bubble wall [73–77]:

$$R\ddot{R}\left(1 - \frac{\dot{R}}{C}\right) + \frac{3}{2}\dot{R}^2\left(1 - \frac{\dot{R}}{3C}\right) = h\left(1 + \frac{\dot{R}}{C}\right) + \left(1 - \frac{\dot{R}}{C}\right)\frac{R}{C}\dot{h}, \quad (2.8)$$

with the enthalpy h at the bubble wall, describing both the internal energy of the bubble and the product of pressure and volume. The pressure term includes the surface tension of the bubble.

It is assumed that the bubble is surrounded by an infinite amount of liquid. In the calculations according to equation 2.8, the bubble is oscillating and expansion and collapse are alternating. This oscillation can be suppressed by including condensation at the bubble wall into the calculations.

Waves

The direct liquid discharge initiation by HV pulses is capable of producing waves inside the liquid medium. In general, it can be divided into two different wave types with different velocities:

Acoustic wave: An acoustic wave is a sound wave propagating through a medium with an acoustic velocity, which is specific for the respective medium (speed of sound). Energy is transported via adiabatic compression and decompression during the propagation. It is sometimes referred to as *pressure wave*.

Shock wave: A shock wave propagates inside a medium faster than its local speed of sound. The local pressure, temperature and density of the medium changes at the shock wave front. Furthermore, the energy of the shock wave is preserved but the entropy is increasing in time.

The speed of sound in water at a temperature of 23°C is 1491.5 m/s [78]. In literature, both shock wave and acoustic wave velocities were observed for waves generated by discharges directly ignited inside liquids [61, 79, 80]. It is reported that a shock wave is formed during ignition which is later relaxing into an acoustic wave [61, 80].

2.3 Emission spectroscopy

The intensity of light emission of short-pulsed discharges in liquids is strong which makes it suitable for spectroscopy measurements. The fundamental processes leading to light emission are discussed in section 2.3.1. Spectral emission lines can be broadened due to different physical mechanisms. The analysis of spectral lines, especially the full width at half maximum (FWHM) gives insight into the density of electrons inside the plasma for broadened lines. The most common broadening mechanisms are described in the following section 2.3.2. Furthermore, continuous radiation can contribute to emission. The different possible generation mechanism of this continuum radiation are discussed in section 2.3.3.

2.3.1 Fundamental processes

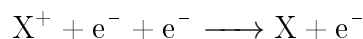
Excitation and de-excitation

An atom or molecule can be excited by energetic electrons (*electron excitation*). Those free electrons can collide with the atom or molecule and transfer energy, which needs to be lower than the ionisation energy in order to excite the particle. Therefore, a bound electron reaches a higher level and the atom/molecule is excited. The de-excitation of the atom/molecule to a lower level occurs under the emission of light with a wavelength according to the energy difference of the two levels (*electron relaxation*). This light can then be detected and analysed.

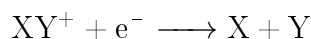
Ionisation and recombination

The collision of a free electron or another particle with an atom or molecule leads to energy transfer. When this energy is higher than the ionisation energy of the colliding partner, the atom or molecule gets ionised. The recombination of the ion with an electron can occur via different recombination mechanisms:

Three-body recombination: A positive ion is colliding with two electrons at the same time. One of the electrons is recombining with the ion during this process and the released binding energy is transported away with the second electron.



Dissociative recombination: When a molecular ion is colliding with an electron, two neutral atoms can be produced according to:



Radiative recombination: In case of an ion recombining with an electron through collision, energy can be set free in form of a photon.



This recombination mechanism can be observed with spectroscopic methods.

2.3.2 Spectral line broadening

When an atom or ion is excited and relaxes, it emits light with the energy $E = h\nu$ which is characteristic for each element and each transition. The distance between the discrete levels is different for each element and therefore elements can be correlated to light emission with specific wavelengths

and hence emission spectra. These discrete emission lines have a natural broadening due to the uncertainty principle which is negligible in most cases according to Griem [81].

In general, the emission line reflects the light emitted from one transition within a particle. But the emission line can be influenced by more than just the type of emitting particle. By taking into account all other particles present in the surrounding (perturbers), the broadening of the spectral line can further be explained by pressure broadening. Pressure broadening comprises three different broadening mechanisms, namely *resonance broadening*, *van der Waals broadening* and *Stark broadening*.

Resonance broadening describes the broadening of a spectral line induced by a perturber particle which is identical to the emitter particle. Therefore, it is possible for an energy exchange to occur. The acting van der Waals forces of the perturber particles on the emitting particle lead to a broadening of the spectral lines which is called *Van der Waals broadening*. The interaction of the emitter particle with the electric field of a charged perturber particle is described by *Stark broadening*. Due to the presence of the electric field, the spectral lines of the emitting particle get shifted and splitted. The Stark broadening is directly associated with the electron density which therefore can be used to determine this parameter.

Additional to pressure broadening, there can be different other broadening mechanisms. The (thermal) Doppler effect resulting from the velocities of the emitting particles with respect to the observer also leads to a broadening of spectral lines (*Doppler broadening*). The distribution of velocities assigns an emitted photon to be either red- or blue-shifted by the Doppler effect, depending on the velocity relative to the observer. The *instrumental broadening* of spectral lines is simply generated by the influence of the experimental setup with all its components.

Aside from these local broadening mechanisms, there is one non-local process which needs to be considered. As the name *opacity broadening* indicates, it is related to the optical depth or thickness τ of the plasma with:

$$\tau(f) = \int_0^d \alpha(x, f) dx. \quad (2.9)$$

The optical depth varies for different frequencies f and is calculated by integrating the absorption coefficient α over the distance d which needs to be surpassed by the emitted light. For a homogeneous plasma equation 2.9 simplifies to:

$$\tau = n \cdot \sigma \cdot d, \quad (2.10)$$

with the particle density n along the optical path d and the cross section σ . A plasma is *optically thick* for $\tau \gg 1$ and *optically thin* for $\tau \ll 1$. The

optical depth of a plasma describes its transparency which is influenced by the number of absorbing species inside the discharge along the optical path. The higher the number of absorbing particles along the optical path, the thicker the optical depth.

According to this, emitted photons during one transition within the discharge may be reabsorbed along the optical path. The absorbing particles may be the very same species which emitted the photons. The reabsorption of photons leads then to the so-called self- or line reversal of an emission line. This influences mostly the center of the emission line. The photons at the center of an emission line have a higher reabsorption probability than the photons at the wings of the line. This effect can generate a dip in intensity at the central position of the emission line (line reversal).

2.3.3 Continuum spectra

In comparison to discrete emission lines, also continuum radiation can be found in emission spectra. These continuum spectra can originate from different mechanisms, which are described below.

(i) Broadened spectral lines

Emission lines can be significantly broadened due to the different mechanisms described in section 2.3.2. Especially Stark broadening can contribute to the overall line broadening at very high electron densities. In addition, emission line profiles can be modified due to self-absorption causing a reversal of the center of the line [82]. The wings of the broadened emission lines can overlap with neighbouring broadened lines and therefore a contribution to the overall continuous spectrum can be made.

(ii) Line emission from molecules

In a similar manner to broadened spectral lines, molecular line series can also be broadened. In general, they extend over a wide spectral range which makes it challenging to identify individual broadened lines.

(iii) Continuum emission from molecules

Continuous emission can also originate from radiative dissociation continua which result from spontaneous radiative dissociation. This describes the decay of the discrete vibrational level of an excited electronic state (X_2^*) into the vibrational continuum of electronic state under the emission of a photon which can be observed for example in the interstellar medium [83]:



In laboratory plasmas, emission from molecular transitions such as the radiative dissociation continuum of H_2^* ($a^3\Sigma_g^+ \rightarrow b^3\Sigma_u^+$) can contribute to the overall continuum spectrum. This continuum contribution depicts the transition from an upper bound state to the lower dissociative state. Lavrov et al. [84] discussed about this continuum for non-equilibrium hydrogen capillary-arc and $\text{H}_2:\text{Ar}$ microwave discharges. In addition, Fantz et al. [85] investigated this radiative dissociation continuum for a low-pressure ECR plasma and compared experiment with a model. Both groups predicted the continuum emission by calculations which include several vibrational levels. This specific continuum is limited to a wavelength range between 180 nm to 400 nm.

(iv) Continuum emission from free-free and free-bound radiation

Free-bound radiative transitions describe the capture of a free electron by an ion (2-body recombination). The probability of this recombination increases with increasing pressure present in the discharge. High pressures have been measured for in liquid discharges in the GPa range [60, 86]. In comparison, free-free radiation is created by the change of momentum of an electron during e.g. a collision with an ion or a neutral atom or molecule (Bremsstrahlung). The radiation resulting from these transitions can be described by an emission coefficient according to equation 2.11 [87]:

$$\epsilon_{cont} = \epsilon_{fb}^{ei} + \epsilon_{ff}^{ei} + \epsilon_{ff}^{en} \quad (2.11)$$

with the emission due to recombination of an ion with an electron:

$$\epsilon_{fb}^{ei} = C_1 \frac{n_e n_i}{\lambda^2 \sqrt{T_e}} \left[1 - \exp\left(-\frac{hc}{\lambda k_B T_e}\right) \right] \xi_{fb}^{ei}(\lambda, T_e), \quad (2.12)$$

and the emission due to collisions between electron and ions:

$$\epsilon_{ff}^{ei} = C_1 \frac{n_e n_i}{\lambda^2 \sqrt{T_e}} \exp\left(-\frac{hc}{\lambda k_B T_e}\right) \xi_{ff}^{ei}(\lambda, T_e), \quad (2.13)$$

and the emission due to collisions between electrons and neutrals:

$$\epsilon_{ff}^{en} = C_2 \frac{n_e n_a}{\lambda^2} T_e^{3/2} Q(T_e) \left[\left(1 + \frac{hc}{\lambda k_B T_e} \right)^2 + 1 \right] \exp\left(-\frac{hc}{\lambda k_B T_e}\right). \quad (2.14)$$

The constants are $C_1 = 1.632 \cdot 10^{-43} \text{Jm}^4 \text{K}^{0.5} / (\text{s} \cdot \text{sr})$ and $C_2 = 1.026 \cdot 10^{-34} \text{J m}^2 \text{K}^{3/2} / (\text{s} \cdot \text{sr})$ [87]. The densities of electrons, ions, and neutrals are n_e , n_i , and n_a , and λ is the wavelength, T_e the electron temperature, h Planck's constant, c the speed of light, k_B the Boltzmann constant, and $\xi_{fb,ff}^{ei}$ are the Biberman factors for free-bound and free-free transitions. The Biberman factors are a correction term for non-hydrogenic behaviour [88]. For discharges in water, these factors can be set to unity for simplicity because

hydrogen is a prominent collision partner. The cross section for electron neutral collisions $Q(T_e)$, can be set to a typical value of 10^{-20} m² [86].

(v) Continuum emission from black-body radiation

At last, the continuum radiation can be described by black-body radiation, originating from the plasma or the hot metal electrode during the pulse-on time. A black body emitter can be assumed as an estimation, although a grey emitter would be more accurate. Black-body radiation can be estimated by Planck's law according to:

$$\epsilon_{bb}(\lambda, T) = \frac{2hc^2}{\lambda^5} \frac{1}{\exp(\frac{hc}{\lambda k_B T}) - 1}. \quad (2.15)$$

“We are trying to prove ourselves wrong as quickly as possible, because only in that way can we find progress.”

Richard Philips Feynman

3 | Experiment, diagnostics and methods

In this chapter, a nanosecond pulsed plasma source for in-liquid discharges are described. The nanosecond pulser is described in the first section of this chapter. The following sections comprise different diagnostics. Each diagnostic and the underlying physics will be described as well as the correlation to the research questions from chapter 1.

3.1 Experimental setup

The setup involving the plasma chamber as well as the nanosecond pulser is described in this chapter. Furthermore, electromagnetic interference generated by the nanosecond pulsed plasma source is discussed.

3.1.1 Plasma chamber

The plasma chamber used for the nanosecond pulsed plasma sources is made out of poly(methyl methacrylate) (PMMA). The overall liquid volume inside the chamber is approximately 25 ml. A sketch of the chamber is shown in figure 3.1.1. The electrodes are mounted from top and bottom into the chamber. The chamber has a width of 2 cm and the electrodes are placed in a central position so that the electrode tip has an approximate distance of 1 cm to the front and back walls (figure 3.1.1(b)). The setup is built with two water inlets and two outlets which can be opened and closed by manual valves which allow a steady-state mode (no change of liquid) and a flow-mode (continuous replacement of liquid). For the latter one, a peristaltic pump is connected to the bottom and the top valve, allowing a continuous flow of liquid. The steady-state mode is used by filling the chamber via the top valve and the air in the chamber gets expelled by the liquid via the top side valve. The liquid outlet for later ex-situ analysis of the chemically modified liquid is at the bottom side valve. Furthermore, three fused silica UV broadband windows are mounted onto the chamber for camera and spectroscopic measurements, two at the sides for line-of-sight measurements and one at the front, respectively. The back is covered with a substrate holder made out of PMMA for surface treatments. The substrate holder is designed with a

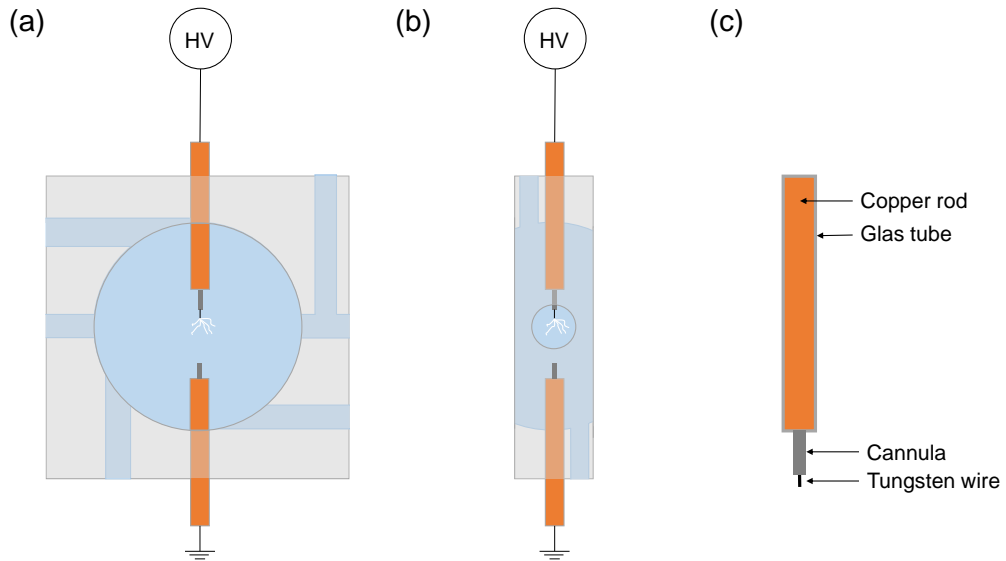


Figure 3.1.1: (a) Front view and (b) side view of the plasma chamber and (c) powered electrode configuration, respectively. The grounded electrode is built likewise without the tungsten wire.

stamp mechanism so that the treated surface can be pressed by the top part of the holder to the bottom holder part. A sketch is presented in figure 3.1.2.

The substrate holder is then mounted directly to the chamber. The electrodes (figure 3.1.1(c)) consist of glas tubes with inserted copper rods. Both electrodes are connected to the high voltage (HV) cables. The electrode tip immersed into the liquid is made out of a stainless steel cannula with a diameter of 0.8 mm with a clamped in tungsten wire (99.95%, Goodfellow GmbH). This wire has a 50 μm diameter and is used to enhance the electric field strength at the tip. The grounded electrode is connected to a second stainless steel cannula but without a wire.

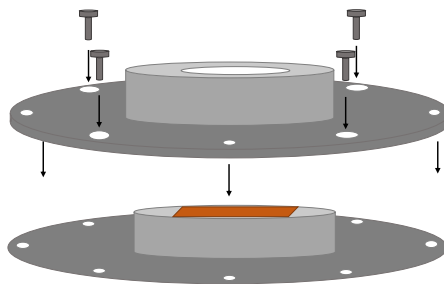


Figure 3.1.2: Substrate holder for in-liquid surface treatment.

3.1.2 Nanosecond pulsed plasma source

The nanosecond pulsed plasma source is the commercial FPG 30-01NK10 high voltage pulse generator from FID Technology GmbH. This pulser is capable of producing pulses with 10 ns length (pulse duration at 80%) and rise times of 2-3 ns. The amplitude can be varied from 10-30 kV, whereas the frequency variation ranges from 1-100 Hz. The pulser is used only with internal triggering, although an external triggering is possible. A sketch of

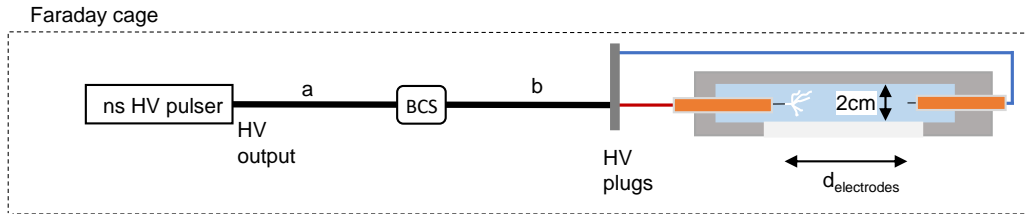


Figure 3.1.3: Nanosecond plasma setup inside Faraday cage. The nanosecond HV pulser is connected via a coaxial cable (length $L = a + b$) with a back current shunt (BCS) mounted at a central position ($a = b$). The electrodes inside the chamber have a distance of $d_{electrodes}$. The HV plug is connecting the powered electrode (red line) and the grounded electrode (blue line) with the inner and outer conductor of the coaxial cable, respectively. The cable lengths and other sizes are not true to scale.

the implementation of the pulser into the setup is shown in figure 3.1.3. The nanosecond pulser is connected to the powered electrode via a RG217 coaxial cable (black line). The cable length L ($L = a + b$) is an important parameter, because a part of the power gets reflected inside the cable and travels back to the pulser due to mismatching of the plasma load. Therefore, different cable lengths were used to distinguish between the incoming and reflected pulses. The used cables are 3.4 m, 6 m, 8.6 m, 10 m, and 12 m long. According to that, a self-constructed high voltage cable connector between the coaxial cable and the electrodes is designed to allow a faster changing of the different cable lengths. Five connectors for each cable are built, splitting the inner and outer conductor of the RG217 cables and mounting them to high voltage connectors. The electrodes can then be plugged into the powered (inner conductor) and grounded (outer conductor) part of the connector. The powered and the grounded electrode connection is illustrated by the red and the blue line in figure 3.1.3, respectively.

The propagating pulse through the HV cable does not dissipate completely into the discharge/liquid due to mismatching impedances. Therefore, a part of the pulse gets reflected at the electrode and travels back to the pulser where it is reflected again. This leads to many reflections and the attenuated pulse

travels inside the cable back and forth. The Fresnel coefficient at the electrode can be determined from the dielectric constant of water $\epsilon_{water}=80$ (still valid in GHz frequency range [89]) and the dielectric constant of the shielding material of the HV cable which is polyethylene (LD-PE) with $\epsilon_{LDPE}=2.4$:

$$r_{electrode} = \frac{\sqrt{\epsilon_{water}} - \sqrt{\epsilon_{LDPE}}}{\sqrt{\epsilon_{water}} + \sqrt{\epsilon_{LDPE}}} = 0.7. \quad (3.1)$$

This gives a reflectivity of $R_{electrode} = r_{electrode}^2 = 0.5$ which indicates that part of the pulse is getting reflected at the electrode. This is just a rough estimation because the electrode components (copper rod, stainless steel canula and tungsten wire) itself influence the reflectivity, which is not included in this calculation for simplicity. The lengths of the cable influences the temporal distance between the reflected pulses [55, 56, 59].

3.1.3 Electromagnetic interference (EMI)

The nanosecond pulser produces HV pulses with short rising times of only a few nanoseconds. Due to this fast increase in voltage, electromagnetic interference (EMI) is arising. This EMI is shielded to avoid a disturbance of other equipment. Therefore, the nanosecond power supply and the plasma chamber with all connecting cables are mounted inside a Faraday cage (figure 3.1.3). The only cable leaving this cage is from AC power which is covered with three ferrite cores. For voltage measurements with a back current shunt (BCS, described below) the connecting BNC cables were also covered with 1-2 ferrite cores as well as for the triggering signal for camera measurements, which is taken from the power supply.

3.2 Diagnostics and methods

3.2.1 Electrical conductivity

The electrical conductivity is a quantity to describe how strong a medium is conducting an electric current. In general, the conductivity σ is linked to the electrical resistivity:

$$\sigma = \frac{1}{\rho} = \frac{j}{E}, \quad (3.2)$$

with the electrical resistivity ρ , the magnitude of the current density j , and E being the electric field.

The electrical conductivity of the used liquids is measured with a GLF100 conductivity meter by GHM Messtechnik. This apparatus is measuring the current I and the voltage drop U between two contacts with a distance of l and an electrode surface A . This results in the electrical conductivity according to:

$$\sigma = \frac{Il}{UA}. \quad (3.3)$$

For liquids, and especially electrolytes, the mechanism of conducting the electrical current is different to solids. While the conduction in solids is carried by electrons and holes, the liquid conduction is carried by the charged species inside the liquid. The current flowing in the liquid is transported by ions and with a higher ion concentration in the liquid, the electrical conductivity increases. Additionally, the current flowing through the liquid can lead to a more enhanced Joule heating and consecutive formation of cavitation bubbles in which discharge ignition can take place. Therefore, the breakdown field decreases for higher electrical conductivity for the same electrode gap distance [90, 91].

In contrast to that, dielectric liquids such as distilled water (dielectric constant $\epsilon=80$) shield part of the electric field (*screening*). This mechanism enhances for increasing dielectric constant of a liquid. For these cases, the breakdown voltage inside the liquid increases due to the screening effect. Therefore, liquids with high electric conductivity but also high dielectric constant can have a higher breakdown voltage as a liquid with lower electrical conductivity. Usually, liquids such as ethanol or sodium chloride solutions which are also used for plasma in liquid discharges have a high electrical conductivity but also a low dielectric constant compared to distilled water. However, M. Kai [80] found that higher applied voltages are necessary for higher conducting liquids (ethanol $6 \mu\text{S}/\text{cm}$, 0.9% sodium chloride solution $1.4 \text{ mS}/\text{cm}$) for the ignition of a nanosecond pulsed plasma with short rising times of 2-3 ns. Although the higher electrical conductivity enhances the current flow through the liquid, the time scale for efficient Joule heating and cavitation void formation is too short for a plasma to ignite. This can be supported by findings of Marinov et al. [61], where nanosecond pulsed plasmas with 30 ns pulse duration and 5 ns pulse rise time were ignited in distilled water ($\epsilon=80$), ethanol ($\epsilon=27$) and n -pentane ($\epsilon=1.84$). The applied voltage for discharge ignition increased from 3.5 kV in distilled water, to 4-5 kV in ethanol and to 10 kV in n -pentane. The same trend of increasing breakdown voltages with decreasing dielectric constants has been found by K.C. Kao [92]. In conclusion, another ignition process than Joule heating and resulting cavitation formation must take place, which shows a different or even no correlation to the electrical conductivity.

3.2.2 Electrical measurements

The voltage measurements for the nanosecond pulsed plasma are performed with a so-called return or back current shunt (BCS) and its signal is monitored by a HD6104A oscilloscope from Teledyne LeCroy GmbH. The BCS is based on the shunt mechanism but is placed in the return leg (grounded side) of the coaxial cable to avoid a damage of the resistors of the oscilloscope by the high voltage potential. The first use of a BCS for nanosecond pulsed plasmas was performed by Udagawa et al. [93]. This technique deduces the current through the transmission cable from the measured voltage drop at the resistors of the BCS. Furthermore, the power can be determined from the incident and reflected pulses inside the cable. A partial reflection of the pulse appears due to a mismatch of impedance at the plasma load. A minimum length of a few meters is needed so that the two pulse signals can be distinguished and do not overlap.

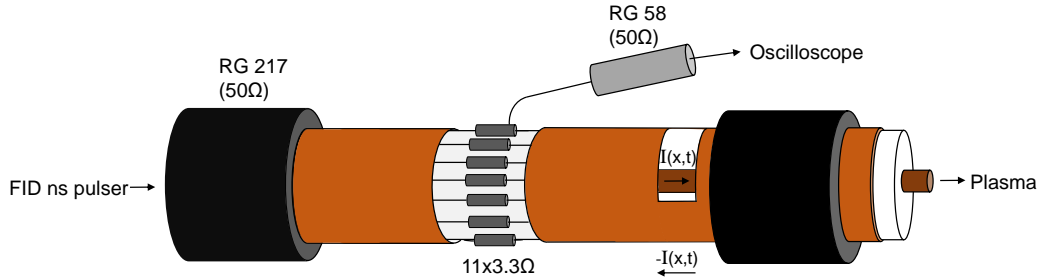


Figure 3.2.1: Schematic of the back current shunt used for the nanosecond pulsed plasma voltage measurements.

The shunt is constructed by soldering 11 x 3.3 Ω (total shunt resistance $R_{shunt} = 0.3 \Omega$) resistors in parallel into the return leg at a central position of a RG 217 coaxial transmission line (bedea Berkenhoff & Drebes GmbH). A schematic of the BCS is given in figure 3.2.1. When the HV pulse passes the back current shunt, a current flowing through the ground shield of the cable is created due to induction, creating a voltage drop at the shunt resistor of [94]:

$$U_{BCS} = R_{shunt} \cdot I. \quad (3.4)$$

This voltage drop is measured by an oscilloscope connected with an attenuator with attenuation factor $\gamma = 31.623$ for a 30 dB attenuator (20 dB + 10 dB attenuators in series). Therefore, the monitored value of the voltage drop by the oscilloscope U_{scope} is:

$$U_{scope} = \frac{U_{BCS}}{\gamma}. \quad (3.5)$$

The line current $I(x, t)$ in the coaxial cable can be determined from the measured voltage U_{scope} as followed:

$$I(x, t) = U_{scope} \cdot (1/R_{shunt}) \cdot \gamma, \quad (3.6)$$

with U_{scope} the measured voltage drop in the shunt, $R_{shunt} = 0.3 \Omega$ the total resistance impedance of the shunt and an attenuation factor γ . Inserting R_{shunt} and γ , equation 3.6 simplifies to:

$$I(x, t) = 105.41 \cdot U_{scope}. \quad (3.7)$$

With this relation the actual voltage pulse can be determined according to Ohm's law:

$$U(x, t) = R_{coax} \cdot I(x, t) = 105.41 \cdot R_{coax} \cdot U_{scope}, \quad (3.8)$$

with the cable resistance $R_{coax} = 50 \Omega$ of the transmission cable.

3.2.3 Phase-resolved ICCD imaging

The discharge during one pulse can be monitored by phase-resolved intensified charge-coupled device (ICCD) imaging. For this technique, an Andor iStar camera is used with the minimum gate of $t_{gate}=2\text{ ns}$. The discharge is focused onto the CCD chip of the camera with a focusing lense. The delay between discharge ignition and camera measurement is canceled out by setting the internal delay t_{delay} to this time delay (e.g. $t_{delay}=485\text{ ns}$ for the 12 m cable). This value can be roughly calculated from the cable length and then be finely adjusted by shifting t_{delay} just before the first emission is visible.

The understanding of the plasma dynamic would require a temporal correlation between voltage pulse (BCS) and light emission (camera) from the discharge. This is, however, difficult on the required temporal scale of ns or less. A synchronisation between the BCS signal and the camera is not possible, because on the one hand the BCS signal is too high and would damage the external trigger of the camera, which is maximum 5 V. On the other hand, the EMI transported from the BCS is influencing the camera too much. The measured voltage drop at the BCS is in the range of tens of volts and therefore too high to be used as a trigger signal. Even if it would be possible to trigger the camera with the BCS (e.g. by using attenuators at the output of the BCS), it is almost impossible to measure all cable length without any error to calculate the delay time. Therefore, the first emission is correlated with the rise of the voltage pulse. The plateau phase of the voltage pulse is leading to a 'dark phase' in emission as discussed in literature [29, 36]. The correlation of the first emission with the rising front of the voltage pulse leads to an overlap of an intensity drop during the plateau phase. Therefore, it is assumed that this cross-correlation is accurate.

Then, the delay is shifted by $t_{shift}=2\text{ ns}$ after each single shot and therefore individual spectra following the whole pulse length can be resolved. However, the imaging of the discharge evolution is not resolved within one pulse. Since the camera is not fast enough to resolve a single pulse, single shots of the discharge are taken during different pulses for different times inside the pulse. Hence, the monitoring of e.g. one streamer is not possible with this setup. Nevertheless, this phase-resolved imaging is giving information about the overall intensity, the position of the plasma at the electrode tip and the behaviour of the discharge during the rising and the falling edge of the voltage pulse.

3.2.4 Shadowgraphs

Shadowgraphs are a method to monitor non-uniformities in liquids. This technique is using the fact that disturbances in a medium refract light rays which lead to shadows. A schematic of the setup is shown in figure 3.2.2.

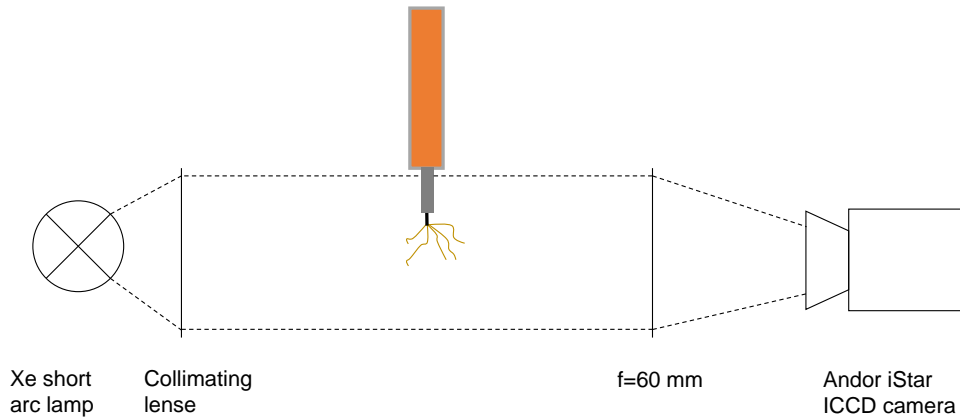


Figure 3.2.2: Schematic of the optical shadowgraph setup. The dashed lines illustrate the light beam.

The light from a xenon short arc lamp is collimated and illuminates the plasma chamber from behind. The light beam reaches the electrode tip through the windows of the chamber. The changes in the refractive index generated by density gradients depletes the light beam which is focused behind the electrode ($f=60\text{ mm}$) and is then collected by an Andor iStar ICCD camera (DH734-18U-03). The camera has a spectral sensitivity in the range of 180–850 nm and is triggered by the sync-output of the HV pulse generator. The jitter of the triggering signal is in the low picosecond range and can be neglected.

The shadowgraphs are taken to monitor the evolution of the plasma and the resulting density fluctuations inside the liquid. In general, Schlieren

measurements could also be performed but exhibit much lower light intensity compared with shadowgraphs for the same light source due to its optical setup.

3.2.5 Optical emission spectroscopy

Optical emission spectroscopy (OES) is performed to monitor the spectral lines of different species which indicate the composition of the plasma in a time-resolved manner. With that, the composition of excited species inside the plasma can be analysed. Furthermore, the spectral line shape due to Stark broadening can be used for determining the electron density as well as the electron temperature.

The light emitted from the nanosecond pulsed plasma is analysed with a triple-grating SpectraPro 750 spectrograph from Acton Research with a 50 grooves/mm grating blazed at 600 nm and a slit width of 25 μm . A sketch of the setup is illustrated in figure 3.2.3.

Two different optical fibre setups were used for different measurements: (i) The time-resolved discharge emission is measured with a 30 ns gate and 15 ns steps with a PI-MAX 1K Princeton Instruments camera (Gen II RB Slow Gate Intensifier) (ICCD 1 in figure 3.2.3) to monitor various pulses due to pulse reflections at the discharge chamber and the pulser. With that, an overall time span of about 300 ns could be resolved. (ii) The emission spectra with an even higher time-resolution from the ignition to the end of the initial pulse is measured with both, gate and step width of 2 ns, with the Andor iStar ICCD camera (DH734-18U-03) (ICCD 2 in figure 3.2.3). Therefore, an overall time span of approx. 30 ns can be resolved. These two different measurements will be distinguished in the following as whole expansion over several hundreds of nanoseconds resolved (i) and initial pulse resolved (ii) measurements.

For both measurements, the light emission is collected by a collimator attached to the first of two UV suitable optical fibre bundles ((d) in figure 3.2.3). This fibre bundle for measurement (i) is a plastic shielded fibre from Thorlabs GmbH with a core diameter of 600 μm . Measurement (ii) is performed with a custom made optical fibre bundle without shielding, also with a core diameter of 600 μm from CeramOptec GmbH. This first plastic-shielded or unshielded fibre is necessary to transport the light emission out of the Faraday cage without EMI. Each of these fibre bundles is then connected via a fibre connector to the second fibre bundle. This is a special manufactured metal-shielded double-y-fibre bundle (53x fibres inside the bundle) by CeramOptec GmbH with a core of 100 μm (denoted as (c) in figure 3.2.3) for both measurements (i) and (ii). This bundle has two y-shaped ends, which allows a reference light source to be displayed next to the discharge emission

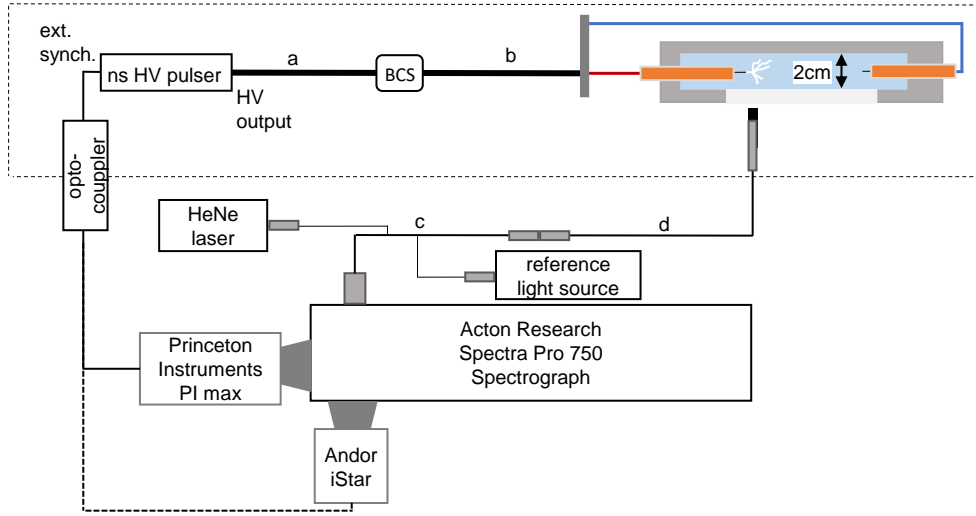


Figure 3.2.3: Schematic of the complete optical emission spectroscopy setup. The dashed line represents the Faraday cage around the plasma chamber and the HV pulser.

on the one side. Additionally, a laser can be coupled into the beam path of the fibre optic to focus the beam path on the $50\ \mu\text{m}$ tungsten wire on the other side (compare figure 3.2.3).

The two bundle ends on the plasma chamber and on the spectrograph side are used for alignment. They contain seven fibres from the fibre bundle. Therefore, the emission from the plasma is captured by the remaining 45 fibres of the fibre bundle. All fibre bundles have a numerical aperture $\text{NA}=0.22$ and the distance between the collimator and the tungsten electrode tip is approx. 4 cm. The collected light from the plasma is therefore covering a field of view of a few millimeters.

The two cameras used for measurement (i) and (ii) have different focal planes which results in different wavelength coverages. The Andor iStar CCD chip has a size of 1024×1024 pixels with a pixel size of $13 \times 13\ \mu\text{m}$ and a focal plane of 13.3 mm. This results for the 50 grooves/mm in a linear dispersion of $26.4\ \text{nm/mm}$ and a resolution of approximately $0.35\ \text{nm/px}$. The PI-MAX 1K has a chip size of 1024×256 pixels with a pixel size of $26 \times 26\ \mu\text{m}$ and therefore a focal plane of 26.6 mm. This results in wavelength coverages of 351.12 nm and 707.52 nm for the Andor and Princeton Instruments camera, respectively.

Because of the smaller wavelength coverage of the Andor camera, the spectra for highly time-resolved measurements are recorded at three different central wavelengths (CW) (400 nm, 550 nm and 850 nm) and are merged together

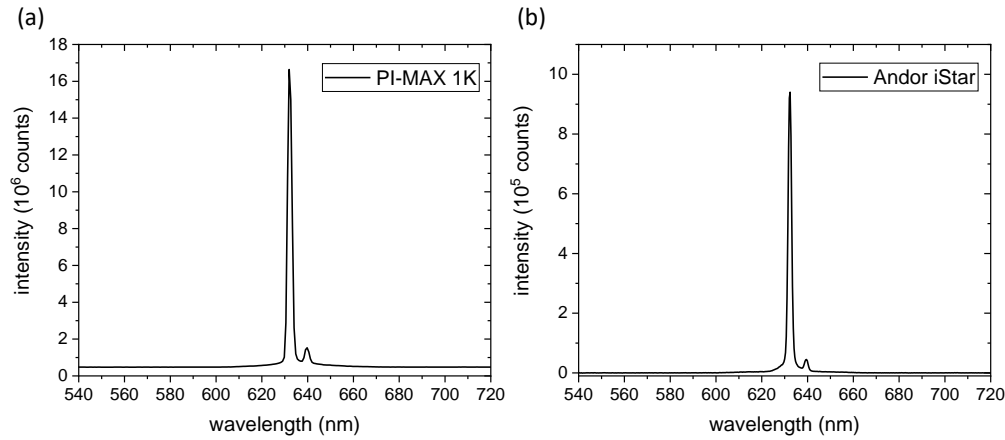


Figure 3.2.4: Instrumental profiles for the setup with (a) the PI-MAX 1K camera ($\text{FWHM}_{PI}=2.3$ nm) and (b) the Andor iStar camera ($\text{FWHM}_{Andor}=1.8$ nm).

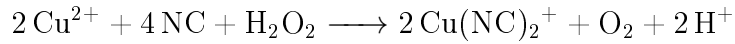
via a Matlab skript which combines the three spectra after background subtraction resulting in a complete spectrum for each step in time. A high pass filter is mounted between collimator and plasma source to suppress the second order for the central wavelengths of 550 nm and 850 nm. The filter cuts off all wavelengths below 500 nm and, therefore, the spectrum with $\text{CW}=550$ nm is measured both with and without filter.

Furthermore, all measurements are calibrated with a D_2 -Halogen lamp. The instrumental profiles for both cameras are measured with a helium neon laser (HeNe, 633 nm), shown in figure 3.2.4. The instrumental profiles have FWHM of 2.3 nm and 1.8 nm for the PI-MAX 1K and the Andor iStar camera, respectively. This is equivalent to the effective resolution of each system.

3.2.6 Optical absorption spectroscopy for liquid chemistry analysis

Optical absorption spectroscopy (OAS) is a diagnostic to determine the wavelength-dependent absorption spectrum of gases, liquids and solids. This is performed by measuring the irradiation passing through the observed medium, interacting with it. For discharges in liquids, this diagnostic is often applied after discharge treatment of the liquid to analyse the chemical composition. Therefore, the liquid is extracted after the treatment from the discharge chamber and is then analysed. Hence, this method is most suitable for longer lived species, such as H_2O_2 . In general, H_2O_2 is difficult to detect directly, because of its broad UV absorption spectrum [95, 96]. Therefore, the H_2O_2 absorption signal is enhanced by using the calorimetric method.

The calorimetric method is applied by using a commercial test kit by Merck KGaG (Spectroquant® Hydrogen Peroxide Test 1.18789.0001) which is based on the reaction of H_2O_2 with Neocuproine-Copper(II). This method exhibits a detection range of 0.88-176.39 $\mu\text{mol/l}$ matching the H_2O_2 concentrations of in-liquid pulsed discharges. It is based on the reduction of Cu(II) to Cu(I) in the presence of Neocuproine (NC). This reaction is shown in the following and leads to an absorption peak at 454 nm:



After plasma treatment, a liquid sample is extracted from the discharge chamber and is inserted into a cuvette in the OAS setup, shown in figure 3.2.5. The light source used for optical absorption spectroscopy is an EQ-

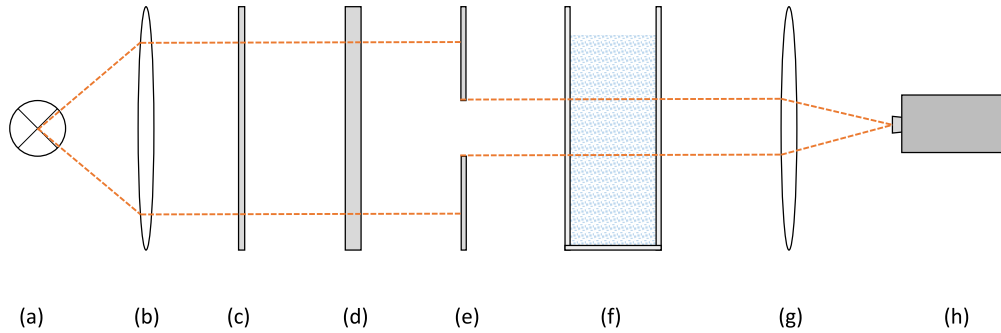


Figure 3.2.5: Setup for optical absorption spectroscopy consisting of a (a) laser driven light source, (b) collimator with $f=60$ mm, (c) grey filter, (d) bandpass filter, (e) shutter, (f) cuvette for liquid sample, (g) focusing lense, and (h) spectrometer.

99XFC LDLS from Energetiq Technology. This light source has a spectral range from 190-2100 nm. A grey filter is placed into the beam to attenuate the intensity of the light source which is afterwards reaching a bandpass filter only allowing light from 350-650 nm to pass. After passing a shutter, the light beam travels through the cuvette which is filled with the treated liquid sample. Then, the beam is focused onto a SILVER-Nova 25 TEC BW16 spectrometer by StellarNet. A calibration has to be performed before each measurement using untreated liquid. With this and the measurement of the absorption peak at 454 nm after plasma treatment, the concentration of H_2O_2 inside the sample can be calculated from the absorbance A according to the Beer-Lambert law (equation 3.9):

$$A = -\log_{10} \left(\frac{I - I_0}{I_{ref} - I_0} \right) = \epsilon cd, \quad (3.9)$$

where I is the intensity of the beam passing the treated sample at 454 nm, I_{ref} is the intensity of the beam passing the untreated sample, I_0 is the

background intensity, ϵ is the molar extinction coefficient with $\epsilon=1.68 \cdot 10^{-2}$ $l/(\mu\text{mol}\cdot\text{cm})$, c is the H_2O_2 concentration and d is the path length through the sample which is 10 mm in case of this cuvette. The molar extinction coefficient ϵ is determined from a calibration curve, which is measured with a commercial standard 30% H_2O_2 solution.

3.2.7 Determination of electron density n_e

The spectrum of discharges in distilled water usually reveals distinctly the H_α line at 656 nm and an atomic oxygen line at 777 nm (OI). The full width at half maximum is broadened for both lines. An exemplary spectrum showing these two lines is presented in figure 3.2.6(a). Figure 3.2.6(b) presents the two lines together with a fit of both lines according to the following analysis.¹

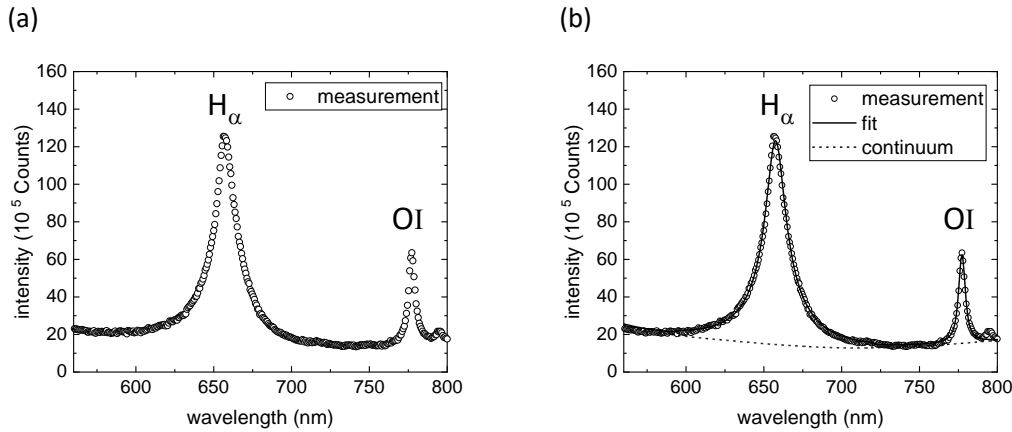


Figure 3.2.6: (a) Exemplary spectrum at 90 ns after ignition of a 10 ns pulsed discharge in distilled water at 20 kV. This spectrum is measured with a PI-MAX 1K camera with a gate of 30 ns and is accumulated over 10000 discharges. The H_α emission line at 656 nm and an atomic oxygen line OI at 777 nm are visible. (b) Exemplary spectrum at 90 ns after ignition (open circles), fit of the data with the described procedure (solid line) and a simultaneously fit continuous background (dashed line). The best fit parameters are $n_e = 8 \cdot 10^{24} \text{ m}^{-3}$ and $T_e=0.5 \text{ eV}$.

It can be seen from figure 3.2.6 that both emission lines are isolated and do not overlap each other. Therefore, the impact approximation for isolated lines can be applied for the atomic oxygen line according to Griem [81]. This approximation describes the line shape function $L(\omega)$ of isolated lines by a

¹The fitting procedure of the spectra with the resulting electron densities has been developed by Julian Held.

Lorentz profile:

$$L(\omega) = \frac{1}{\pi} \cdot \frac{w}{w^2 + (\Delta\omega - d)^2}, \quad (3.10)$$

with w the half width at half maximum (HWHM), $\Delta\omega$ the frequency detuning and d the shift of the line. With the FWHM $\gamma = 2w$, $\Delta\omega = (2\pi c/\lambda_0^2)\Delta\lambda$, $w_\lambda = (\lambda_0^2/2\pi c)w$, and $d_\lambda = -(\lambda_0^2/2\pi c)d_\omega$ the equation transforms to:

$$L(\lambda) = \frac{\lambda_0^2 c}{\pi^2} \cdot \frac{\gamma}{\gamma^2 + 4 \cdot (\Delta\lambda + d_\lambda)^2}. \quad (3.11)$$

With this, the OI emission line in figure 3.2.6 can be fitted according to:

$$y = y_0 + \frac{2A}{\pi} \cdot \frac{\gamma}{\gamma^2 + 4(\lambda - \lambda_c)^2}, \quad (3.12)$$

similar to equation 3.11 with the area A under the emission line, γ the full width at half maximum (FWHM), λ_c the central wavelength of the line and the wavelength λ .

The fitting of the H_α line is based on the comparison between the experimentally measured profiles and computer simulated profiles of Gigosos et al. [97] depending on the electron densities:

- (i) $n_e = 10^{20} - 10^{25} \text{ m}^{-3}$: The complete line profiles given by [97] for discrete electron densities are used and compared with the measured spectrum. For electron densities values in between the discrete values an interpolation is applied.
- (ii) $n_e < 10^{20} \text{ m}^{-3}$ and $n_e > 10^{25} \text{ m}^{-3}$: For these ranges, an approximation formula provided by [97] is used. Nevertheless, these values have to be taken with caution as the underlying theory has not been experimentally validated above 10^{25} m^{-3} .

The electron density for the best fit with the H_α line is then compared with the Lorentz fit of the OI line. The line profile ϵ is described by the convolution (*) of the instrumental profile P , the Stark profile S and the van der Waals profile W (if necessary) and is dependent on the gas density n_g , the gas temperature T_g , the electron density n_e and the electron temperature T_e :

$$\epsilon(n_g, T_g, n_e, T_e) = P * S(n_e, T_e) * W(n_g, T_g). \quad (3.13)$$

The complete fit function $I(A_{H_\alpha}, A_{OI}, n_g, T_g, n_e, T_e)$ is the sum of both line profiles ϵ_{H_α} and ϵ_{OI} which are weighted with their intensities A_{H_α} and A_{OI} , respectively, according to:

$$I(A_{H_\alpha}, A_{OI}, n_g, T_g, n_e, T_e) = A_{H_\alpha} \cdot \epsilon_{H_\alpha}(\lambda_{0,H_\alpha}, n_g, T_g, n_e) + A_{OI} \cdot \epsilon_{OI}(\lambda_{0,OI}, n_g, T_g, n_e, T_e), \quad (3.14)$$

with the unshifted wavelength positions $\lambda_{0,H\alpha}$ and $\lambda_{0,OI}$ for the H_α and atomic oxygen line, respectively. The parameters n_g and T_g are set to fixed constants motivated by the results from the cavitation theory model (section 4.4) in the case of a possible van der Waals contribution. The line intensity, wavelength positions, and electron densities and temperatures are fitted.

If the agreement between data and fit is decent, an overall model spectrum is given as shown in figure 3.2.6(b). This fit shows excellent agreement with the measured data. Additionally, a continuum background has to be included in the procedure and subtracted for the spectral line fit correlating to the previously discussed continuum radiation. This is done in a self-consistent fit algorithm (Levenberg-Marquardt) with the following fitting procedure:

1. Reading the background subtracted data.
2. Finding the best match of simulated H_α line from [97] with data and simultaneously fit atomic oxygen line with Lorentz profile including the electron density given from the respective simulated profile.
3. Subtracting the best guess of line profiles from data.
4. Smoothing the resulting continuum background spectrum with rolling average (over 100 pixel, about 700 nm).
5. Returning sum of smoothed continuum background spectrum and line emission.

According to this fitting procedure, the data is treated as a combination of line emission and continuum background. Each spectrum is analysed individually to avoid systematic errors.

“The important thing is not to stop questioning; curiosity has its own reason for existing.”

Albert Einstein

4 | Physics of nanosecond pulsed plasmas in distilled water

The following chapter deals with the physics of the nanosecond pulsed plasma inside distilled water. The electrical discharge properties will be discussed in section 4.1. Afterwards in section 4.2, the discharge ignition is analysed, focusing on possible initiation mechanisms which deal with the first research question

"Which physical processes cause ignition of a high voltage, nanosecond pulsed discharge in a liquid environment?"

Section 4.3 discusses the physics of the discharge during the initial voltage pulse, including the analysis of emission spectra and propagation mechanisms inside the liquid. Furthermore, re-ignitions of the discharge due to electrical oscillations inside the cable are monitored over a longer time scale of a few hundreds of nanoseconds and finally, the electron density for the initial pulse and the re-ignitions is determined. In this section, the first part of the second research question

"How is the discharge propagating inside the liquid medium and how is this correlating with the chemical species created by the plasma?"

is addressed. The second part concerning the chemistry induced by the plasma is then discussed in the last two sections. After discharge emission, a cavitation bubble is formed, which is outlined in section 4.4. Lastly, the chemistry of these discharge, in particular the H_2O_2 production, is discussed in section 4.5.

4.1 Electrical discharge properties

The electrical properties, specified by the used pulsed power source, are key parameters to change the physical behaviour of the discharge inside the liquid. Therefore, it is necessary to gain as much knowledge as possible about the electrical characteristics of the discharge system.

4.1.1 Pulse shape characteristics

The electrical properties of the discharge are crucial parameters for the behaviour of ignition and propagation inside the liquid. The most important properties are the rising time (i), the amplitude (ii), the polarity (iii), the pulse length (iv), and the shape of the pulse (v). These properties can be monitored by the BCS and influence the discharge as follows:

- (i) *rising time*: The rising time of the pulse is crucial to distinguish different ignition mechanisms inside the liquid. In literature it is shown that pulses with long rising times of a few hundreds of ns to μ s are leading to a microbubble formation previous to the discharge in the electrode tip vicinity [61]. This, however, might not be true for pulses with rising times below several nanoseconds, because the liquid cannot react fast enough to the resulting forces exerted by the applied electric field, as described in chapter 2. Other ignition mechanisms have to be taken into account, as e.g. field effects which are described in section 4.2.
- (ii) *amplitude*: The amplitude of a pulse is a measure for the energy dissipated within the discharge. With higher amplitudes, more energy is dissipated into the liquid which, therefore, results in an increase in emission intensity and possibly also in higher electron densities.
- (iii) *polarity*: The polarity of the pulse could be an important parameter for the ignition process. If the ignition is in fact generated by field effects, the polarity of the pulse would influence the ignition process significantly. For a positive potential between electrode and liquid, field ionisation is assumed whereas a negative potential would lead to field emission. During field ionisation, electrons are tunneling from the liquid into the electrode tip and ionisation occurs in the tip vicinity. Field emission, however, leads to a tunneling of electrons into the liquid. If the polarity at the tip electrode would be switched from positive to negative, the field effects would be reversed. This should be distinguishable in the emission pattern. Additionally, the electric field threshold for discharge breakdown for both processes is different and should therefore be an indicator, if these processes are dominating the discharge ignition.
- (iv) *pulse length*: The pulse length, usually given as the FWHM of the pulse, determines the lifetime of the discharge. During a longer voltage pulse, more liquid molecules can be dissociated and ionised which increases the number of chemical processes during one pulse. Therefore, if a dissociation of different molecules is desired, a longer pulse length could be favourable.
- (v) *pulse form*: The pulse form is influencing the discharge behaviour. It is discussed in literature that a discharge is only present during a

time-variation of the applied voltage dU/dt . This is true for the rising and falling edge of the pulse. If a *square* pulse is applied, a plateau phase dominates the pulse. During this plateau phase, the so-called ‘dark phase’ appears [29, 36]. If the pulse would be designed into a *triangular* shape, such dark phase should not occur and the discharge would be visible during the whole pulse length.

Figure 4.1.1 shows the voltage calculated from the BCS signal for the 12 m cable at 10 kV with distilled water as medium. This pulse has a positive polarity, a FWHM of 12 ns, and a rising time of 2 ns. Furthermore, a maximum amplitude of 10.8 kV is reached but only for a few ns. Then, the pulse reaches an average of 7 kV before the voltage drops at the end of the pulse. The time from 5-12 ns will be described in the following as the *plateau*, although small changes in the voltage amplitude are still visible. The high peak in the beginning of the pulse is possibly an artefact of the setup. The pulse shape given by the producer has a pulse length of 10 ns (at 80%) and a squared shape. Therefore, the distorted pulse shape seems to be generated by this specific setup.

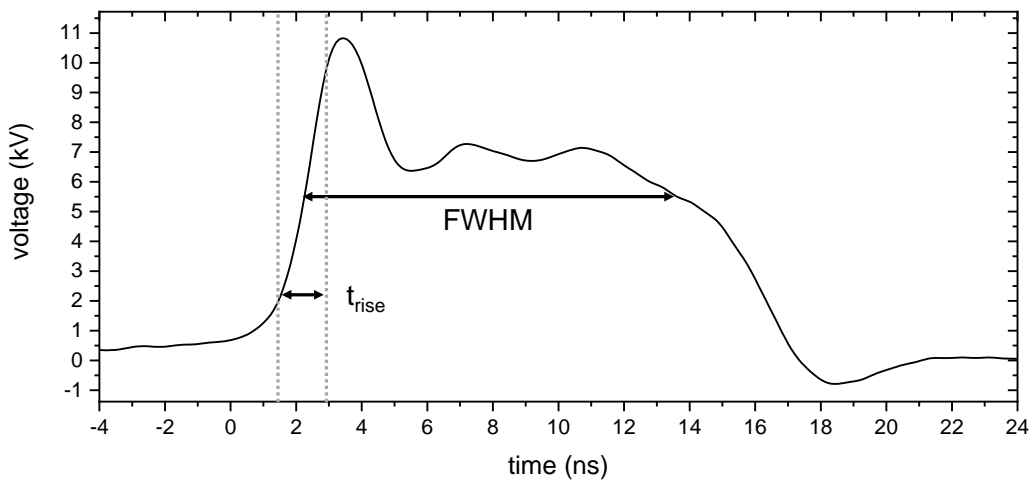


Figure 4.1.1: BCS signals from the 12 m cable at 10 kV for electrodes in distilled water. The vertical dashed lines mark the times at 0.1 U and 0.9 U, respectively. The calculated values from this graph are FWHM=12 ns and $t_{rise}=2$ ns.

Another parameter which can influence the discharge is the surrounding medium of the electrodes. To investigate the influence of the used electrode configuration as well as the surrounding medium (air, water), BCS measurements for the 12m cable at 10 kV (below breakdown voltage) with an *open circuit*, with electrodes *in air*, and with electrodes in *distilled water* are performed and presented in figure 4.1.2. The numbers (1),(3) mark the forward

travelling pulses whereas (2),(4) describe the backward travelling pulses. The graphs in figure 4.1.2 show all the same pulse shape of the initial pulse (1). The comparison of the reflected pulses (2) for an *open circuit* and *in air* shows a change in pulse shape which indicates the impact of the electrode configuration. The *open circuit* is measured without the electrodes being connected to the HV plugs whereas the electrodes are connected to the HV plugs for the *in air* case. It is visible that the pulse shape of (2) is changing from *open circuit* to *in air* both in pulse shape and in amplitude.

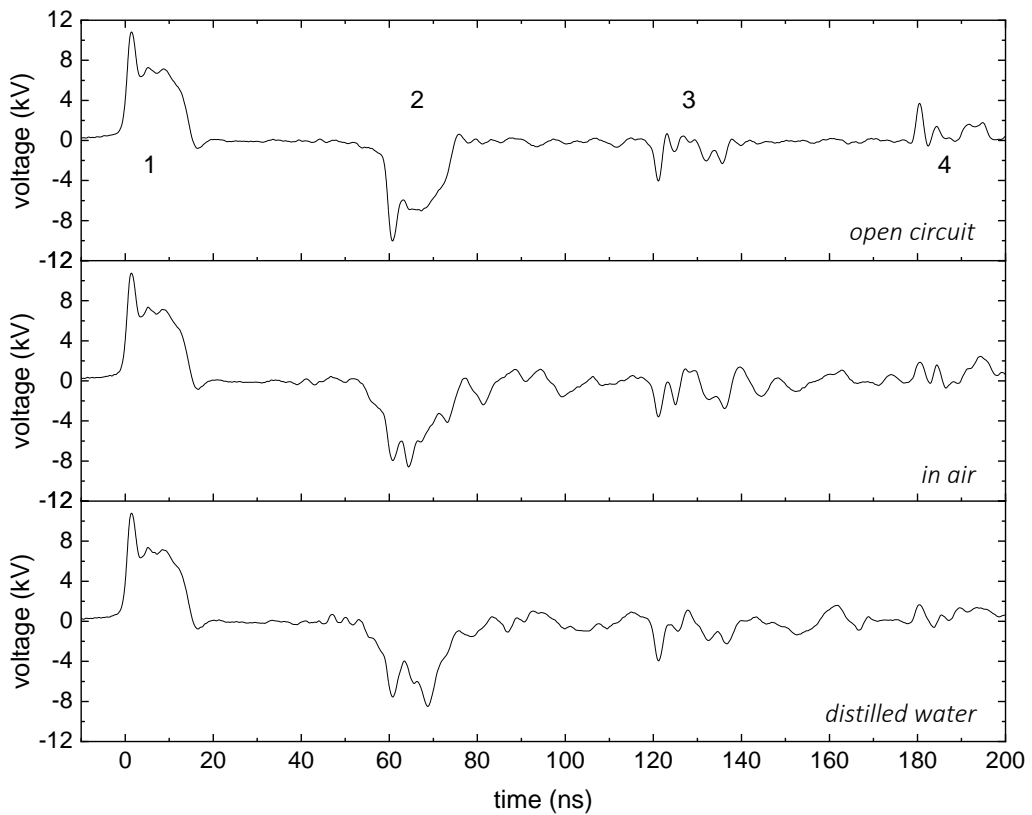


Figure 4.1.2: BCS signals from the 12m cable at 10 kV for an open circuit (no electrodes connected to HV plugs) (top), electrodes in air (middle) and electrodes in distilled water (bottom). The initial pulse (1), the reflected pulse (2) and the following first forward (3) and backward (4) travelling pulses are visible.

Furthermore, the ‘plateau’ described before (in (v) *pulse form*) is not visible anymore in the reflected pulse (2) *in air* and electrical interference is covering the signal. This electrical interference is most likely to be generated due to the experimental setup. Many origins for reflections are given by the complex assembly of the electrodes. Additionally, the HV plugs of both electrodes are further connecting sites which could lead to signal reflections.

The comparison between pulse (2) *in air* and in *distilled water* illustrates the influence of the distilled water as surrounding medium. The pulse shape of (2) is changing again in shape and amplitude of the peaks when changing from *in air* to *distilled water* conditions.

In addition to that, the reflection at the pulser should be discussed. Therefore, pulses (2) and (3) are compared for all measurements. In the case of total reflection ($R=1$) at the pulser both shape and monitored polarity should probably stay the same. The actual polarity of the pulse will change after the reflection at the pulser, but as they travel in different directions, the monitored pulse polarity stays constant. The top graph in figure 4.1.2 reveals that the pulse shape changes tremendously after the reflection at the pulser. The amplitude of (3) is less than half of the reflected pulse (2) and the shape has changed completely. In cases of *in air* and *in distilled water*, the pulses (3) and (4) are mostly covered by noise and can poorly be distinguished. This leads to the conclusion that the pulse is only partly reflected at the pulser ($R \leq 1$). Nevertheless, it can be assumed that each forward travelling pulse (1, 3,...) dissipates part of its energy into the discharge.

The time lag between two forward travelling pulses can be determined by comparing the BCS signals of the initial and the reflected pulse. This is done with an *open circuit* setup because the signals can be clearly distinguished from electrical noise. The BCSs are mounted in the center of each cable (compare figure 3.1.3). Therefore, twice the time lag of the initial and reflected pulse (1,2) corresponds to the time between the initial and the following forward travelling pulse (1,3). It is more applicable to compare the pulses (1,2) due to the change of pulse shape of (3) after the reflection at the pulser. Because of their exact shape, the rising front of both pulse signals can be compared after changing the polarity of the reflected pulse signal from negative to positive. The necessary time shift to overlap both signals equals the time between those pulses $t_{1,2}$. Accordingly, the time between two forward travelling pulses is $t_{1,3} = 2t_{1,2}$.

Figure 4.1.3 shows the shifted reflected voltage pulse (dashed line) by 59 ns, overlapping with the initial pulse (solid line). The 12 m cable with an open circuit is used. The shape of the two pulses is slightly different, which leads to the fact that there are some losses at the HV plugs into open air. The time between the initial and reflected pulse is equal to the measured shift $t_{1,2}=59$ ns. This method is used for all cable lengths and the resulting times between two forward travelling pulses $t_{1,3}$ are listed in table 4.1.

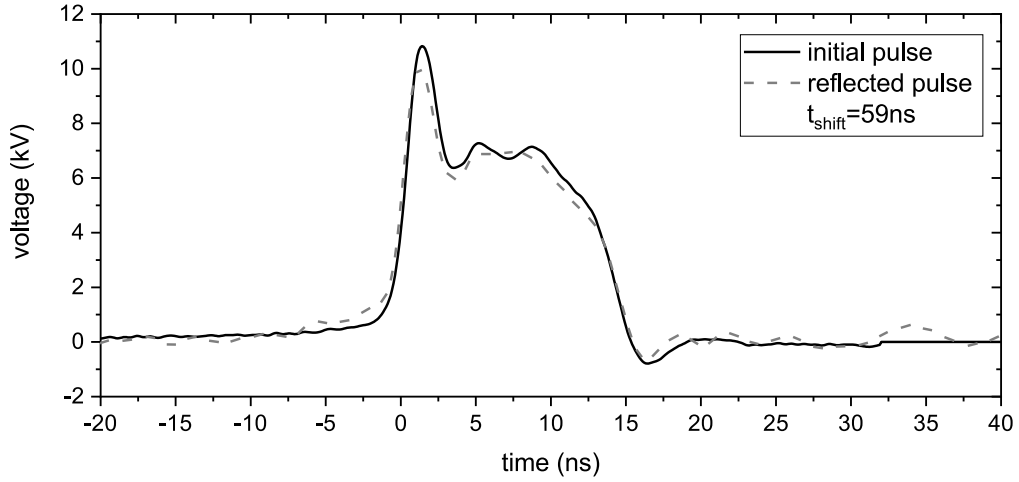


Figure 4.1.3: BCS data of 12 m cable 10 kV pulses with an open circuit configuration. The initial pulse (black solid line) and first reflected pulse (grey dashed line) are overlapped by shifting the first reflected pulse by $t_{shift} = t_{1,3}/2 = 59$ ns.

The measured time delays are compared with calculated values according to equation 4.1:

$$v_{cable} = \frac{c}{\sqrt{\epsilon_r \mu_r}} = 193650 \text{ km/s} = 0.19 \text{ m/ns}, \quad (4.1)$$

where $\epsilon_r = 2.4$ is the relative permittivity of low-density polyethylen (ld-PE, isolation material of the coaxial cable), $\mu_r = 1$ is the relative permeability of water, and c is the speed of light. With that, the delay times t_{calc} between the incident and reflected pulses for the different cable lengths are calculated. The agreement between calculated delay times t_{calc} and measured delay times $t_{1,3}$ between two discharges is acceptable. The residual derivation originates presumably from a slightly inaccurate measurement of cable lengths.

Additionally, the oscillation of the HV power can be compared to a ring-down of the electrical power in the system. The voltage pulse is oscillating inside the cable between the powered electrode and the pulser, losing power during each reflection. Therefore, the total power inside the cable is decreasing with each reflection which can be correlated to a characteristic ‘ring-down’ time constant $\tau_{ring-down}$ describing this power loss. This can be calculated according to

$$\tau_{ring-down} = \frac{L}{v_{pulse}(1 - \sqrt{R_{pulser}R_{electrode}})}, \quad (4.2)$$

with the cable length L , the voltage pulse velocity inside the cable v_{pulse} , reflectance at the pulser $R_{pulser}=1$ and at the electrode $R_{electrode}=0.5$, respectively. It is assumed that the pulser reflects all of the power for simplicity and

the reflectance at the electrode $R_{electrode}$ can be calculated from the Fresnel coefficient $r_{electrode} = \frac{\sqrt{\epsilon_{water}} - \sqrt{\epsilon_{id-PE}}}{\sqrt{\epsilon_{water}} + \sqrt{\epsilon_{id-PE}}} = 0.7$ with $R_{electrode} = r_{electrode}^2 = 0.5$. The ring-down times are calculated for different cable lengths and are listed in table 4.1 together with the measured and calculated distance between two forward travelling pulses, respectively.

Table 4.1: Time delay between two forward travelling pulses $t_{1,3}$ for different cable lengths L measured according to figure 4.1.3, the calculated time t_{calc} according to equation 4.1 and the ring-down time constant of the electrical power inside the system $\tau_{ring-down}$ according to equation 4.2.

cable length L (m)	$t_{1,3}$ (ns)	t_{calc} (ns)	$\tau_{ring-down}$ (ns)
3.4	26	35	60
6	60	62	106
8.6	84	89	153
10	100	103	176
12	118	124	212

The calculated times for the distance between two forward travelling pulses is in agreement with the measured time delays. The measured data is especially inaccurate for the short 3.4 m cable, due to an overlap of forward and backward travelling pulses. The calculated ring-down times are higher than the measured and calculated time delays between two forward travelling pulses. This discrepancy may origin from the values of the reflectances at the electrode and at the pulser, which might be even smaller. Comparing these results with the measured BCS signals in figure 4.1.3, especially the reflectance at the pulser should be smaller. If the reflectance would be one, then the pulses (2) and (3) in figure 4.1.3 would have the same shape and amplitude. A decent fit of the ring-down times with the calculated time delays between the forward travelling pulses can be given by $R_{electrode} = 0.9$ and $R_{pulser} = 0.3$ resulting in ring down times of 36 ns, 64 ns, 92 ns, 107 ns, and 129 ns for the increasing cable lengths, respectively. These ring-down times fit to the calculations of the time delays. Furthermore, the comparison of the reflectances with the measured BCS signal show more realistic values, because the reflectance at the pulser must be less than one according to the BCS signal. The difference in $R_{electrode}$ could result from a slightly different value of the relative permittivities ϵ_r of both the isolation material of the cable and the distilled water.

4.1.2 Reconstructed pulse at the electrode

The BCS is only measuring the voltage drop over the resistances inside the cable, but does not monitor the voltage pulse directly at the electrode. This pulse is different to the BCS voltage. Because at the electrode itself, the voltage reflects and, therefore, the amplitude can increase by a factor of two

at the reflection point in case of an open end. The pulse at the electrode can be reconstructed by shifting the rising fronts so that the signals of the initial and reflected pulse overlap and add up [59, 98]. This leads to a voltage amplitude at the electrode which is approximately twice as high as the applied voltage by the HV pulse generator.

An example for the reconstruction of the electrode voltage is presented in figure 4.1.4. The BCS measures the initial and reflected pulse for a 20 kV

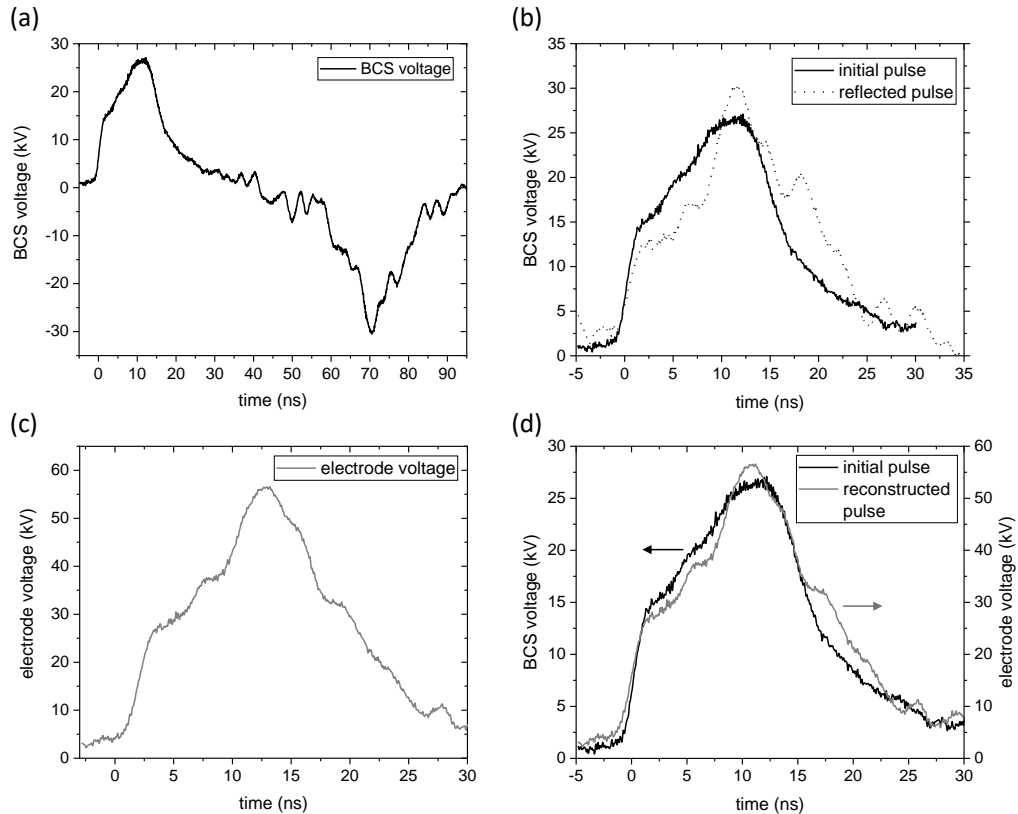


Figure 4.1.4: (a) BCS signal showing initial and reflected pulse. (b) Overlap of initial (black solid line) and inverted reflected (black dotted line) pulse. (c) Reconstructed pulse at electrode (grey line) from adding up signals in (b). (d) Comparison of initial pulse shape (black line) and electrode voltage pulse shape (grey line).

pulse travelling through the 12 m cable as shown in figure 4.1.4(a). The polarity of the reflected pulse is inverted, because of the reverse direction of the travelling pulse inside the cable due to the reflection at the electrode. The real polarity is still positive. Therefore, in figure 4.1.4(b), the signal of the reflected pulse is reversed in polarity and shifted in time so that the rising fronts of the initial and the reflected pulse overlap. These two signals are then added and the electrode voltage is constructed as shown in figure 4.1.4(c). The initial and the reconstructed pulse have a similar shape. Figure

4.1.4(d) shows the direct comparison of the shape and neglectable changes are noticed. Furthermore, the amplitude of the electrode voltage is doubled, as expected.

The appearing differences between the reconstructed pulse and the initial pulse originate from the difference between initial and reflected pulse. The reflected pulse shows small oscillations inside the signal, which are generated from the HV plugs, used to connect the electrodes to the different cables.¹ The initial pulse is measured prior to reaching the HV plugs, whereas the reflected pulse has passed it two times (forward to and return from the electrode). It is also possible that the initial pulse is also slightly deformed by reflections at the HV plugs, which cannot be measured by the BCS at the current position. It can be assumed that the initial and reflected pulse at the electrode exhibit the same shape and, therefore, the reconstruction of the voltage pulse directly at the electrode can be assumed to be twice the value of the applied voltage.

4.1.3 Dissipated power

An estimation of the power dissipated in the plasma can be determined from the BCS signal. Therefore, the power of the incident and reflected pulse is determined from the voltage U and the current I according to equation 4.3:

$$P = U \cdot I. \quad (4.3)$$

By subtracting the reflected power from the incident power, the power dissipated into the plasma assuming no cable losses can be described as: $P_{diss} = P_{initial} - P_{reflected}$. Losses directly at the BCS can be estimated according to:

$$P = I^2 \cdot R_{shunt} \quad (4.4)$$

With $R_{shunt} = 0.3 \Omega$ and an approximated line current of $I = 450 \text{ A}$ from the BCS measurements, the power determined at the BCS is 54.7 kW. For a 20 kV voltage pulse ($P=9 \text{ MW}$), this would result in 0.6 % losses. Therefore, losses at the BCS are negligible.

The energy per pulse can be calculated by integration of the power of the respective pulse. The energy dissipated into the discharge is then determined by the difference between the energy of the initial and the reflected pulse $\Delta E_{diss} = E_{initial} - E_{reflected}$. This is illustrated in figure 4.1.5 for the 12m long cable with an applied voltage of 20 kV. The pulse shape of the initial and reflected power measured at the BCS is different, resulting from the dissipated power into the discharge, losses inside the cable and electrical interference at e.g. the HV plugs. The difference in energy of both pulses

¹Previous measurements without HV plugs show an identical shape of initial and reflected pulse with only small differences in amplitude.

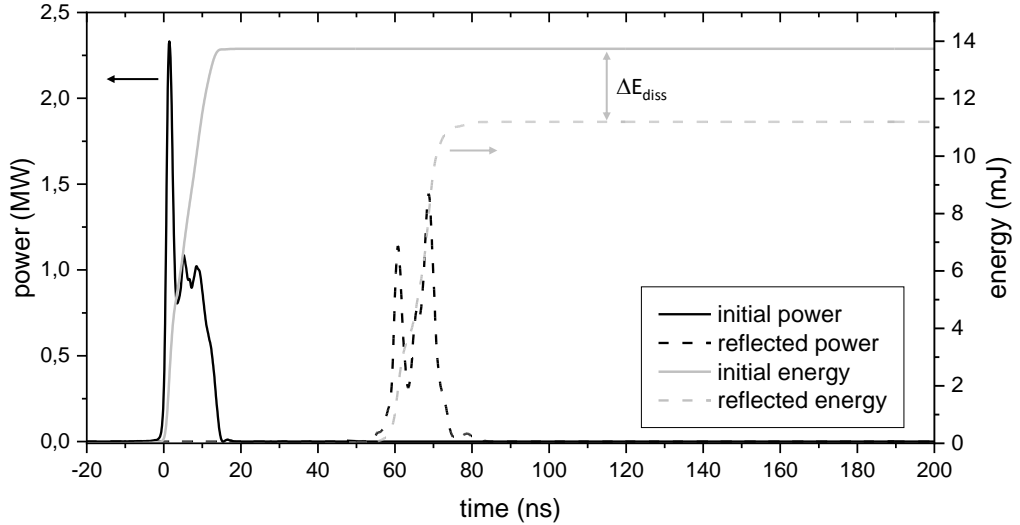


Figure 4.1.5: Initial (solid black line) and reflected (dashed black line) power pulses during a 20 kV discharge in water. The difference of the energy of the initial pulse (solid grey line) and the reflected pulse (dashed grey line) gives an estimate of the dissipated energy $\Delta E_{diss}=2.55$ mJ.

results in a dissipated energy of $\Delta E_{diss}=2.55$ mJ. Babicky et al. [98] determined the energy of a comparable discharge setup in water with an electrode voltage of about 100 kV in a similar manner, resulting in $\Delta E_{diss} \approx 100$ mJ. This value is higher compared to the presented data as they did not use HV plugs resulting in losses and had an overall higher applied voltage. Therefore, this comparison shows that the calculated value is in agreement with literature.

4.2 Ignition of nanosecond discharge in liquid

The ignition of short nanosecond pulsed discharges in liquids is a highly discussed topic in literature as described in section 2.1.1. A common assumption is that nanovoids are formed in the tip vicinity due to electrostrictive forces induced by the strong electric field. Nevertheless, no observation of nanovoids is recorded in literature and a validation is still needed. In the following section, the ignition in liquid environment induced by field effects will be discussed.

4.2.1 Field ionisation

The measurement of the first picoseconds of discharge ignition inside distilled water is not possible with the presented diagnostics, because of the temporal resolution of the camera, which is in the nanosecond range. The position of

discharge emission during the first nanoseconds, however, can be identified by camera imaging. Because the first emission is rather weak, images at 6 ns after ignition are presented in figure 4.2.1. These images illustrate that the discharge is not igniting at the same position for consecutive pulses but at different positions. Additionally, more than one position can lead to a discharge ignition. This leads to the assumption that the surface of the tungsten electrode possess smaller structures than the electrode tip diameter, where the electric field is most enhanced and allows discharge breakdown. These small surface structures were observed by Lukes et al. [99], who compared tungsten and titanium needle tips after operation using scanning electron micrographs (SEM). In comparison to the smooth titanium tip, the tungsten tip revealed many surface protrusions in the range of micrometers.

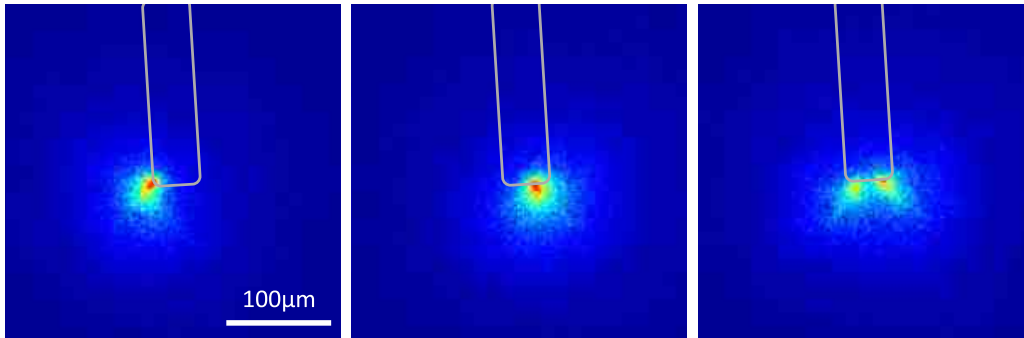


Figure 4.2.1: Single shot camera images at 6 ns after discharge ignition with 20 kV applied voltage and a camera gate of 2 ns. The grey contours illustrate the position of the tip, previously identified by shadowgraphs. The images are presented in false colour due to contrast.

To evaluate the microstructure of the surface after plasma operation, a tungsten tip is compared with a platinum iridium (Pt/Ir) tip applying a voltage of 20 kV at 15 Hz. The tungsten tip has been in use for these parameters for approximately 30 h before the discharge stopped igniting. In comparison to that the Pt/Ir tip only lasted for approximately 1 h in operation before discharge ignition stopped. SEM results for both tips after use are presented in figure 4.2.2. The SEM micrographs show a different structure of the electrode surfaces of both tips. The Pt/Ir tip shows a smooth surface, whereas the W tip reveals small protrusions on the surface in the micrometer range. This is consistent with the findings of Lukes et al. [99]. Although the radius of the W tip is larger compared to the Pt/Ir tip and therefore the electric field should be smaller, the W electrode is igniting discharges continuously compared to the Pt/Ir tip. For the latter electrode tip, a stable discharge ignition can only be assured for approximately 1 h at a pulse frequency of 15 Hz before no plasma is ignited anymore. This leads to the conclusion that

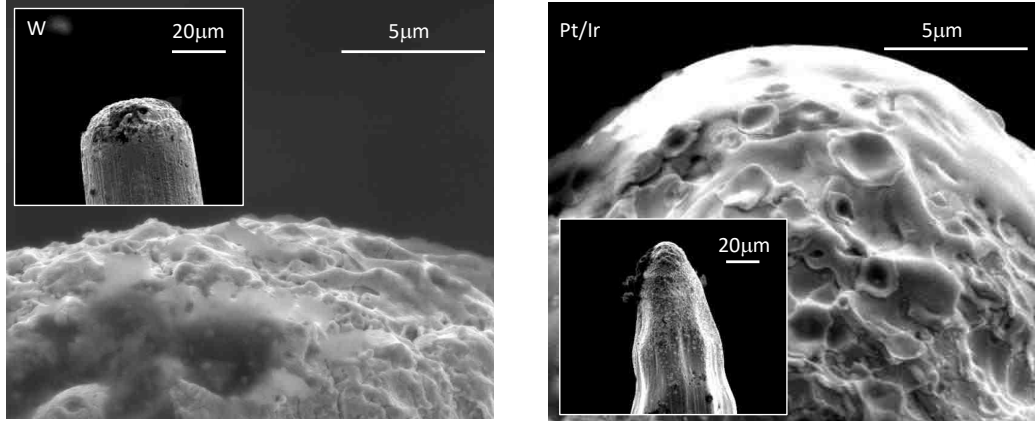


Figure 4.2.2: SEM micrographs of a tungsten tip after 30 h operation (left) and a Pt/Ir tip after 1 h operation (right). Measurements done by P. Grosse at FHI, Berlin.

the microscopic structures (*protrusions*) at the W electrode are the sites of ignition. According to this hypothesis, the area of emission is analysed from camera images. Investigations of the brightest emission at the beginning of the pulse gives an identification of an approximated ignition site with a dimension of max. $8\ \mu\text{m}$. This supports the assumption that the protrusions are sites of a maximal enhanced field strength and therefore the locations of ignition.

The electric field strength needs to exceed a threshold for ignition to appear. Therefore, sharp electrode tips are necessary to enhance the electric field strength. In literature, the electric field strength for pin-to-pin electrode configurations is discussed and calculated in different ways. In the following, these various approximations will be compared.

One approximation of the electric field strength is made according to equation 4.5 from Seepersad et al. [42].

$$E = \frac{2U(t)}{r \ln\left(\frac{4d}{r}\right)}, \quad (4.5)$$

$U(t)$ is the voltage across the electrode gap at the time t (calculated from $U(t) = t \cdot U_{max}/t_{rise}$), U_{max} is the peak voltage of the pulse, t_{rise} is the rising time of the pulse, r is the radius of the tip or protrusion and d is the electrode gap distance. A second rough estimation of the electric field can be made according to R. Gomer [46] as described in equation 4.6:

$$E = \frac{U}{5r}, \quad (4.6)$$

with the applied potential U and the hemispherical tip radius r . An estimation of the electric field is made for different electrode tip radii for both equations. This is illustrated in figure 4.2.3.

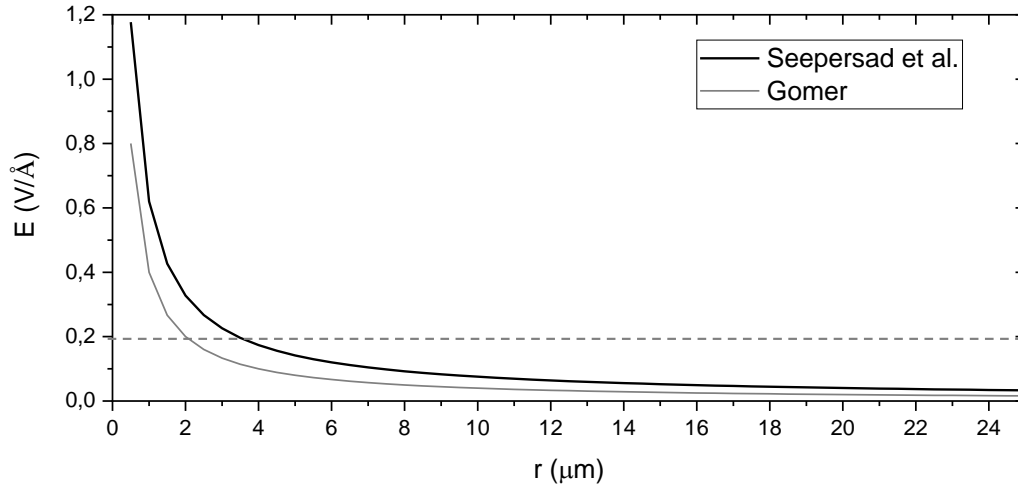


Figure 4.2.3: Comparison of electric field strength for various tip radii calculated according to Seepersad et al. [42] (black) and Gomer [46] (grey). The dashed grey line illustrates the threshold for field ionisation of H_2O [49, 100].

The threshold for field ionisation in liquid water in contact with a tungsten surface is $0.2 \text{ V}/\text{\AA}$ [49, 100], which is reached for electrode tip radii of $2.0 \mu\text{m}$ and $3.5 \mu\text{m}$ according to the equations of Gomer [46] and Seepersad et al. [42], respectively. By comparing these values with the protrusions visible on the SEM micrographs in figure 4.2.2, it can be assumed that the threshold for field ionisation can be reached with the tungsten electrode. The protrusions show tip diameters of less than one μm and are therefore, smaller than the calculated tip radii.

This leads to the conclusion that field ionisation of water generates the first electrons (described in detail in section 2.1.1). The electrons tunnel through the distorted potential towards the tungsten electrode and leave a layer of adjacent ions. These ions attract negative charges from the surrounding liquid, which leads to further ionisation events. This movement of electrons is, therefore, starting and maintaining the streamer-like propagation inside the liquid.

4.2.2 Electrostrictive forces

Nevertheless, there is still the discussion, whether nanovoids are generated previously by electrostrictive forces and if they are contributing to the ignition process or even enhance it. The formation of nanovoids was extensively studied theoretically [25, 26, 28, 101, 102] and even Rayleigh scattering as an experimental diagnostic for observing these nanovoids was proposed [21]. Despite that, no experimental validation for the existence of those nanovoids is done. According to Herbert et al. [103], a threshold pressure exerted on water of -24 MPa is necessary so that nanovoids can be formed. This was validated by calculations of Tereshonok et al. who estimated the total pressure depending on the distance from tip radius and rising time [28]. These calculations were performed for 1 kV and a tip radius of $3 \mu\text{m}$. To estimate the possibility of cavitation ruptures to occur in our system, the following calculations are made. There are two conditions for cavitation ruptures in the liquid to occur.² First, the electric field pressure p_E has to exceed the critical pressure $p_{crit} = -24$ MPa. Second, the time scale of the pressure propagation r_0/c_S has to be larger than the rising time of the voltage front, with c_S being the speed of sound in water. This leads to:

$$p_E = \epsilon_r \epsilon_0 E^2 / 2 > p_{crit} \quad (4.7)$$

$$t_0 < r_0 / c_S \quad (4.8)$$

The estimation is based on $\epsilon_r = \text{const.}$ rather than $\epsilon_r = \epsilon(E)$ for simplicity. Nevertheless, these equations are calculated for various tip radii (or protrusion radii) for an applied voltage $E \propto U/r_0 = 20$ kV, $t_0 = 2$ ns, $c_S = 1500$ m/s, $\epsilon_0 = 8.85 \cdot 10^{-12}$ As/(V·m) and $\epsilon_r = 1.77$, leading to two conditions for the radii: $p_{0,thr}$ and $t_{0,thr}$. This is illustrated in figure 4.2.4. Figure 4.2.4 shows that a critical tip radius for reaching the critical pressure is $r_{0,thr} = 10 \mu\text{m}$. The time scale would require a smaller critical tip radius of $r_{0,thr} = 3 \mu\text{m}$ for the liquid to rupture. Because both conditions have to be fulfilled at the same time, the smaller value is necessary for cavitation to occur in the tip vicinity due to electrostrictive forces. Assuming that protrusions with the size of $1 \mu\text{m}$ are the sites of ignition, these conditions would be fulfilled.

Here, liquid ruptures can occur in the described system but an experimental validation is still needed. In literature, even higher critical pressures for the creation of these nanopores are given [104]. It is an open question whether nanovoids are created. If they are generated previous to in-liquid discharge ignition, nanovoids are an important factor for ignition as they can act as sites of ignition.

In conclusion, it is possible that electrostriction forces create nanovoids and rupture the liquid. From literature it seems that nanovoids consist of a gas-like medium in which electrons can be accelerated according to the picture

²Private communication with D.V. Tereshonok

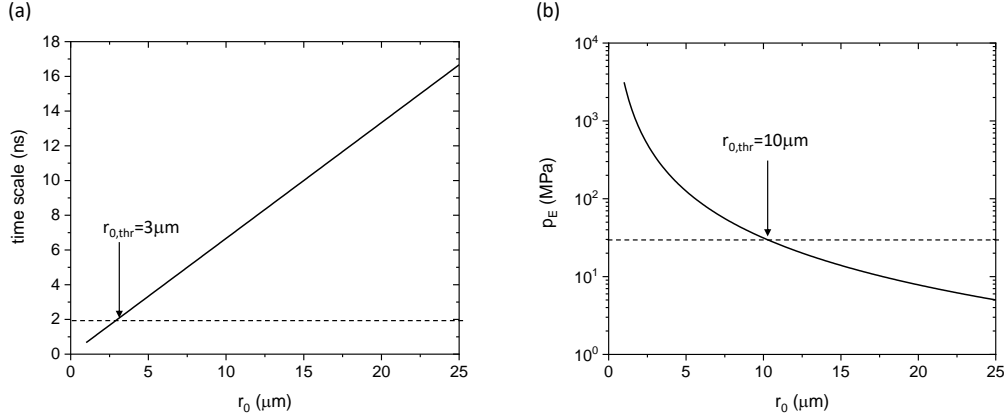


Figure 4.2.4: (a) Time scale and (b) electric pressure p_E according to equation 4.8 and equation 4.7, respectively, for different tip radii. The dashed lines indicate (a) the critical time scale and (b) critical pressure.

presented in [30]. However, nanovoids were not observed or detected. In that context, a region of different refractive index and therefore lower density was formed and detected by Schlieren imaging, but the structure of this region could not be resolved [30]. Even if nanovoids are created, it is still unknown how the first electros are generated inside these pores. Therefore, the ignition of nanosecond pulsed plasmas with strong electric fields and short voltage rising times are possibly ignited due to a combination of both electrostrictive forces and field effects.

4.3 Discharge physics and propagation in liquid

The discharge is monitored by optical diagnostics such as phase-resolved camera imaging and optical emission spectroscopy. In combination with the findings from the previous chapter concerning the ignition mechanism, a model for discharge initiation and propagation inside the liquid is presented. Therefore, the discharge, its re-ignitions and its afterglow are analysed in a time-resolved manner. This section is divided into the investigation of the primary discharge created by the initial HV pulse (section 4.3.1) and the re-ignitions as well as the discharge afterglow (section 4.3.2) following the timeline of the discharge. Additionally, the electron density is determined for all pulses, including the initial and all reflected pulses, for which the H_α line is visible (section 4.3.3).

The primary discharge light emission induced by the initial pulse is monitored with ICCD imaging and is compared with the optical emission spectra

for the respective times. The spectra show a broadband continuum which will be discussed. The different possible origins of this continuum radiation are opposed to each other. Next to this, line emission is observed in the emission spectra which is discussed, focusing on the line shape and the line broadening mechanisms. Additionally, the propagation of the discharge is outlined for the time of the initial pulse and the electron density is determined.

The re-ignitions of the discharge and its afterglow are observed via optical emission spectroscopy. The spectra are compared to the electrical BCS measurements. Furthermore, the electron density is determined from H_{α} line broadening during the re-ignitions of the discharge.

4.3.1 Primary discharge

The primary discharge is generated by the initial HV pulse from the nanosecond pulse generator. After breakdown inside the liquid, the propagating discharge is analysed by camera imaging and optical emission spectroscopy to resolve the emission during the initial pulse. Phase-resolved imaging is performed for a voltage pulse of 20 kV at a frequency of 15 Hz at the tungsten needle tip immersed in distilled water ($\sigma = 1 \mu\text{S}/\text{cm}$). This is illustrated in figure 4.3.1. In (a), exemplary single-shot images during the initial pulse

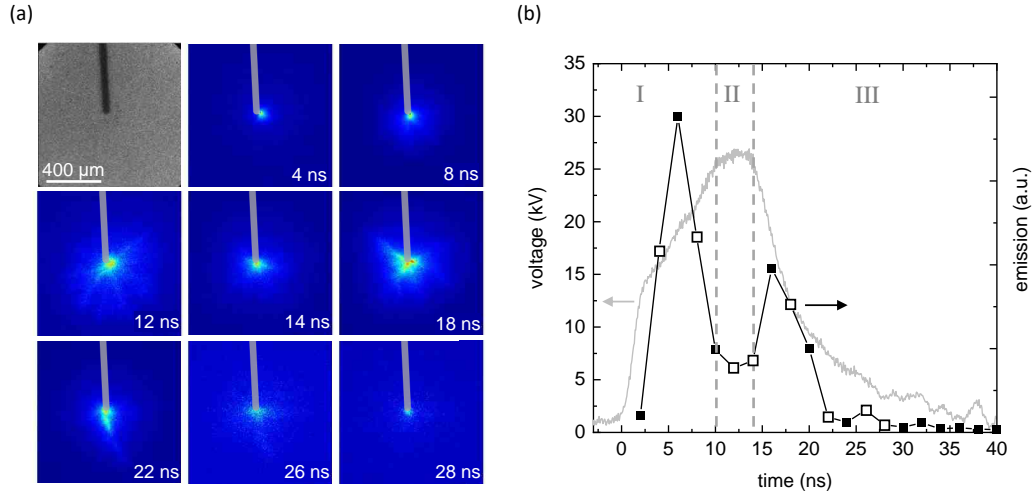


Figure 4.3.1: (a) Phase resolved imaging (scaled to maximum of each image) and (b) voltage pulse measured with BCS (grey line) and integrated light emission from the camera images (black squares). The open squares in (b) correspond to the time stamp of the images shown in (a).

are presented in a phase-resolved manner. The top left image shows a shadowgraph for determining the electrode position for the camera images. The

electrode position is illustrated by the grey area in each image. The integrated light emission is shown in (b) together with the applied voltage pulse. The shape of the voltage pulse form is different from the previously discussed waveform due to a different electrode connection setup. Here, the electrode was directly connected to the HV cable without the HV cable connectors which were incorporated later into the setup. Two intensity peaks can be identified in light emission. By correlating the light emission with the applied voltage pulse, three phases can be determined:

- I *voltage rise (0-10 ns)*: The voltage rises steeply with a rising time of 2 ns and the ignition starts. The ionisation of water molecules is enhanced due to the change in voltage dU/dt . The plasma propagates inside the liquid as a streamer. The leading front of the streamer ionises the water molecules ahead and leaves a region of recombination behind. The electric field needs to increase continuously in order to sustain the discharge propagation.
- II *plateau phase (10-15 ns)*: When the voltage reaches the plateau phase, the change in voltage over time is zero ($dU/dt = 0$). The propagating discharge vanishes and the so-called ‘dark phase’ appears. This is visible in the integrated light emission. During this phase, electrons are moving towards the head of the streamer in order to compensate this positive potential inside the liquid [30]. Therefore, without an increase in electric field, the discharge becomes weak.
- III *voltage drop (15-40 ns)*: When the voltage drops, the resulting electric field is strong enough to re-ignite the positive space charges created during the rising front of the pulse. The created streamer channels enhance the re-ignition. Furthermore, field emission occurs at the electrode. Due to the distorted potential at the electrode, electrons tunnel into the liquid and are accelerated by the positive space charge of the previously created streamer head. When the voltage drops to zero, the discharge vanishes.

To make a more significant analysis of the initial pulse, time-resolved optical emission spectroscopy is performed. For this, a camera gate time of 2 ns and a step width of 2 ns are used in order to resolve the complete pulse. As discussed in section 3.2.5, the spectra are merged from four measurements with different central wavelengths to cover a large wavelength range. This is done by combining the small wavelength ranges covered by the Andor iStar camera. Each measurement is accumulated over 1000 discharges. The resulting emission spectra are presented in figure 4.3.2. During the first 10 ns (rising voltage front, phase *I*), a broad continuum is visible in the emission spectra with an additional specific structure at the wavelength of H_α , H_β , and H_γ . The intensity and, therefore, the continuum radiation decreases during the ‘dark phase’ (10-15 ns, phase *II*). Afterwards (>15 ns, phase *III*), broad

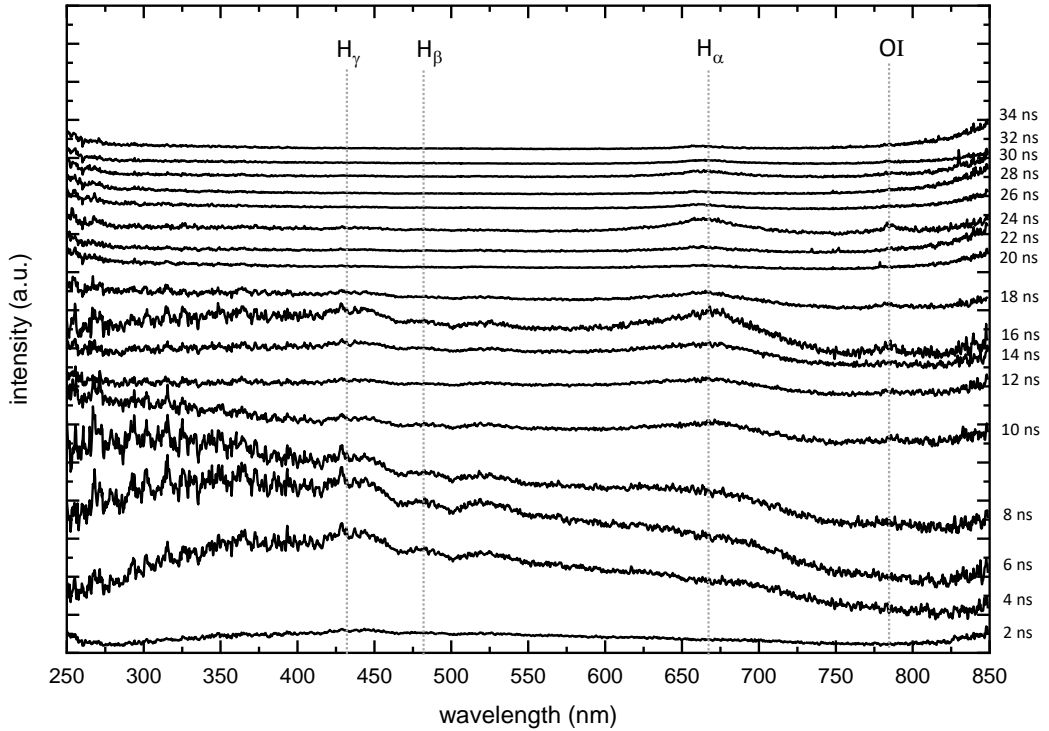


Figure 4.3.2: Time-resolved optical emission spectra. The spectra are scaled for optimal visibility. The grey dotted lines illustrate the central wavelength λ_0 of the H-Balmer lines H_α at 656 nm, H_β at 486 nm, H_γ at 434 nm, and an atomic oxygen line at 777 nm. Each spectrum is recorded with a gate of 2 ns and accumulated over 1000 discharges.

emission lines are visible in the spectrum and the intensity decreases after this second intensity peak.

The different structures (continuum and emission lines) can be attributed to various emitting regions of the discharge. The continuum can be generated by different mechanisms as described in section 2.3.3. In the following, these different mechanisms will be analysed to find the most suitable interpretation for this continuum radiation. The emission lines are most likely generated by the propagating plasma. They will be analysed concerning different regions of emission from the propagating plasma (ionisation region and recombination region).

Continuum radiation

The continuum radiation is most visible during the first 18 ns after first detecting emission. The highest intensity of the emission is present during the rising front of the voltage pulse. For better analysis, the spectra with the

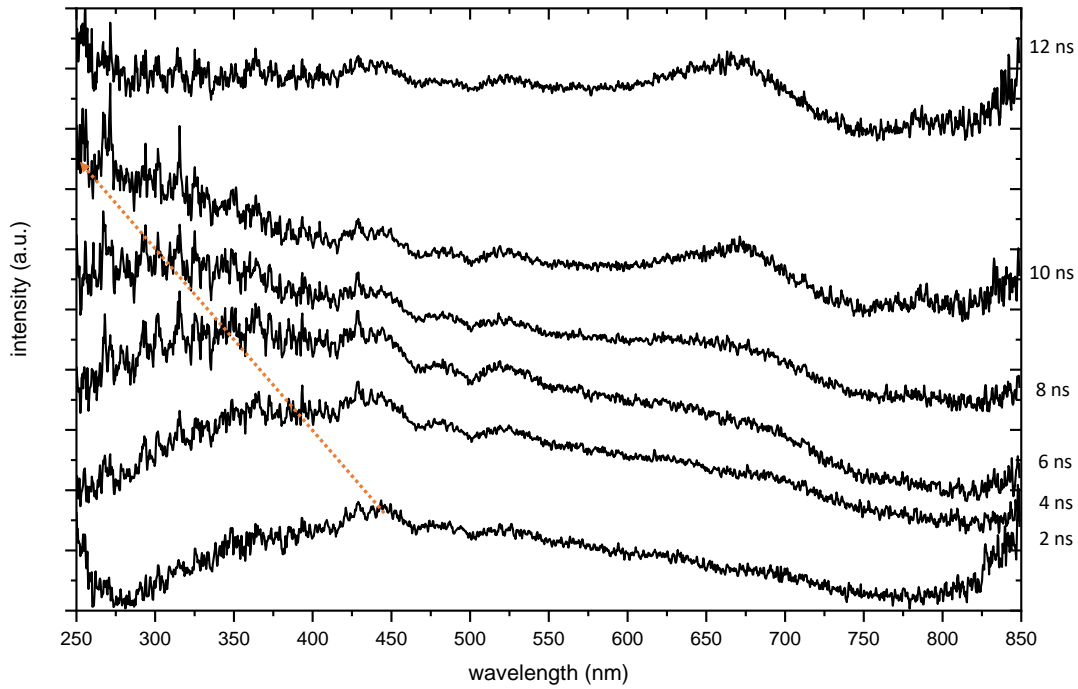


Figure 4.3.3: Optical emission spectra at 2-12 ns measured for a 20 kV discharge at 15 Hz inside distilled water. The spectra are stacked and scaled for best visibility. The dashed orange arrow indicates the shift over time of the continuum peak to lower wavelengths.

most prominent continuum background are plotted in figure 4.3.3. Five fundamental processes can be responsible for continuum radiation, which will be discussed according to their likeliness to contribute to the continuum.

- (i) *Significant broadening of spectral lines due to Stark or van der Waals broadening*

The direct ignition of the plasma inside the liquid leads to the assumption that H and O emission lines as well as molecular lines should be present. The emission lines of H_{α} , H_{β} , H_{γ} and the atomic oxygen line at 777 nm are visible in figure 4.3.2 and figure 4.3.3. These lines are highly broadened due to the Stark effect and some are influenced by self-absorption as discussed in the following section. Nevertheless, the broadening of the lines does not match the continuum, especially not in the UV. As there are no other contributions of line emission which would be visible at later stages of the pulse where the continuum is vanished, this process will be neglected for describing the continuum.

(ii) *Molecular bands*

Additionally, molecular bands as, for example, from OH could contribute to the spectrum. These lines could also be broadened due to different broadening mechanisms. Nevertheless, these bands could not be determined from the presented spectra which could also result from the fairly low signal-to-noise ratio at the left and right end of the spectra. Since this molecular line emission is also not found in similar measurements in literature [38, 56], it will be neglected.

(iii) *Radiative dissociation continuum of molecules*

Another possible process responsible for the continuum is the radiative dissociation continuum of molecules. Especially the dissociation continuum of $H_2(a^3\Sigma_g^+ \rightarrow b^3\Sigma_u^+)$ was discussed in detail for non-equilibrium capillary-arc and H_2 :Ar microwave discharges [84]. Additionally, this continuum was modeled and compared to experiments by Fantz et al. [85] for a low-pressure ECR plasma. Simek et al. [59] studied the emission of a similar pin-to-plane in-liquid discharge which is generated by 7 ns pulses (FWHM) at 50 kV inside deionised water. They observed a shift of the UV emission in time. They concluded that first the continuum is associated with free-bound and free-free radiative transitions. Further, the shift of the continuum can be best described by the bound-free $H_2(a^3\Sigma_g^+ \rightarrow b^3\Sigma_u^+)$ transition. They argued that the UV intensity of this transition increases with discharge time. In their measurements, the overall intensity increases with time as well as the UV intensity. This is in contrast to the presented measurements.

The continuum is visible in the time-resolved emission spectra presented in figure 4.3.3. The overall intensity increases during the rising front of the voltage pulse until it reaches the voltage plateau at 10 ns. Then the intensity drops and the continuum gets weaker. Additionally, a shift of the continuum from the visible to the UV range over time can be seen, as in the work of [59]. But in contrary to [59], the overall intensity does not increase in time but follows the phases I-III of the voltage pulse, as previously discussed. This can lead to the assumption that the mentioned free-bound $H_2(a^3\Sigma_g^+ \rightarrow b^3\Sigma_u^+)$ transition from an upper bound state to a lower dissociative state is not or less responsible for the UV emission in our experiment. This is supported by the fact that this dissociative continuum ranges only from 180-400 nm, but the continuum spectra presented in this work range from 180-700 nm.

(iv) *Free-bound and free-free radiative transitions*

As mentioned before, free-free and free-bound radiative transitions are discussed to be the origin of the continuum [59]. They may describe various reactions inside the liquid that could lead to free-bound transitions as for example $H_2O(\tilde{C}^1B_1 \rightarrow \tilde{A}^1B_1)$ or the previously mentioned

$H_2(a^3\Sigma_g^+ \rightarrow b^3\Sigma_u^+)$ transition. Furthermore, free-free Bremsstrahlung is discussed. These processes might be suitable candidates for the continuum and their contribution will be discussed.

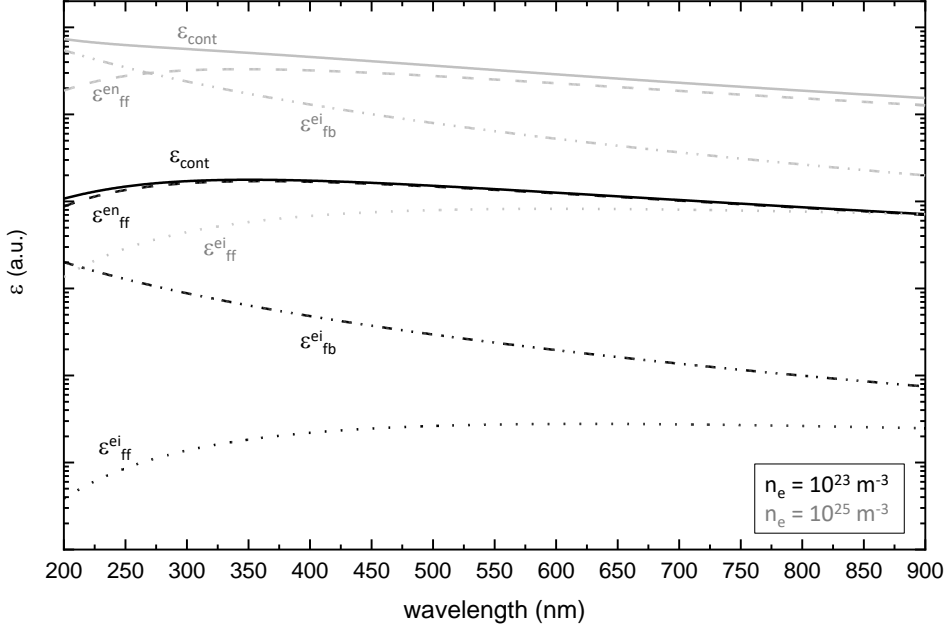


Figure 4.3.4: Calculation of the emission coefficient ϵ_{cont} (solid lines) of the continuum radiation composed of the emission coefficients of free-free radiative transitions of electrons with ions ϵ_{ff}^{ei} (dotted lines) and electrons with neutrals ϵ_{ff}^{en} (dashed lines) and the free-bound transitions of electrons with ions ϵ_{fb}^{ei} (dotted dashed lines). These contributions were calculated for electron densities of 10^{23}m^{-3} (black lines) and 10^{25}m^{-3} (grey lines). Adapted from [105].

According to the equations in section 2.3.3, the contributions of free-bound and free-free transitions to the continuum are calculated for two different electron densities and are presented in figure 4.3.4. It can be seen that for lower electron densities, the emission due to free-free radiative transitions of electrons with neutrals dominates. The free-bound emission of electrons and ions begins to gain significance at higher electron densities, especially in the lower wavelength range. With this, the shift of continuum radiation to the UV as presented in figure 4.3.3 could be explained by an increasing electron density in time. As discussed later, the electron density follows the voltage curve which would support this theory. Therefore, the emission due to the free-bound and free-free radiative transitions will be compared to the following possible source of continuum radiation.

(v) *Black-body radiation*

The continuum could also originate from black body emission either from the plasma itself or the heated tungsten electrode. As the plasma can exhibit high temperatures, the temperature range for tungsten is rather limited. Tungsten has a melting temperature of 3695 K and a boiling temperature of 5828 K. The emission due to black-body radiation can be described by Planck's law:

$$\epsilon_{bb}(\lambda, T) = \frac{2hc^2}{\lambda^5} \frac{1}{\exp(\frac{hc}{\lambda k_B T}) - 1}. \quad (4.9)$$

It is possible that the temperature of the tungsten surface increases tremendously due to the power input and the forces acting on the tungsten tip. Therefore, this process will also be analysed for being a possible source of the continuum radiation.

Here, free-free and free-bound radiative transitions as well as black-body radiation will be taken into account. Therefore, the emission spectra will be compared to the calculate emission spectra of those processes.

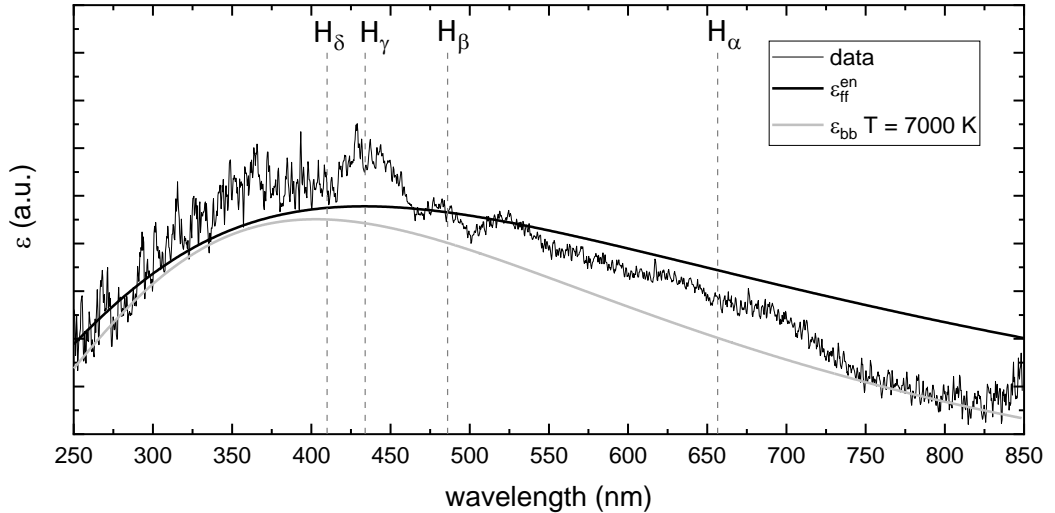


Figure 4.3.5: Emission spectrum at 4 ns after plasma ignition (thin black line) with a camera gate of 2ns, averaged over 1000 discharges. The line positions for H_α, H_β, H_γ, and H_δ are indicated. The solid lines denote either black-body radiation ϵ_{bb} assuming a temperature of 7000 K (grey line, λ^{-5} dependence) or Bremsstrahlung ϵ_{ff}^{en} (thick black line, λ^{-2} dependence) due to electron neutral collisions for an electron temperature of 9500 K. Adapted from [105].

In terms of wavelength dependence, black-body radiation is proportional to λ^{-5} at long wavelengths whereas free-free and free-bound radiative transition

emission scales with λ^{-2} as can be seen in equations 2.12-2.14. The spectra in figure 4.3.3 seem to follow more λ^{-5} than λ^{-2} which can be seen in more detail in figure 4.3.5. This graph shows a better fit of the continuum with black-body radiation rather than with the exemplary λ^{-2} dependent radiation from electron neutral collisions. This is discussed in detail in the following paragraphs.

The boiling temperature of a substance is pressure dependent. For the present high pressures during the discharge, these values may vary. The boiling temperature at various pressures can be calculated by the Clausius-Clapeyron equation:

$$T_B = \left(\frac{1}{T_0} - \frac{R \ln(P/P_0)}{\Delta H_{vap}} \right)^{-1}, \quad (4.10)$$

with the boiling temperature T_0 , the ideal gas constant $R = 8.31 \text{ J}/(\text{K mol})$, the vapour pressure of the material P , the known atmospheric pressure $P_0 = 10^5 \text{ Pa}$ for $T_0 = 5828 \text{ K}$ and the heat of vaporisation of tungsten $\Delta H_{vap} = 774 \text{ kJ/mol}$. The boiling temperature depending on the external pressure is shown in figure 4.3.6.

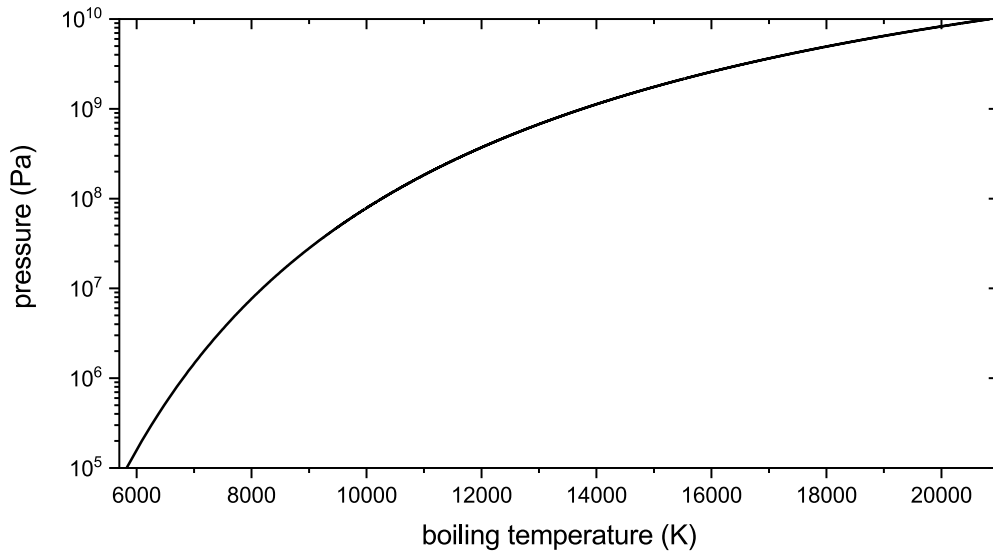


Figure 4.3.6: Boiling temperature T_B depending on the pressure P working on the material according to equation 4.10.

It can be read from this graph that with rising pressure acting on the tungsten, its boiling pressure increases. It will be shown in section 4.4.1 that the liquid at the electrode exhibits pressures in the range of GPa in the very beginning of the discharge [86]. Boiling temperatures of 14000 K or higher

can be reached when the same pressure acts on tungsten. Afterwards, the pressure is released in form of a pressure wave travelling through the liquid. Then, the surrounding pressure is relaxing to normal atmospheric pressure and the boiling temperature reaches T_0 again. This possible increase in boiling temperature in the beginning of the pulse has to be taken into account while fitting black-body radiation to the continuum. The temperatures used for the fitting can exceed T_0 . However, the tungsten tip will not necessarily rise above boiling temperature if the pressure is increased at the same time.

A decrease in tungsten wire length is observed over time. A rate of approximately 1 mm per hour is estimated which leads to the conclusion that part of the tungsten tip is getting above melting/boiling temperature and material gets sputtered over time or melts away. Therefore, even for a short time very high temperatures must be present.

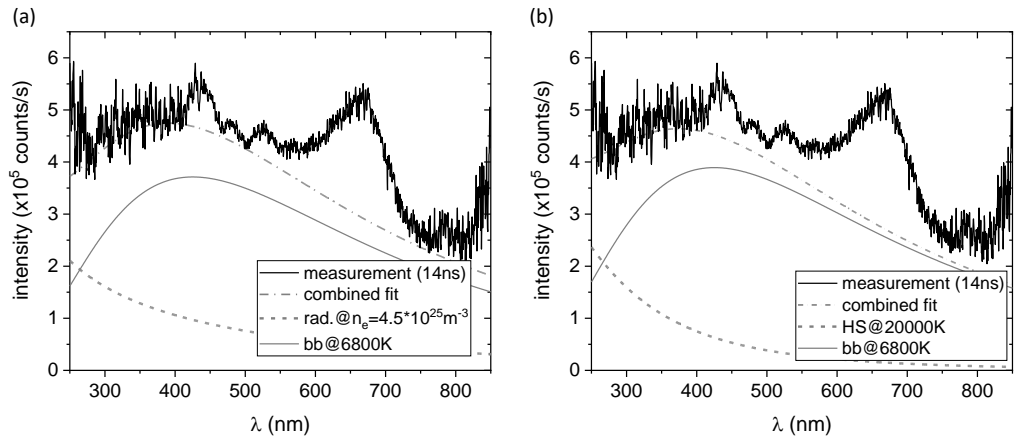


Figure 4.3.7: Fit of continuum radiation to spectrum at 14 ns (a) with black body plus radiative transitions (dashed-dotted grey line) and (b) black body plus hot spot emission (dashed-dotted grey line).

The analysis of the continuum concerning the contributions of black-body radiation with either a hot spot or radiative transition contribution is done in the following. Therefore, both cases are fitted individually to the continuum. This is shown in figure 4.3.7. Two different fits are performed: figure 4.3.7(a) illustrates the sum (dashed-dotted grey line) of black-body radiation at 6800 K (solid grey line) and radiative transitions with an electron density of $n_e = 4.5 \cdot 10^{25} \text{m}^{-3}$ (dashed grey line). Figure 4.3.7(b) shows the sum (dashed-dotted grey line) of black-body radiation at 6800 K (solid grey line) and hot spot emission at 20000 K (dashed grey line). The two cases are discussed in the following.

The spectra of the first 24 ns are illustrated in figure 4.3.8 together with the fits of the different contributions. The graph shows that the continuum can

be described by simple black-body radiation of the tungsten surface during the first 6 ns (a)-(c) with temperatures ranging from 6600 K-8100 K. These temperatures are consistent with findings in literature [60] for a similar discharge and setup. They exceed the typical boiling temperature of tungsten of 5828 K, but as the partial pressure is changing simultaneously, this boiling temperature is varying as presented in figure 4.3.6. The changing pressure is addressed later in section 4.4. As discussed before, the main part of the

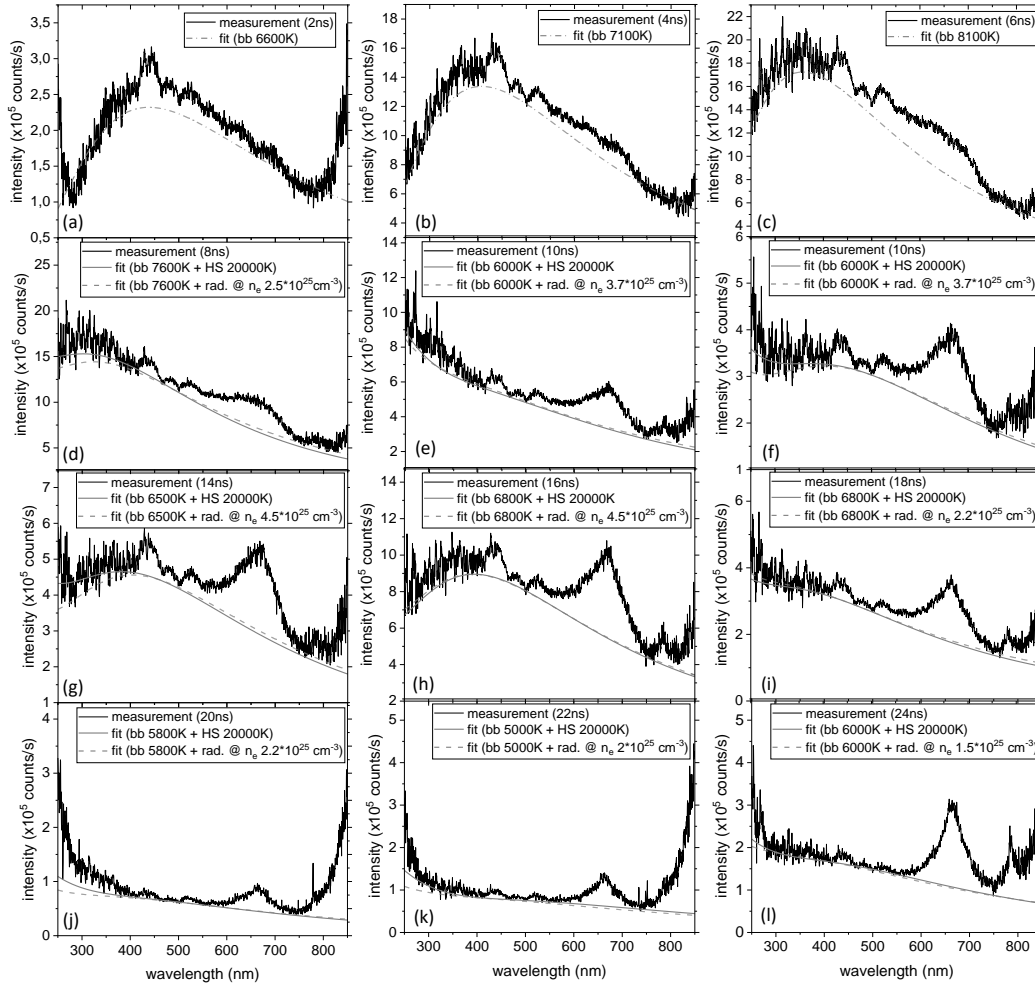


Figure 4.3.8: Emission spectra (black lines) at (a) 2 ns, (b) 4 ns, (c) 6 ns, (d) 8 ns, (e) 10 ns, (f) 12 ns, (g) 14 ns, (h) 16 ns, (i) 18 ns, (j) 20 ns, (k) 22 ns, and (l) 24 ns. The fits according to only black body contribution of the hot tungsten wire (dashed-dotted grey line), black-body radiation plus hot spot on surface (solid grey line) and black-body radiation plus radiative transitions (dashed grey line) are shown.

continuum seems to be shifted more to the UV range over time. Therefore, a simple fit with black-body radiation cannot describe the continuum at later

times. There are two possible mechanisms which could be linked to the increase in UV radiation, namely the building of a *hot spot* or the *radiative transitions*. Both processes are described with respect to their likeliness of appearance.

A so-called *hot spot* (HS) could form on the already hot tungsten surface and add to the continuum especially in the UV. This hot spot with an arbitrarily set temperature of 20000 K would expand over a very small area of the hot tungsten surface. The creation of these hot spots is known from arc discharges [106]. This very localised region of contracted plasma is created by the interaction of thermionic emission and local heating of the surface, which has a non-linear behaviour. The temperature of the hot tungsten surface of the electrode tip is slightly reduced in contrast to the high temperatures at the hot spot [106]. The location of this hot spot could be a protrusion found on the tungsten surface as shown in figure 4.2.2. A comparison of the hot electrode tip area of $A_{electrode} = \pi(25\mu\text{m})^2 = 1963\mu\text{m}^2$ to the assumed area of the tip of a protrusion being $A_{protrusion} = \pi(2\mu\text{m})^2 = 13\mu\text{m}^2$ leads to a percentage of the protrusion/hot spot of 0.6% to the whole hot tungsten surface. This rough estimation matches the percentages of hot spot contribution of the fits as presented in figure 4.3.9 (solid circles). The limited wavelength coverage of the camera in the UV makes it impossible to exactly determine the temperature of such a hot spot. An UV sensitive setup would increase the wavelength range but nevertheless water as a medium is only little transparent. However, the rough estimations of the area and temperature of this hot spot explains the measured continuum in a decent manner together with an overall surface temperature in a range between roughly 6000-8000 K.

The increase of the continuum in the UV could also be described by adding the emission from free-bound (two-body recombination) and free-free (Bremsstrahlung) radiative transitions to the black body emission. For Bremsstrahlung, the interaction between electrons and ions as well as with neutrals needs to be distinguished. The weight of each contribution depends sensitively on the ionisation degree $\alpha = \frac{n_i}{n_i+n_0}$. For higher ionisation degrees, ϵ_{ff}^{ei} and ϵ_{fb}^{ei} dominate, whereas for lower ionisation degrees ϵ_{ff}^{en} dominates. This can be examined by figure 4.3.4. In this graph the electron density is varied for the same neutral density $n_0 = 3 \cdot 10^{28}\text{m}^{-3}$. Therefore, the ionisation degree increases with increasing electron density when quasineutrality is assumed ($n_i = n_e$). Especially the emissivity of the recombination radiation ϵ_{fb}^{ei} is increasing and starts to significantly contribute to the complete continuum radiation ϵ_{cont} .

The electron densities, necessary for the emissivities, are taken from the line broadening described later as a rough estimate. Although it leads to a small ionisation degree of 0.1%, both ϵ_{ff}^{en} and ϵ_{fb}^{ei} , are relevant for the calculated spectrum. With a small percentage of contribution to the continuum radia-

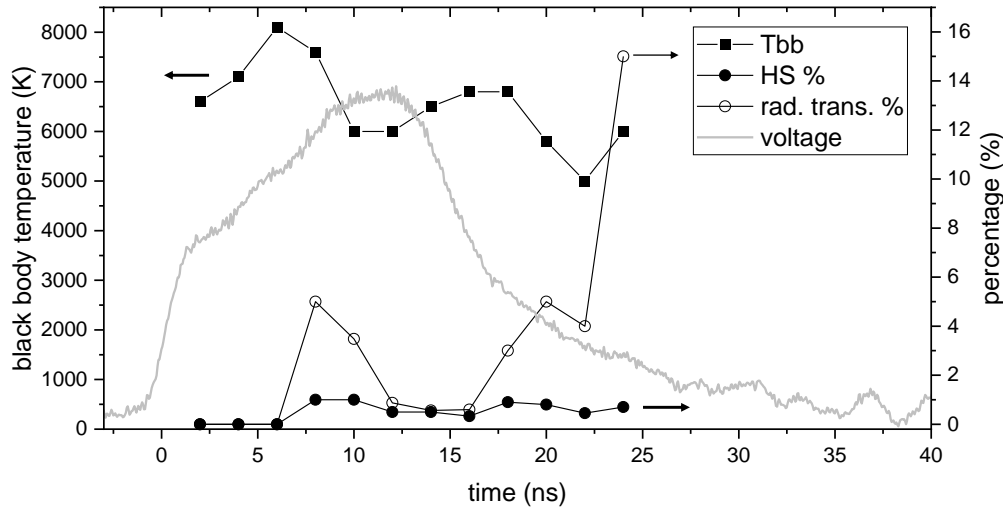


Figure 4.3.9: Hot tungsten surface temperature (black squares), percentage of hot spot at 20000 K (black solid circles) and percentage of radiative transitions (black open circles) at different points in time. The voltage pulse is given in grey as a reference.

tion staying below 5% during the pulse, the continuum can be described in a similar manner to the hot spot attempt. The percentage of this radiation over time is shown in figure 4.3.9 (open circles). At the latest point in time at 24 ns, the percentage of the emission of radiative transitions increases to 15%. This would indicate that the 2-body recombination increases after the initial pulse. This matches with the picture of a propagating plasma inside the liquid leaving a recombination region behind.

It can be concluded that both physical processes can describe the measured continuum especially at lower wavelength. However, it would be necessary to use a highly UV sensitive setup to distinguish between black-body radiation from a hot spot and the radiative transitions described above. They have different dependencies of λ^{-5} and λ^{-2} , respectively. The trend of the spectra at lower wavelength would reveal the process which is most likely do describe the continuum correctly. The evolution of the emissivity of the hot tungsten surface and hot spot are presented in figure 4.3.10.

This graph shows that the setup would need to be sensitive in the low 100 nm range to distinguish between black-body radiation or radiative emission. The latter would further increase, whereas the black-body radiation would decrease at low wavelength as visible in figure 4.3.10. It would be still challenging to analyse the spectra correctly for a more UV sensitive setup due to the absorption of water at lower wavelengths. Furthermore, the camera used for these measurements is not sensitive below 250 nm. It has to be noted

that the quantum efficiency cuts off below 180 nm for all applicable cameras. Due to these reasons, it will not be possible to distinguish between those processes and their contribution to the continuum with this setup.

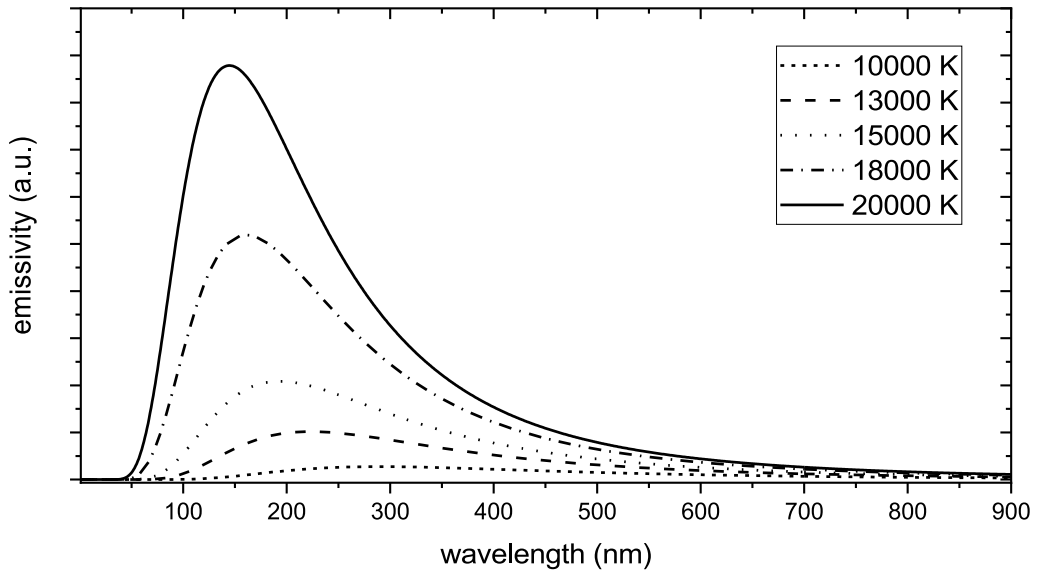


Figure 4.3.10: Emission curve for high temperatures between 10000-20000 K according to Planck's law (equation 2.15).

Nevertheless, a prediction of the likeliness of each process contributing to the continuum is realised. The comparison of the spectra of the first 6 ns make it visible that all three spectra can be described simply by black-body radiation of the hot tungsten surface. For later times, this simple description is not applicable and a higher contribution at lower wavelengths is necessary. Two scenarios are possible after 6 ns.

First, the temperature would increase up to the point where a hot spot is forming and the temperature of the hot tungsten surface begins to decrease back to boiling temperature. Although the appearance of a hot spot at the electrode tip for these plasmas is not discussed previously in literature, it might be a possible process and should be investigated further. It is remarkable that two different mechanisms like radiative emission and hot spot formation with different λ dependencies create such a smooth fit. Additionally, the loss of electrode material over time with a rate of about 1 mm/h could indicate a local heating above the melting point, leading to sputtering of the material.

Second, the temperature is evolving similar to the first case. The evolution follows the voltage curve and is equivalent to the dissipated power in the

system. The continuum at times ≥ 8 ns could also be described by radiative transitions from the propagating plasma in addition to the black body radiation from the hot tungsten surface. This scenario is likely, because recombination between electrons and ions should appear. However, it exhibits only a small percentage in the overall contribution due to the small ionisation degree. The percentage of emission from radiative transitions is $\leq 5\%$ during the pulse and therefore matches this condition.

Line emission

Besides the continuum radiation, line emission is visible in the time-resolved spectra as can be seen in figure 4.3.2. The H_α , H_β , and H_γ Balmer lines

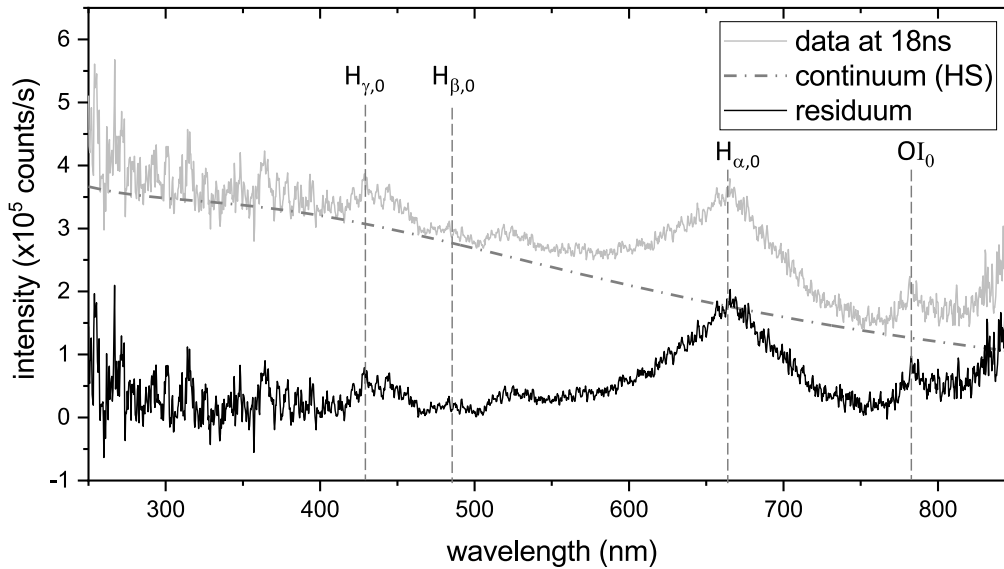


Figure 4.3.11: Time-resolved spectrum at 18 ns after ignition (grey line), continuum resulting from a hot spot (dashed-dotted black line) and the residuum of the continuum subtracted spectrum (black line). The unshifted wavelength positions of H_α , H_β , H_γ and OI are indicated by $H_{\alpha,0}$, $H_{\beta,0}$, $H_{\gamma,0}$, and OI_0 (dashed black lines), respectively.

and an atomic oxygen line at 777 ns are visible in the spectrum. This line emission is generated by so-called bound-bound transitions. In contrast to free-bound and free-free transitions, the energy of an electron within an atom or molecule changes. This leads to a release of photons. As this plasma is ignited directly inside water, line emission from H and O atoms as well as from molecules such as H_2O and OH are expected. Unfortunately, the emission from molecular components could not be identified due to the limited spectral resolution and low signal-to-noise ratio especially at wavelengths be-

low 400 nm.

The H-Balmer lines as well as the atomic oxygen line are analysed. As it can be seen in figure 4.3.11, the visible spectral lines are highly broadened. The full width at half maximum (FWHM) exceeds several tens of nanometer which is most pronounced for the H_α line. The previously calculated continua are subtracted from the spectrum to gain a clearer line emission spectrum. This residuum is then analysed and broadened emission lines can be identified.

It can be seen in figure 4.3.11 that the intensity increases at larger wavelengths. This is an artefact from the intensity calibration due to the reduced sensitivity above 800 nm. As this is influencing the residuum of the atomic oxygen line, the focus of the analysis is put on the H-Balmer lines. Additionally, a red shift from the unperturbed emission line wavelengths (indicated by $H_{\alpha 0}$, $H_{\beta 0}$, $H_{\gamma 0}$ and OI_0) is visible which results also from broadening mechanisms. The role of different spectral broadening mechanisms is discussed in the following for these spectral lines. The different spectral line broadening mechanisms are described in the chapter 2 in detail. Here, the contribution of each process will be discussed:

Instrumental broadening: The broadening contribution according to the setup was determined using a helium-neon laser which is known to produce a narrow emission line (compare section 3.2.5). The instrumental profile has a mostly Gaussian shape with a width of maximum 2.5 nm and is taken into account for the broadening of the H_α and OI emission lines in the measured spectra.

Doppler broadening: The FWHM resulting from Doppler broadening for a Maxwellian distribution at temperature T can be derived from [107], p.157:

$$\Delta\lambda_{Doppler} = \lambda_0 \sqrt{\frac{8 k_B T \ln(2)}{m c^2}}, \quad (4.11)$$

with the unperturbed wavelength λ_0 , the Boltzmann constant k_B , the temperature T , the mass m , and the speed of light c . This leads to very small values for Doppler broadening in the order of fm. This is illustrated in figure 4.3.12.

The FWHM of e.g. the H_α line is about 80 nm at 18 ns. This width is much larger than the Doppler broadening even at very high temperatures. Therefore, this mechanism will be neglected.

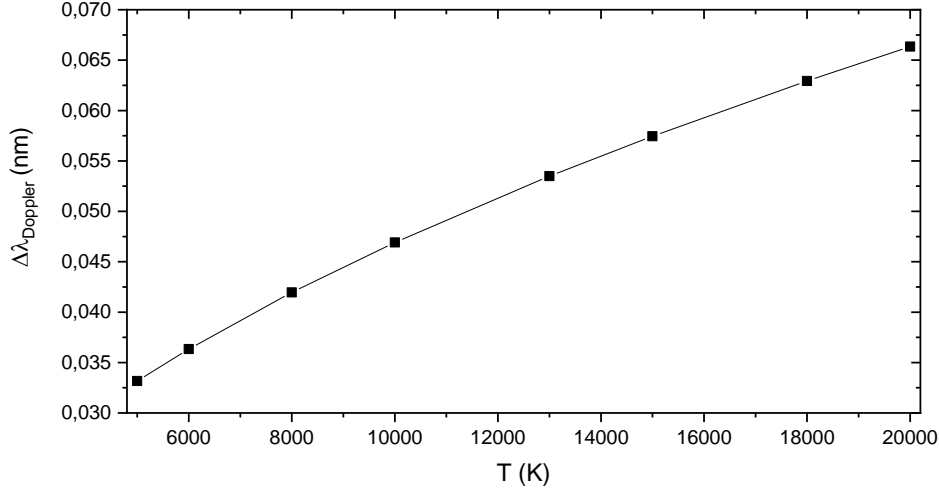


Figure 4.3.12: FWHM induced by Doppler broadening for hydrogen at varying temperatures.

Van der Waals broadening: Collisions of hydrogen with surrounding collision partners is leading to van der Waals broadening. This is a process which is likely to happen for discharges in liquids due to their high electron and species density. According to Konjevic et al. [108], the FWHM of emission lines broadened by van der Waals broadening can be calculated as follows:

$$\Delta\lambda_{vdW} = 8.18 \cdot 10^{-12} \lambda^2 (\bar{\alpha} \langle R^2 \rangle)^{2/5} (T/\mu)^{3/10} n, \quad (4.12)$$

with the wavelength in emission λ in cm, the polarisability of collision partners $\bar{\alpha}$ in cm^3 , the difference between the squares of expectation values of the coordinate vector of the radiating electron in upper and lower state of the transition $\langle R^2 \rangle$, the temperature of the gas T in K, the reduced mass describing the collision of hydrogen and collision partners μ in amu and the density of particles n in m^{-3} . The polarisability of collision partners can be calculated as follows [109, 110]:

$$\bar{\alpha} = \frac{9}{2} a_0^3 \left(\frac{3 E_H}{4 E_{exc}} \right)^2, \quad (4.13)$$

where $a_0 = 5.29 \cdot 10^{-11} \text{ m}$ is the Bohr radius, $E_H = 109737.32 \text{ cm}^{-1}$ is the ionisation potential of hydrogen and E_{exc} is the energy of the first excited level of the perturber. Possible perturbers are water molecules ($\bar{\alpha}_{H_2O} = 1.45 \cdot 10^{-18} \text{ m}^3$), oxygen ($\bar{\alpha}_O = 0.8 \cdot 10^{-18} \text{ m}^3$), and hydrogen ($\bar{\alpha}_H = 0.66 \cdot 10^{-18} \text{ m}^3$) and in the following, water molecules are assumed as perturbers.

The factor of $\langle R^2 \rangle$ can be calculated from the quantum numbers of the transition from an upper to a lower state by $\langle R^2 \rangle = R_u^2 - R_l^2$ with

$$R_u^2 = 0.5 n_u^2 [5 n_u^2 + 1 - 3 l_u (l_u + 1)], \quad (4.14)$$

$$R_l^2 = 0.5 n_l^2 [5 n_l^2 + 1 - 3 l_l (l_l + 1)], \quad (4.15)$$

where $n_{u,l}$ describes the square of the effective quantum number of the upper and lower state and $l_{u,l}$ the angular or azimuthal momentum quantum numbers of the upper and lower states. The square of the effective quantum number itself can be calculated with:

$$n_{u,l} = E_H / (E_{IP} - E_{u,l}), \quad (4.16)$$

where E_H is the ionisation potential of hydrogen, $E_{IP} = 13.6 \text{ eV} = 2.18 \cdot 10^{-18} \text{ J}$ is the ionisation potential of the studied element (here hydrogen), and $E_{u,l}$ is the energy of the upper or lower level of the transition. In case of hydrogen being the studied element, it is $E_H = E_{IP}$.

According to equation 4.12, the van der Waals line broadening is calculated separately for each component. The sum of all components with their relative intensities according to their Einstein coefficients A_{ik} and their statistical weight g_k gives then the FWHM of the van der Waals broadened lines. The values for particle density and gas temperature are taken from the cavitation theory model, which is described in section 4.4.2. The gas density of liquid water $n = 3 \cdot 10^{28} \text{ m}^{-3}$ and temperatures of a few thousand Kelvin during the initial state of the discharge were calculated. This density would correspond to a complete chemical dissociation of water, which is unrealistic. More suitable values would result from assuming hydrogen as the emitter inside the liquid with a reduced density of $n = 1 \cdot 10^{27} \text{ m}^{-3}$ and a temperature equal to the hot tungsten surface of around 7000 K. The reduced density can be estimated from the assumption, that a local region of reduced pressure is present during ignition. The FWHM for both cases are presented in table 4.2 with calculated values of $\langle R^2 \rangle$, $n_{u,l}$ according to $E_{u,l}$, $l_{u,l}$, and $g_k A_{ik}$ from NIST database (tables A.1-A.3 for H_α , H_β , and H_γ , respectively in appendix A).

Table 4.2: FWHMs of van der Waals broadened line profiles for H_α , H_β , and H_γ according to different neutral gas densities and temperatures with water as a perturber.

$n \text{ (m}^{-3}\text{)}$	T (K)	FWHM $_{H_\alpha}$ (nm)	FWHM $_{H_\beta}$ (nm)	FWHM $_{H_\gamma}$ (nm)
$3 \cdot 10^{28}$	15000	238.0	82.6	46.1
$1 \cdot 10^{27}$	15000	7.9	2.8	1.5
$3 \cdot 10^{28}$	7000	189.4	65.7	36.7
$1 \cdot 10^{27}$	7000	6.3	2.2	1.2

The calculated values of van der Waals broadening with a reduced density of $n = 1 \cdot 10^{27} \text{m}^{-3}$ is more realistic, because the FWHM of H_α calculated with $n = 3 \cdot 10^{28} \text{m}^{-3}$ is larger than the overall spectral line width of the measured H_α line of 80 nm.

Furthermore, van der Waals broadened lines are red-shifted by 30 % FWHM of the broadened line [111]. The measured data, however, only shows a red shift of about 5 % of the FWHM. Therefore, van der Waals broadening cannot be the dominating broadening mechanism.

Stark broadening: In the case of Stark broadening being the dominant broadening mechanism, the power radiated per unit frequency from the emitting particle can be described with the Dirac function δ as:

$$\frac{dP}{d\omega} = \frac{\omega^4}{3\pi\epsilon_0 c^3} L(\omega), \quad (4.17)$$

with power P , frequency ω , electric constant ϵ_0 , speed of light c , and the normalised line shape according to [112]:

$$L(\omega) = \sum_{n,m,i} \delta(\omega - \omega_{mn}) | \langle n | e x_i | m \rangle |^2 \rho_m, \quad (4.18)$$

with ρ_m population probability, stationary states m and n . The δ function ensures energy conservation and the sum is called ‘shape’ or ‘profile’ of the line $L(\omega)$.

The FWHM induced by Stark broadening $\Delta\lambda_{Stark}$ depends on the electron density n_e and the electron temperature T_e . This dependence varies for different lines: A temperature variation of a few 10000K leads to a variation of the FWHM of the H_α line of about 5%, whereas the FWHMs of the H_β line and the H_γ line vary by 15-20%. Stark broadening for the H-Balmer lines is simulated by Gigosos et al. [97] as described in chapter 2. According to the calculated tables, an electron density of 10^{24}m^{-3} and a temperature of 20000 K would result in FWHM of 5 nm, 23 nm and 27.8 nm for the H_α , H_β , and H_γ lines, respectively. Therefore, H_β is often used to determine n_e and T_e [108]. The spectrum in figure 4.3.11 shows a highly broadened H_α line, but H_β and H_γ are not as visible and their line intensities are one or two magnitudes smaller. This can be explained by the lower population of the upper states of hydrogen and also lower transition probabilities. Those can be identified by their Einstein coefficients which are $A_{H_\alpha} = 4.41 \cdot 10^7 \text{s}^{-1}$, $A_{H_\beta} = 8.419 \cdot 10^6 \text{s}^{-1}$ and $A_{H_\gamma} = 2.53 \cdot 10^6 \text{s}^{-1}$.

Therefore, in case of a visible H_α line with a FWHM of about 80 nm, the FWHM of H_β and H_γ are much larger. However, the lines are not

as visible as H_α due to their lower line intensity and the high continuum radiation covering the lines. Additionally, a red-shift of about 5% of the FWHM of the broadened line is observed. This value is much lower than necessary for van der Waals broadening and can therefore only result from Stark broadening. To conclude, Stark broadening seems to have a significant impact on the spectral lines, broadens them by many tens of nm and shifts the spectral lines by $\approx 5\%$ of their FWHMs.

Opacity broadening/Self-absorption: A lower state transition of the emitting species needs to be significantly populated for significant self-absorption. This state corresponds to the $n = 2$ state for hydrogen. This results in a modified emission line $I(\lambda)$ with a line profile $P(\lambda)$ and amplitude I_0 under the assumption that the photons pass a layer of absorbing atoms of the same identity as the emitter particles [82]:

$$I(\lambda) = I_0 P(\lambda) \exp\left(-p \frac{P(\lambda)}{P(\lambda_0)}\right). \quad (4.19)$$

The value p describes a function of the total amount of absorbing particles which therefore increases with particle density. The self-absorption effect is possibly appearing because the in-liquid discharge is a highly localised and dense plasma. The emitting hydrogen is affected by a dissociated cloud of surrounding hydrogen atoms. Therefore, the particle density along the optical path is rather high and self-absorption is likely to appear.

Considering only Stark and van der Waals broadening, the emission lines should follow a Lorentzian line profile $P(\lambda)$ according to:

$$P(\lambda) = \frac{1}{\pi} \frac{\frac{\Delta}{2}}{(\lambda - \lambda_0 - \lambda_s)^2 + \left(\frac{\Delta}{2}\right)^2}. \quad (4.20)$$

This line profile changes its shape when self-reversal due to self-absorption is taken into account. The measured spectra are therefore analysed according to all three broadening mechanisms. The fitted spectra are presented in figure 4.3.13.

It can be seen that two different fits are combined for the complete modelled fit (orange). These fits correspond to different levels of self-absorption and, hence, to different regions within the discharge: the *ionisation region* and the *recombination region*. Excitation of hydrogen atoms can still occur in both of these regions. It is assumed that the discharge behaves similar to streamer propagation in gases. The streamer head is corresponding to an ionisation zone at the front of the discharge, ionising water molecules from the surrounding liquid. This *ionisation front* is propagation through the liquid and leaves a *recombination region* behind. This process is illustrated in figure 4.3.14. These two regions are both areas of light emission but the

contribution of self-absorption is different as the optical path is different for those two areas.

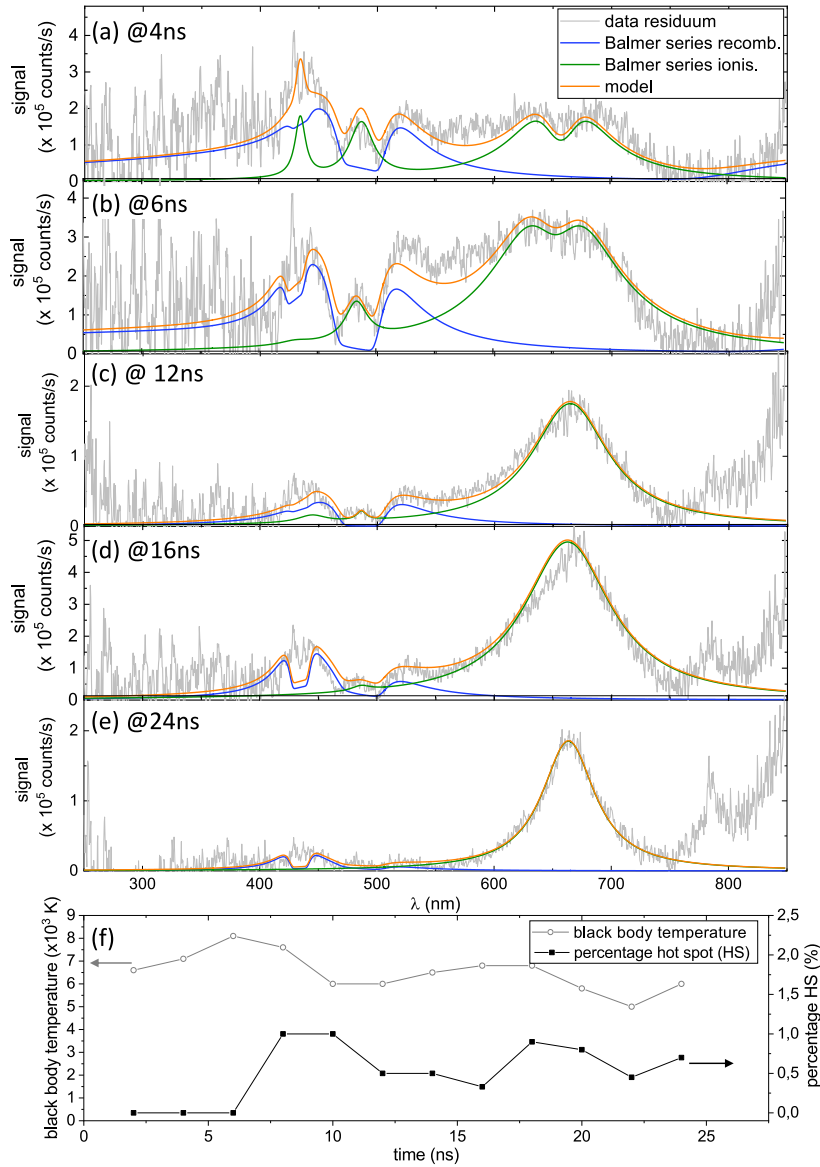


Figure 4.3.13: Continuum subtracted residua (grey lines) corresponding to (a) 4 ns, (b) 6 ns, (c) 12 ns, (d) 16 ns and (e) 24 ns. The signal intensity scale is adjusted for best visibility. The emission from the recombination region (blue lines) and the ionisation region (green lines) is modelled and both combine to the overall fit of the residua (orange lines). (f) The corresponding black body temperatures (open circles) and hot spot contribution (solid black squares) percentages. Adapted from [113].

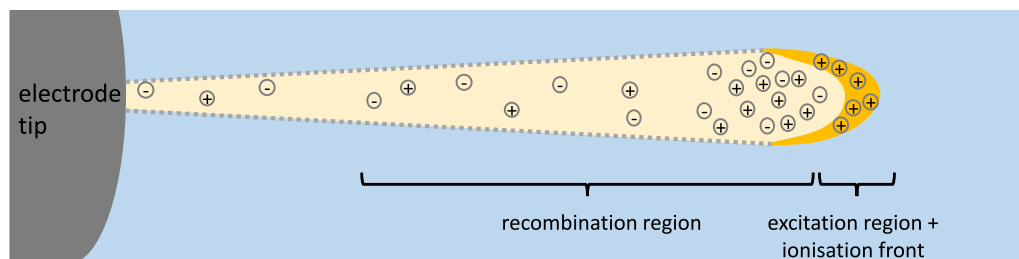
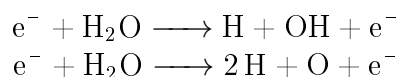


Figure 4.3.14: Sketch of propagating discharge in liquid with an ionisation front (streamer head) and a recombination region behind the streamer head (in analogy to streamers in gases).

At later times, the contribution of light emission from the recombination region decreases until it completely vanishes for 24 ns after the ignition (compare figure 4.3.13(e)). This coincides with the time where the pulse is over and no voltage is applied to the electrode. Furthermore, the light intensity drops drastically (compare figure 4.3.1(b)). It is therefore assumed that the plasma stops propagating at the end of the voltage pulse and the recombination process (as well as ionisation) is not happening. Afterwards, only the Stark broadened H_α line is visible, which is generated by the excited species at the streamer head. The effective lifetimes of the H-Balmer lines are 12.5 ns, 34 ns and 78 ns for H_α , H_β , and H_γ , respectively [114]. These relatively long effective lifetimes can explain the visibility of the H_α emission line after the end of the voltage pulse. Therefore, it is necessary to use this *two-region* approach to model the line spectra precisely, especially during the voltage pulse. The processes over the whole voltage pulse and the corresponding propagation are illustrated in figure 4.3.15.

During phase I, field ionisation starts the discharge and the ionisation front is propagating into the liquid. Hydrogen atoms are created from electron dissociation of H_2O as for example from the following reactions:



The hydrogen atoms can either be ionised or excited by collisions with electrons. For electron energies above 13.6 eV, the hydrogen atoms are ionised whereas electron energies of 10.2-13.6 eV lead to excitation of the hydrogen H-Balmer lines.

Phase II is characterised by the highest applied voltage of 20 kV and the plateau phase. The voltage is not rising anymore and there is no potential difference between electrode tip and ionisation front. The overall intensity of the emission drops due to the lack of new electrons exciting or ionising atoms and molecules. The already excited species relax and also the corresponding

continuum emission is getting weaker for the plateau phase of the voltage pulse. This drop in intensity is the so-called ‘dark phase’ [29, 36].

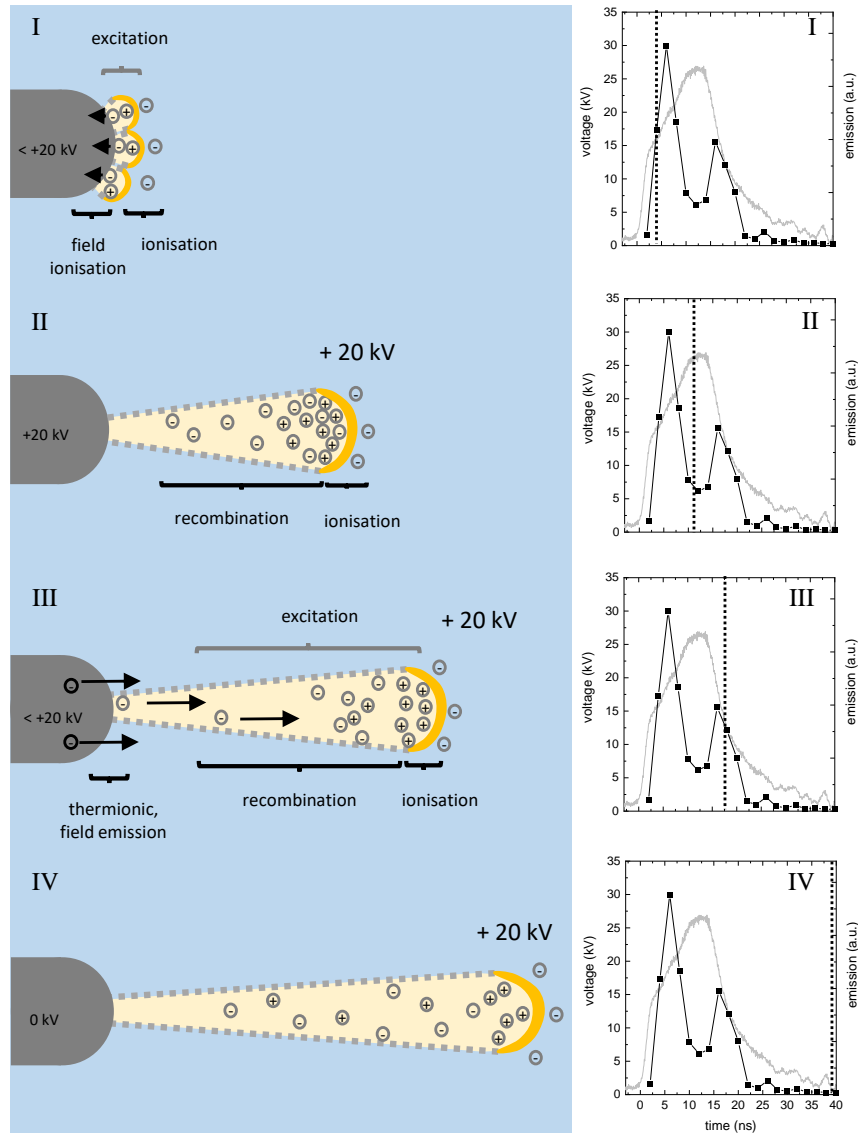


Figure 4.3.15: Sketch of propagation during different phases: voltage rise (I), voltage plateau (II), voltage drop (III), and after-pulse (IV). The voltage pulse (grey) and integrated light emission (black) are shown as a reference with the specific point in time marked by the dashed line.

Phase III describes the drop of the voltage where field emission sets in. Electrons are accelerated out of the electrode into the conductive channel and excite already recombined species along the way. The emission intensity rises again and after reaching a second maximum it drops again to zero. During the drop of the voltage pulse, the energies of the electrons decrease due to the

decrease of the electric field at the electrode tip. At one time in the falling slope of the voltage pulse, the electric field is too small for field emission to occur.

In phase IV, no voltage is applied to the electrode tip and only the streamer head has a positive potential of approximately 20 kV. Because of the lack of electrons to effectively maintain the discharge, the species recombine and the last excited species relax. The primary streamers end. These streamers are faint structures in comparison to the bright emission area in front of the electrode tip as shown in figure 4.3.1(a). This area is blackened out to show the streamer structures in figure 4.3.16.

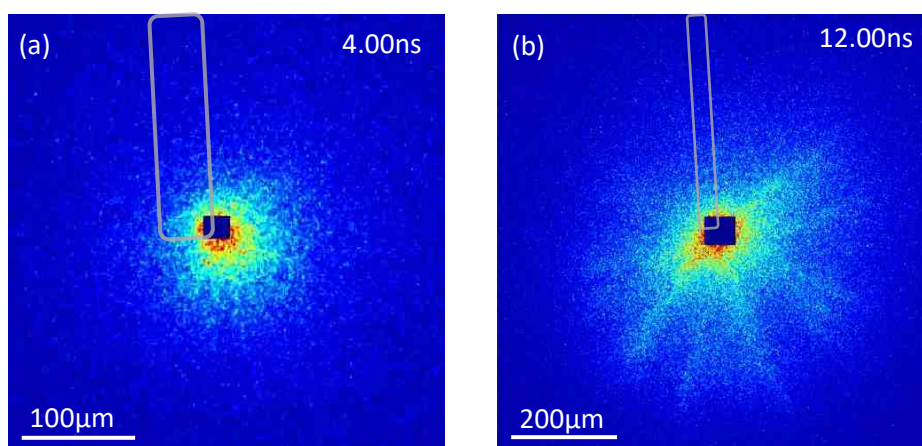


Figure 4.3.16: Single-shot ICCD images presented in false colour with a gate width of 2 ns at (a) 4 ns and (b) 12 ns after ignition with blackened out area of highest intensity. At 12 ns faint structures are visible, which correspond to propagated streamers in the liquid medium.

However, as discussed before, the initial voltage pulse is partly reflected and reaches the electrode again. This results in a re-ignition of the plasma which can be visualised by time-resolved optical emission spectroscopy over a longer period of time.

4.3.2 Re-ignitions and discharge afterglow

To obtain an overview of the spectral line evolution for longer times, including new power input into the discharge by reflected pulses, optical emission spectroscopy is performed with the PI MAX camera. The gate time is 30 ns and time steps of 15 ns are used. Furthermore, the influence of the reflected pulses on the discharge is investigated for different cable lengths which allow longer distances between the reflected pulses (compare section 4.1.1). Figure

4.3.17 illustrates the emission spectrum evolution over a time period of about 300 ns for the 3.4 m (a) and 12 m (b) cable as well as the intensity evolution at 656 nm for all cable lengths (c). The time-resolved spectra for the 6 m, 8.65 m, and 10 m cable are given in appendix B.

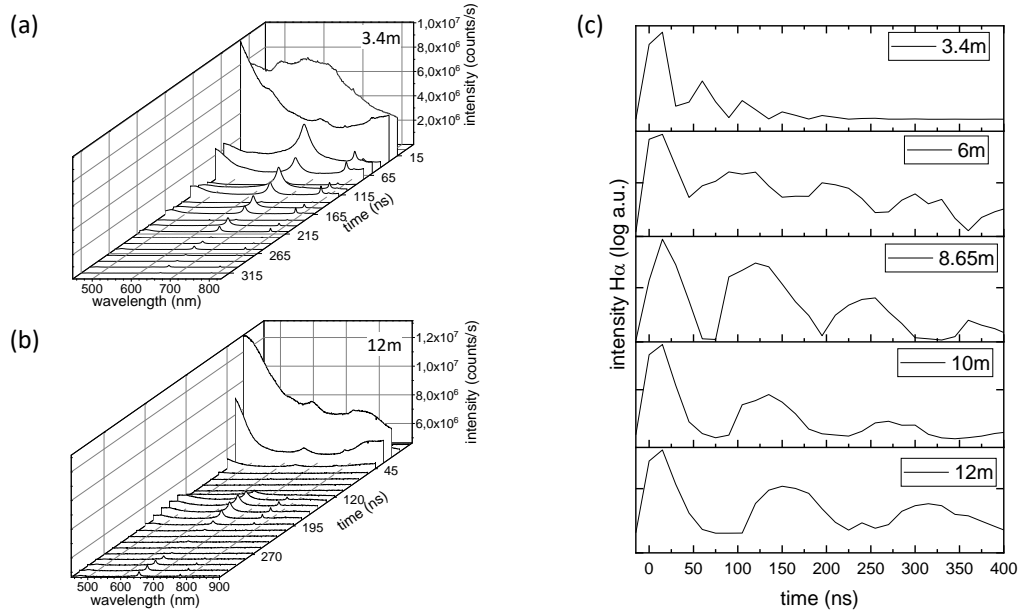


Figure 4.3.17: Temporal evolution of optical emission spectra for the (a) 3.4 m cable and (b) the 12 m cable. The intensity at 656 nm corresponding to the H_α line is shown for all cable length in (c).

The emission spectra for each cable length show a strong continuum at the beginning of the voltage pulse. This continuum was previously analysed with a higher temporal resolution over the time of one voltage pulse. In addition to the continuum radiation, line emission is visible within the time-resolved spectra. The 3.4 m cable exhibits many intensity peaks at 656 nm, corresponding to the H_α line. These emission lines occur with a constant time delay matching the reflections of the voltage pulse inside the cable, leading to re-ignitions of the discharge.

These intensity peaks are also visible for the other cable lengths. However, their appearance is less pronounced compared to the continuum and the distance between these intensity peaks increases with increasing cable length. This is expected due to the longer travelling time within the cable. The H_α emission line is clearly visible at the end of the initial pulse for all measurements indicated by an increase in intensity at around 656 nm on top of the continuum at approximately 30 ns.

The evolution of both the H_α and the OI line can be better analysed by plotting the intensity at the wavelengths 656 nm and 777 nm, respectively for both cable lengths. Figure 4.3.18 shows the temporal evolution of the intensity at 656 nm (a) and 777 nm (b) for the 3.4 m and 8.65 m cables as an example. Both emission line intensities seem to oscillate.

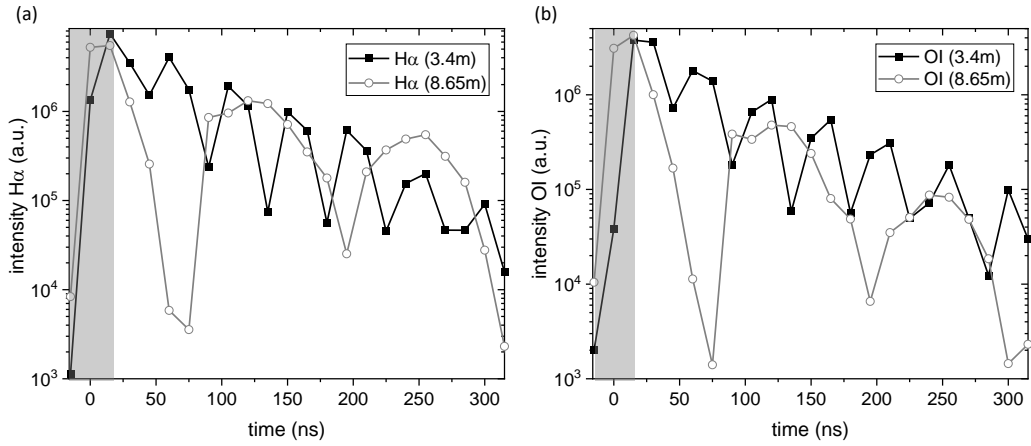


Figure 4.3.18: Temporal evolution of the line intensity of (a) H_α and (b) OI for for the 3.4 m cable (black solid squares) and the 8.65 m cable (black open circles). The grey area marks the beginning of the pulse and the dominating continuum radiation.

The approximated times between the peaks in intensity are 45 ns and 120 ns for emission lines measured with the 3.4 m cable and the 8.65 m cable, respectively. These oscillation times fit to the calculated periods of the oscillating HV pulses induced by the reflections inside the cable (compare section 4.1.1). The delay between the intensity peaks for all cables are presented in table 4.3.

Table 4.3: Comparison of measured time delay between intensity peaks with calculated delay times according to the different cable lengths L from section 4.1.1.

cable length (m)	delay int. peaks (ns)	calc. delay times (ns)
3.4	45	35
6	100	62
8.65	120	89
10	135	103
12	165	124

The difference between the calculated time delays and the estimated times between the peaks in intensity in figure 4.3.18 are an artefact from the longer

camera gate of 30 ns. Additionally, the step width of 15 ns leads to an overlap of emission intensities which is not reflecting the real emission at that point in time, but rather a broader time span of 30 ns. The accumulated light is therefore not reflecting the exact time development and serves only as an estimation. The measurements with the BCS provide more reliable measurements of these time delays between intensity peaks as presented in table 4.1. Summarising, the reflections of the voltage pulse inside the cable, as discussed in section 4.1.1, are also visible in the optical emission spectroscopy measurements. Due to the increase in intensity resulting from the arriving reflected pulses at the electrode, it can be postulated that energy is dissipated into the discharge with every reflected pulse arriving at the electrode. To verify this hypothesis, the electron density derived from the spectral line broadening is investigated in the following.

4.3.3 Electron densities

The electron density of the in-liquid discharge ignited at 20 kV and 15 Hz is determined from the spectral line broadening as discussed in section 3.2.7. The values for the electron density are taken from measurements with high temporal resolution (2 ns gate width) for the 12 m long cable as well as low temporal resolution (30 ns gate width) for the 3.4 m and 8.65 m cables.

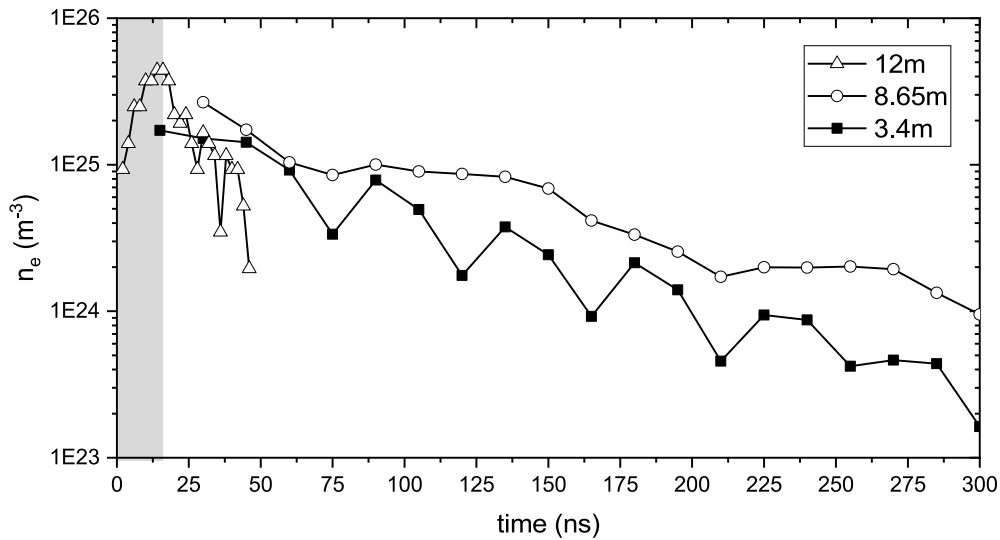


Figure 4.3.19: Time-dependent electron density derived from Stark broadening of H_α for the 12 m cable with $t_{gate}=2$ ns and the 8.65 m and 3.4 m cable with $t_{gate}=30$ ns . The grey area marks the rising voltage front. A voltage of 20 kV and a frequency of 15 Hz was applied for all measurements.

As discussed before, the measurements with the PI-MAX camera were collected with a 30 ns gate. Therefore, the H_α line emission is averaged and the broadening of the H_α line is estimated for this gate width. The measurements taken with the Andor camera show that the FWHM changes also on the short time scale of 2 ns. Therefore, it is assumed that the 2 ns time-resolved measurements are more accurate.

The time-dependent electron densities for the selected cables are presented in figure 4.3.19. Electron densities above 10^{25} m^{-3} are determined for all cable lengths. As discussed in section 2.3.1, electron densities above 10^{25} m^{-3} and below 10^{22} m^{-3} have to be taken with caution. Nevertheless, these values seem reasonable and agree with measurements from literature [56]. A comparison of the OES measurements used for electron density determination found in literature for similar setups can be found in table 4.4. The order of magnitude of the electron densities agrees with the presented measurements, except for [36], where the broadened H_α and OI lines are fitted with the sum of two Lorentzian profiles. Each of these Lorentzian profiles should represent van der Waals and Stark broadening, respectively. However, the interaction of these line broadening mechanisms requires a convolution of both line profiles and not their sum [107, 115, 116].

Table 4.4: Comparison of maximum electron densities in literature determined from spectral line broadening of H_α .

group	setup	U (kV)	t_{rise} (ns)	t_{pulse} (ns)	n_e (m^{-3})
Pongrac et al. [56]	pin-plane	80	2.5	6	$10^{24} - 10^{25}$
Marinov et al. [60]	pin-plane	15	3.7	30	$1.3 \cdot 10^{26}$
Dobrynin et al. [36]	pin-plane	30	0.3	10	$1.5 \cdot 10^{23}$
Grosse et al. [86]	pin-pin	20	2	10	$4.5 \cdot 10^{25}$

Marinov et al. [60] also fitted a time-averaged spectrum over 40 ns with two Lorentzian profiles, but attributed these contributions to two different times within the discharge, which is a reasonable explanation. During their analysis it is stated that the observed red shift is exclusively generated by van der Waals broadening. They argue that Stark broadening can be neglected as an origin for this red shift. However, at very high electron densities this assumption is not valid and the red shift of the H_α line caused by electron impact needs to be taken into account [115, 116].

For a separation of van der Waals from Stark broadening, both line widths and shifts have to be analysed. Here, many works only used Stark broadening [34, 56]. Comparing the results of Pongrac et al. [56] to the here presented data the order of magnitude of the electron density and the pulse shape characteristics are quite similar, but the amplitude of the voltage at the electrode tip is much higher. Pongrac et al. fitted the H_α line with a Voigt peak

function, which convolves both Gaussian and Lorentzian profiles including the Doppler broadening as well as pressure broadening, respectively, neglecting van der Waals broadening. With the assumption that Stark broadening is dominating at later times, the Lorentzian profile is used to determine the electron density with a simplified formula [56]. Their measurements showed a decrease of electron density in time, with a decay time of $\tau_{decay} = 150$ ns.

It can be concluded that additional information about gas density and pressure during the discharge and afterglow phase are necessary in order to interpret the measured optical emission spectra clearly. An estimation of the pressure and temperature can be found in section 4.4.2 based on cavitation theory. Besides that, the comparison of measured line profiles with the simulated line profiles from Gigoso et al. [97] seem to be a valid and a comprehensive method as it includes all relevant mechanisms. Nevertheless, the emission spectra are accumulated over many discharges and a field of view of approximately 1 mm^2 . The difference in electron densities compared to literature (table 4.4) can result from varying setup geometry and liquid properties which can influence the discharge dynamics and therefore also the electron densities. The drop of the electron density appears with a time constant of about 70 ns and 90 ns for the 3.4 m and 8.65 m cable, respectively. These decay times correspond to the decay of the line intensities in figure 4.3.18. The re-occurring voltage pulses at the electrode tip re-ignite the plasma and therefore the emission intensity and the electron density increase shortly due to this new power input. Pongrac et al. [56] also observed a decay of electron density with a time constant of 130 ns (6 ns pulse, 100 kV electrode voltage, 8 m cable, deionised water, pin-to-plane configuration) and linked that to electron recombination. This electron density decrease should, however, only correspond to the decay of oscillating power inside the cable.

The evolution of the electron density can also be compared to the initial applied voltage pulse, which is presented in figure 4.3.20. The start of the voltage pulse is shifted to the rising edge of the electron density. Due to the high density of species inside the liquid compared to gases, the build-up of charges is expected to be faster than the change in voltage. Nanosecond streamer propagation in gases usually show a delay between the rising voltage front and the current because of a delayed build-up of electron density within an ionisation avalanche. This is not assumed for the in-liquid streamer discharge and explains the correlation between the electron density and the voltage pulse. Furthermore, the recombination times of the electrons inside the streamer should occur in the order of picoseconds at such high electron densities. This decay fits to the voltage fall time, which can be expressed through an exponential decay with $\tau_{decay} = 8$ ns. The electrons would therefore balance between their generation in the high electric field and their loss in recombination.

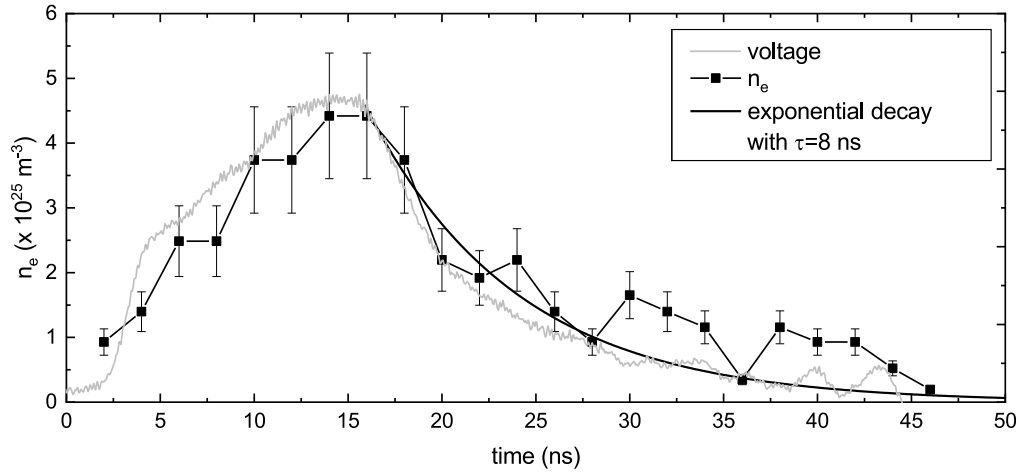


Figure 4.3.20: Voltage pulse (grey) and electron densities (black squares) derived from the FWHM of the H_α line during the first 46 ns. An exponential decay (black line) is modelled using a decay constant of 8 ns. The voltage curve is shifted in time so that its rising front coincides with the rise of electron density. Adapted from [113].

The discussed electron densities mirror the accumulated electron density over the whole discharge area. Certainly, the electron density will distribute differently within the streamer propagation through the liquid. This spatial resolution of one propagating streamer cannot be achieved with OES, which makes modelling necessary. A streamer propagation model can be applied to identify both the movement through the liquid and the electron density within the streamer.

4.4 Cavitation

In general, cavitation describes the formation of gaseous voids inside liquids. As described in section 4.2, during ignition the liquid can rupture and nanovoids are likely to be formed for the described discharge. These nanovoids can grow into streamer channels and further combine to a cavitation bubble. The formation of this cavitation bubble is discussed now. The findings from the experiment are then compared with cavitation theory and are taken in context with the modelling of plasma ignition. Finally, a comprehensive picture of the discharge and cavitation bubble development inside the liquid is derived by combining all experiments and models.

4.4.1 Formation of a cavitation bubble

The nanosecond discharge initiates the creation of a bubble inside the liquid. Furthermore, the propagation of a radial acoustic wave due to the high initial pressure is observed. The temporal evolution of the bubble and the acoustic wave is monitored by shadowgraphs according to the setup in figure 3.2.2. The post-discharge cavitation bubble formation is observed for four different voltages and thus power input into the discharge. The temporal evolution of these discharges is presented in figure 4.4.1.

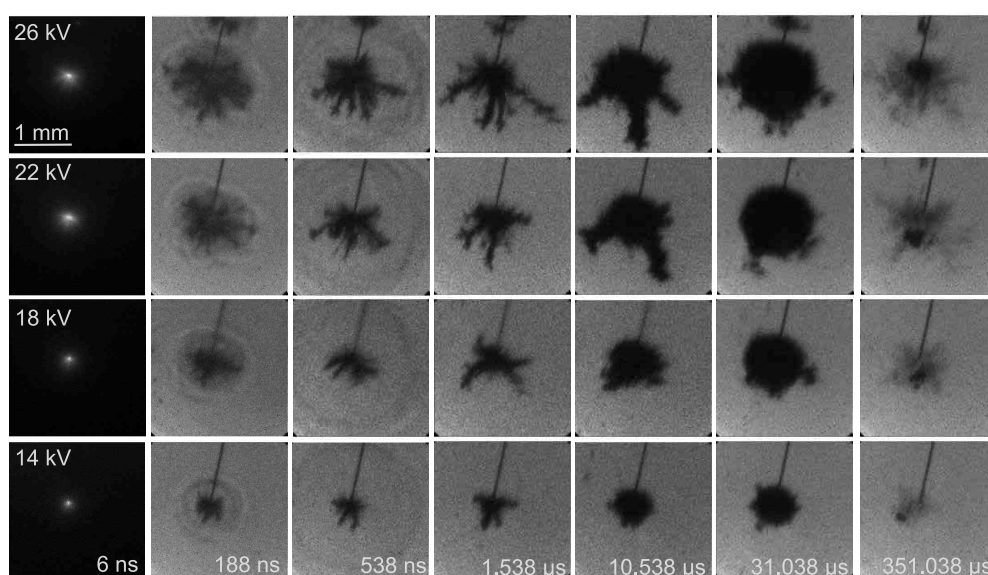


Figure 4.4.1: Shadowgraphs taken for different applied voltages (rows) at different times during the discharge and post-discharge phase (columns). The gate time of the camera varies between a 2 ns gate (at 6 ns), 50 ns gate (at 188 ns, 538 ns and 1.538 μs) and 100 ns (at 10.5 μs, 31.038 μs and 351 μs). The black line from the top is the shadow of the tungsten wire.

The shadowgraphs are taken as single shots with different camera gate times of 2 ns (at 6 ns), 50 ns (at 188 ns-1.538 μs) and 100 ns (at 10.538-351.038 μs). The shorter gate times in the beginning are necessary to avoid the ICCD chip from saturating due to the plasma emission and afterglow. The tungsten wire is visible in the top of each shadowgraph as a thin black line. After the discharge vanishes, the cavitation bubble is visible as black areas on the shadowgraphs due to the difference in refractive index compared to the liquid background. The bubble contains gas atoms and molecules left over from plasma dissociation recombination.

At 188 ns, the gas channels from the streamer expansion inside the liquid become visible adjacent to the electrode tip. Furthermore, the radial acoustic wave can be observed. For the maximum voltage of 26 kV, the streamer gas channels have traveled as far as the wave front. Additionally, a secondary gas channel area can be found at the top of the shadowgraphs directly at the tungsten wire. This leads to the assumption that the surface of the tungsten wire was roughened at that position so that a second discharge could ignite at this protrusion. At 538 ns the acoustic wave propagated further through the liquid but is still visible inside the shadowgraph.

From 10.538 μs onwards, the gas channels start to form a cavitation bubble, which increases in size until it suddenly shrinks and separates from the electrode tip. The whole temporal evolution can be divided into three phases: (I) acoustic wave propagation, (II) cavitation bubble formation and (III) cavitation bubble collapse. These different phases are described in detail:

(I) Acoustic wave propagation

The shadowgraphs at 188 ns and 538 μs show an acoustic wave propagating radially from the point of ignition through the liquid. The acoustic waves are visible for all applied voltages.

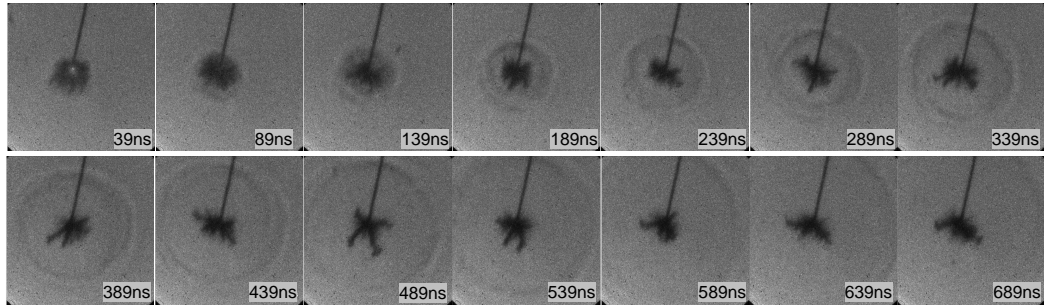


Figure 4.4.2: Shockwave propagating from point of ignition through the medium in circular shape. Plasma generated with 14 kV and 1 Hz. Shadowgraphs are taken for different pulses.

The detailed propagation of the acoustic wave for a 14 kV voltage pulse is shown in figure 4.4.2. Each time stamp of the shadowgraphs is relative to the time of ignition ($t=0$ ns). The camera gate and the time steps between the shadowgraphs are set to 50 ns. The radial acoustic wave is propagating from the point of ignition outwards through the distilled water. The radius of the acoustic wave for each point in time is used to determine its velocity [80]. The radii for different times at 20 kV and 1 Hz and the resulting velocities for voltages of 16-26 kV are given in figure 4.4.3.

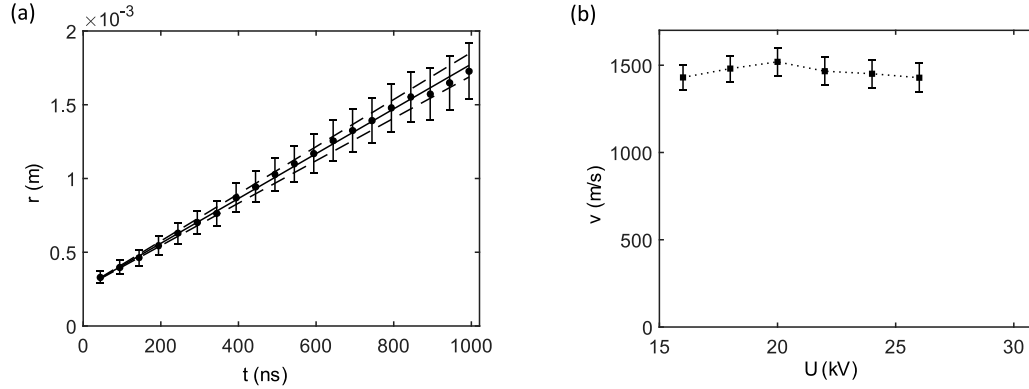


Figure 4.4.3: (a) Radii determined for different points in time and (b) velocities calculated from radii for different applied voltages. Graphs adapted from M. Kai [80].

The average acoustic wave propagation velocity is 1463 ± 78 m/s which is consistent with the speed of sound in water of 1491.50 ± 2.87 m/s at water temperature of 23°C [78]. The acoustic wave can only be determined for times longer than 44 ns due to the light emission of the discharge and the expansion of gas channels around the electrode tip, covering the acoustic wave front in the shadowgraphs (compare first image of figure 4.4.2 at 39 ns). However, the origin of the acoustic wave is expected at the electrode tip. As discussed in the section 2.1.1, a region of negative pressure is surrounding the electrode in the beginning and its formation is faster than the hydrodynamic forces. When the hydrodynamic forces start to react on the negative pressure, a compression layer is formed. The negative pressure layer disappears when the voltage pulse is zero and, therefore, the electric field vanishes which leads to a relaxation of the compression layer which travels away. The dependence of the negative pressure on the electric field is the same as the dependence of the force \vec{F} acting on polar fluids to the electric field [42]

$$\vec{F} \approx \frac{\alpha \epsilon \epsilon_0}{2} \vec{\nabla} E^2, \quad (4.21)$$

with the characteristic constant for the liquid $\alpha \approx 1$ [22] and the permittivity of the liquid ϵ . When the radius of the acoustic wave in figure 4.4.3 is extrapolated to the time $t=0$ ns, the radius is not zero as expected.

This leads to the assumption that the velocity must be higher in the first 44 ns and relaxes then to the speed of sound velocity in water at ambient pressure. Therefore, higher pressures must be present before 44 ns and this *initial* acoustic wave velocity v_{init} is estimated with the assumption that it has a linear behaviour according to:

$$v_{init} = \frac{r_{44ns}}{\Delta t_{init}}, \quad (4.22)$$

with the radius of the acoustic wave r_{44ns} at 44 ns and the time between ignition ($t_0=0$ ns) and the 44 ns. The uncertainty of the time of ignition t_0 is expected to be equal the camera gate time of 2 ns. Acoustic wave velocities in the initial stage of the plasma therefore range between 5600 m/s and 8900 m/s for applied voltages of 16 kV to 26 kV, respectively.

The increase in initial acoustic wave velocity with applied voltage correlates with a higher electric field at the electrode tip for higher applied voltages. According to equation 4.21, this leads to higher negative pressure in the ignition phase. Therefore, the compression layer is pushed outwards with a stronger force acting on it. Furthermore, this acoustic wave has not only to pass a liquid environment in this initial phase but also a gas or gaseous-like environment due to the streamer channels which built up during the discharge. This change of media could lead to a higher expansion velocity of the shock front.

Acoustic wave expansion in liquids are recorded by different groups. Vogel et al. [79] generated a plasma by Nd:YAG laser pulses inside distilled water. They showed that with increasing laser power and pulse length, the initial shock wave velocity increases in the beginning, but always reaches the speed of sound after a few tens of nanoseconds. Despite the different generation of the plasma, the shock wave velocity is much comparable to the presented data. Therefore it is assumed that the initial acoustic wave velocity increases not linearly but rather follows an exponential approximation to the speed of sound in water and might even be a shock wave in its initial stage. Therefore, the previously estimated initial acoustic wave velocities show only a mean velocity during the first 44 ns and are probably higher in the very beginning of the discharge.

The observation of an increased initial shock wave velocity in water decreasing to speed of sound of water have been made by Marinov et al. [61] who used a very similar setup but operated at lower voltages of max. 9 kV. Furthermore, the pulse shape is with 30 ns duration and 5 ns rise time longer than in the presented case and a nickel pin electrode is used instead of a tungsten electrode. Nevertheless, they also report a shock/acoustic wave propagation, bubble formation and the collapse of the bubble. It is also reported that shock waves are created at the propagating streamers inside the liquid [29, 34, 60] which can degenerate into an acoustic wave [60]. The supersonic streamer development is believed to be closely related to the formation of the shock wave which is detected at later times [34]. This phenomenon could not be resolved with the presented setup. However, the shock wave velocities can be used to determine the pressure acting on the shock wave front in the very beginning of the discharge. During that time it might be rather a shock wave than an acoustic wave. Therefore, the shock wave velocity u_S , the velocity of the particles behind the shock u_P and the ambient hydrostatic density ρ_0

have to be taken into account to calculate the pressure from the Rankine-Hugoniot equations [79, 117]. Rice and Walsh [118] calculated the pressure p_s in the region compressed by the shock according to the conservation of momentum of the shock front:

$$p_s = \rho_0 u_s u_p + p_0, \quad (4.23)$$

with the particle velocity

$$u_p = c_1 \cdot \left(10^{\frac{u_s - c_0}{c_2}} - 1\right). \quad (4.24)$$

The density in water at 22°C is $\rho_0 = 998 \text{ kg/m}^3$ [119], the atmospheric pressure is $p_0 = 101325 \text{ Pa}$, the speed of sound of water is c_0 and the parameters c_1 and c_2 can be derived from the Hugoniot curve as $c_1 = 5190 \text{ m/s}$ and $c_2 = 25306 \text{ m/s}$. Rice and Walsh used these calculations for studying shock waves in the range of 2.5-25 GPa but can also be used for values up to 45 GPa. The resulting pressures for the different initial shockwave velocities are presented in figure 4.4.4.

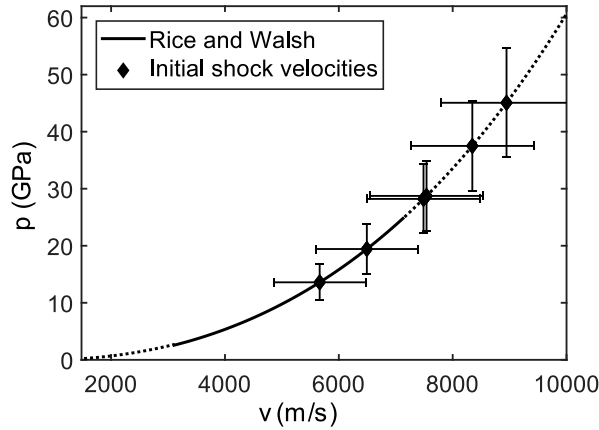


Figure 4.4.4: Pressure in compressed region of shock wave according to equation 4.23 (solid and dotted line) for initial shock wave velocities (squares). The solid line represents the pressure region which was used in the study of Rice and Walsh [118]. (Graph adapted from M. Kai [80]).

The pressure during the initial stage of the discharge can be estimated to be several GPa. This pressure would be high enough to allow the formation of nanovoids discussed before (critical negative pressure $< -24 \text{ MPa}$ [103]). It needs to be mentioned that this pressure is a mean value over the first 44 ns (same for the velocities). Therefore, a time-resolved pressure estimation is not possible. Additionally, as the velocity is here assumed to be linear, an acceleration of the shock wave is not included in the pressure calculations.

As discussed before, it is most likely that the velocities and therefore the pressures are even higher during the time of ignition and the early beginning of the discharge.

(II) Cavitation bubble formation and (III) cavitation bubble collapse

When the internal pressure inside the gas channels is higher after the discharge than the outer pressure of the liquid, these gas channels are forming a bubble structure. This bubble is growing until it reaches its maximum. The quick expansion of the bubble causes a drop of pressure and temperature inside due to the adiabatic expansion. When the input energy and the potential energy of the bubble balance, the maximum size of the bubble radius is reached. Condensation inside the bubble reverses the movement which leads to a collapse of the gas bubble until it reaches its minimum size. This process can be visualised by showing the time-resolved radii of the bubble for different voltages as presented in figure 4.4.5.

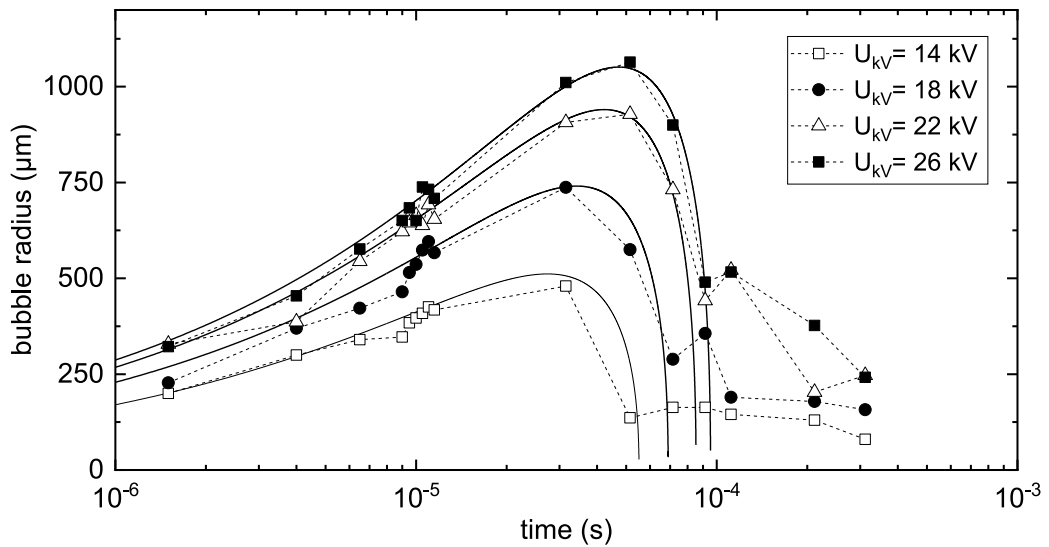


Figure 4.4.5: Temporal evolution of bubble radii for different applied voltages. The solid lines represent modelling results from cavitation theory. Adapted from [86].

The graph shows the temporal evolution of bubble radii for discharges ignited at different applied voltages derived from the shadowgraphs shown in figure 4.4.1. It can be noted that the maximum bubble radius is reached slightly later for higher applied voltages. This can be correlated to the higher electric field strength at the tip which directly influences the total pressure at the

bubble-liquid interface according to:

$$p_{liquid}(R) = \underbrace{p_{E-field}}_{\text{electrical pressure}} + \underbrace{p_{0,gas} \left(\frac{R_0}{R} \right)^{3\gamma}}_{\text{initial pressure}} - \underbrace{\frac{2\sigma}{R}}_{\text{surface tension}} - \underbrace{4\eta \frac{\dot{R}}{R}}_{\text{viscosity}}, \quad (4.25)$$

with the adiabatic coefficient for water $\gamma = 1.33$, $\sigma = 0.072 \text{ N/m}^2$, $\eta = 0.001 \text{ Pa s}$ and with the electrical pressure according to:

$$p_{E-field} = \frac{1}{2} \epsilon_0 E_{HV}^2 \left(1 - \frac{1}{\epsilon_{water}} - \frac{k}{\epsilon_{water}} \right), \quad (4.26)$$

where E_{HV} is the electric field at the tungsten tip, $\epsilon_{water} = 80$ the dielectric constant of water and $k = 1.5$ the coefficient for electrostriction [27].

For higher electric field strengths, the total pressure increases and the bubble can expand more until the energies balance and the bubble collapses. The maximum bubble radius for an applied voltage of 14 kV is 0.6 mm whereas an applied voltage of 26 kV leads to maximum bubble radii of 1 mm. When the bubble collapses, it remains in the vicinity of the electrode tip until it rises due to buoyancy.

4.4.2 Model I: Cavitation theory

The experimental findings from the previous subsection can be benchmarked with theory. For that, cavitation theory based on continuum equations is applied to describe the slow processes during bubble expansion [86]. The high initial pressure derived from the extrapolation of acoustic wave velocities can lead to the rupture of the liquid and nanovoids can be created. A high pressure difference between this nanovoid and the surrounding liquid is created. The nanovoid might be the initial environment for the discharge to ignite, but this is still an open question. As discussed in section 4.2.1, field effects are most likely to play a dominant role in ignition and cannot be neglected. Nevertheless, gas channels are left in the liquid after the discharge and this gas environment can rearrange into a bubble shape due to surface tension.

Radius and velocity of the bubble-liquid interface

Rayleigh gave the first description of the expansion or collapse of a spherical bubble (containing vacuum) in an incompressible liquid in 1917 [72]. The extension to compressible liquids with the bubble propagation at maximum speed of sound in the liquid was established later and is described by the Rayleigh-Plesset equation [73–77]:

$$R\ddot{R} \left(1 - \frac{\dot{R}}{C} \right) + \frac{3}{2} \dot{R}^2 \left(1 - \frac{\dot{R}}{3C} \right) = h \left(1 + \frac{\dot{R}}{C} \right) + \left(1 - \frac{\dot{R}}{C} \right) \frac{R}{C} \frac{\partial h}{\partial t}. \quad (4.27)$$

R is the radius of the interface between bubble and surrounding liquid, \dot{R} and \ddot{R} the velocity and acceleration of this interface, respectively, C the speed of sound at the interface and h is the enthalpy. The last term proportional to $\frac{\partial h}{\partial t}$ can be neglected because the velocity of the acoustic wave is significantly larger than the expansion velocity of the bubble. This simplifies to:

$$R\ddot{R}\left(1 - \frac{\dot{R}}{C}\right) + \frac{3}{2}\dot{R}^2\left(1 - \frac{\dot{R}}{3C}\right) = h\left(1 + \frac{\dot{R}}{C}\right). \quad (4.28)$$

The enthalpy can be described as

$$h = \int_{p_\infty}^{p(R)} \frac{dp}{\rho}, \quad (4.29)$$

with the pressure dependent density of water $\rho(p)$. The calculation of the enthalpy is made using the equation state of water:

$$h = \frac{n}{n-1} \frac{1}{\rho_0} \left(B + p_\infty \right) \left(\left(\frac{p_{liquid}(R) + B}{B + p_\infty} \right)^{\frac{n-1}{n}} - 1 \right), \quad (4.30)$$

with $\rho_0 = 1000 \text{ kg/m}^3$, the coefficient $B = 3000 \cdot 10^5 \text{ Pa}$ and $n = 7$.

The sound velocity C at the interface between bubble and liquid at location R depends on the pressure at this location $p_{liquid}(R)$ and the sound velocity at ambient pressure $c_\infty = 1435 \text{ m/s}$:

$$C = c_\infty \left(\frac{p + B}{p_\infty + B} \right)^{\frac{n-1}{2n}}. \quad (4.31)$$

With these assumptions, the Rayleigh-Pleeset equation can be calculated which yield the temporal developing radius of the bubble-liquid interface and its velocity. The boundary conditions to solve equation 4.28 numerically are $R(t = 0) = R_0$, $\dot{R}(t = 0) = 0$, $p_{0,gas}(R = R_0)$ and the total pressure $p_{liquid}(R)$ is given in the following paragraph.

Pressure

The total pressure at the liquid acting on the bubble $p_{liquid}(R)$ is described in equation 4.25. The electric field pressure at the tungsten tip is calculated with a tip radius of $R_0 = 25 \text{ }\mu\text{m}$ and the electric field at the electrode is approximated with $E_{HV} = U_{applied}/R_0$. This yields a total pressure according to:

$$p_{liquid}(R) = \frac{1}{2}\epsilon_0 E_{HV}^2 \left(1 - \frac{1}{\epsilon_{water}} - \frac{k}{\epsilon_{water}} \right) + p_{0,gas} \left(\frac{R_0}{R} \right)^{3\gamma} - \frac{2\sigma}{R} - 4\eta \frac{\dot{R}}{R}. \quad (4.32)$$

The initial pressure inside the bubble $p_{0,gas}$ is a free parameter but can be set to 0.5 GPa as an estimation from the modeled $R(t)$. This is in agreement with the range of the determined pressures from shadowgraphic measurements in figure 4.4.4.

Temperature

The temperature of the adiabatically expanding gas inside the bubble $T(t)$ can be converted from the numerical solution of the simplified equation 4.27 describing the bubble radius $R(t)$:

$$T(t) = T_0 \left(\frac{R_0}{R(t)} \right)^{3(\gamma-1)}. \quad (4.33)$$

The temporal evolution of all four variables R , \dot{R} , p and T are shown in figure 4.4.6. It can be seen that the velocity of the bubble increases quite fast

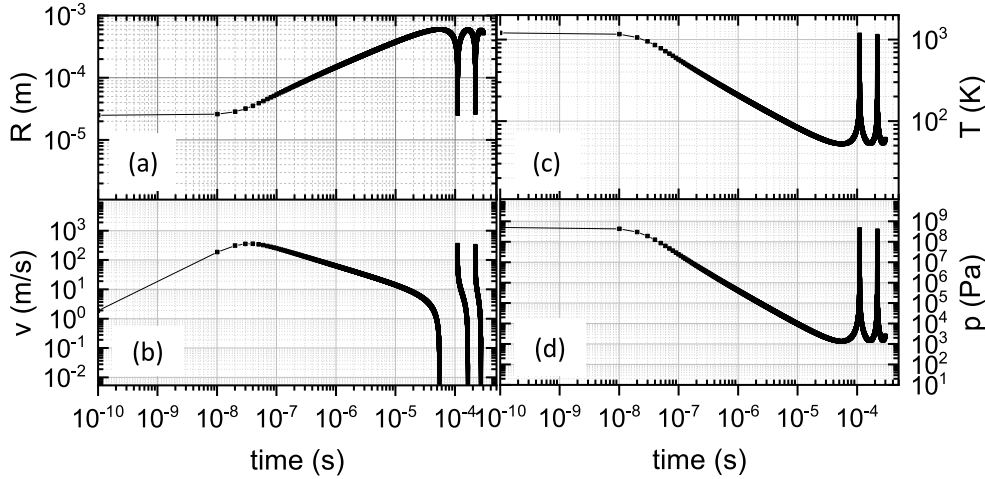


Figure 4.4.6: Temporal evolution of an expanding bubble with a (a) radius $R(t)$, (b) velocity $\dot{R}(t)$, (c) temperature $T(K)$, and (d) pressure at bubble-liquid interface $p_{liquid}(R)$ based on the numerical solution of equation 4.28. The initial values of radius, velocity, pressure and temperature are $R_0 = 25 \mu\text{m}$, $\dot{R}_0 = 0$, $p_0 = 5 \cdot 10^8 \text{ Pa}$ and $T_0 = 1200 \text{ K}$. Adapted from [86].

during the 10 ns pulse, whereas the radius is remaining almost constant. The maximum velocity is reached at approximately 50 ns with 400 m/s. The maximum bubble radius of 600 μm is reached after 50 μs . Afterwards, the bubble collapses and reaches its minimum size at 100 μs . From the expansion to the collapse of the bubble, the pressure inside drops to almost 10^3 Pa and the temperature reaches its minimum at 60 K due to the adiabatic expansion. This temperature is way below the freezing point of water of 273.15 K.

If it is assumed that the plasma is igniting inside water, it is reasonable that the bubble is filled with water vapour. Under this assumption, the water

vapour would undergo phase transitions from gas to liquid to solid phase. This is illustrated in figure 4.4.7.

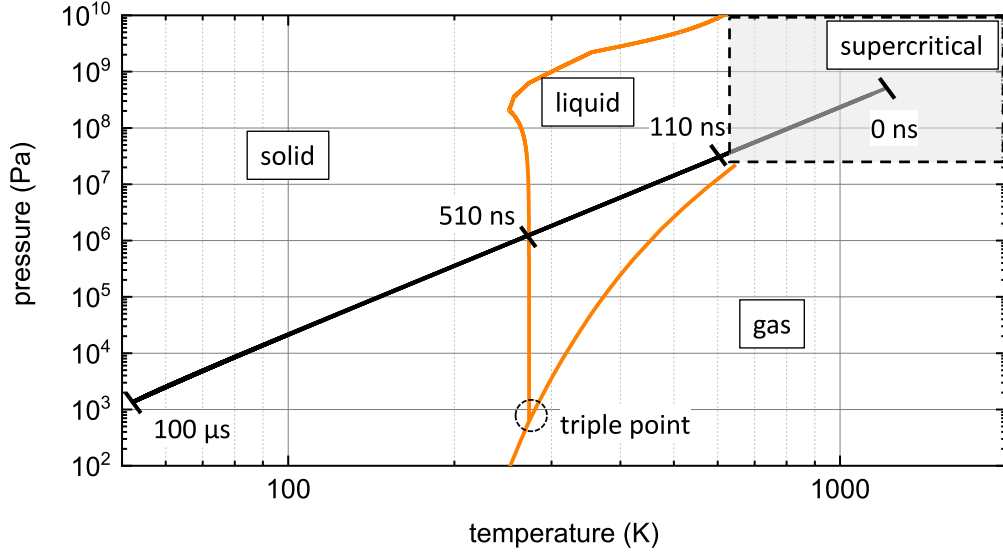


Figure 4.4.7: Change of pressure p and temperature T of the gas inside the bubble during the time of bubble expansion. The orange line indicates the phase boundaries of water. The supercritical state is marked by the grey area. Adapted from [86].

According to the temperature dependent pressure $p(T)$, two phase transitions should occur: (i) from supercritical water vapour to liquid and (ii) from liquid to solid. Such a phase transition describes an equilibrium which might not be applicable. A more realistic description of the gas phase in the bubble should regard the adsorption of gas species at the inner walls of the expanding bubble. The time constant τ before species are lost can be estimated, which can be described by the balance of the surface collision fluence with the total number of gas phase species inside the bubble with radius R [28]:

$$\frac{1}{4}n_{gas}v_{thermal}\beta \cdot \tau \cdot 4\pi R^2 = n_{gas}\frac{4\pi}{3}R^3, \quad (4.34)$$

with the density of gas phase species n_{gas} , the sticking coefficient of water molecules β and the thermal velocity of water molecules $v_{thermal} = \sqrt{3k_B T/m}$ with mass m and temperature T inside a bubble volume with radius R . The condensation occurs at the inner walls of the bubble by adsorbing gas species.

The bubble radius R changes during time of bubble expansion and also the temperature T and the sticking coefficient inside the bubble might change. In the following, values of $\beta = 1$ and $T = 300 K$ are set as a rough estimation. The temperature inside the bubble and the sticking coefficient depend on each

other as a higher temperature leads to an easier desorption of water molecules at the inside of the bubble walls. The time constant for condensation is:

$$\tau = \frac{4R}{3v_{thermal}}. \quad (4.35)$$

Condensation can, therefore, be included in the Rayleigh-Plesset equation by changing the initial pressure inside the bubble $p_{0,gas}$ to $p_{0,gas} \cdot \exp(-t/\tau)$. A comparison between the model with and without condensation is presented in figure 4.4.8.

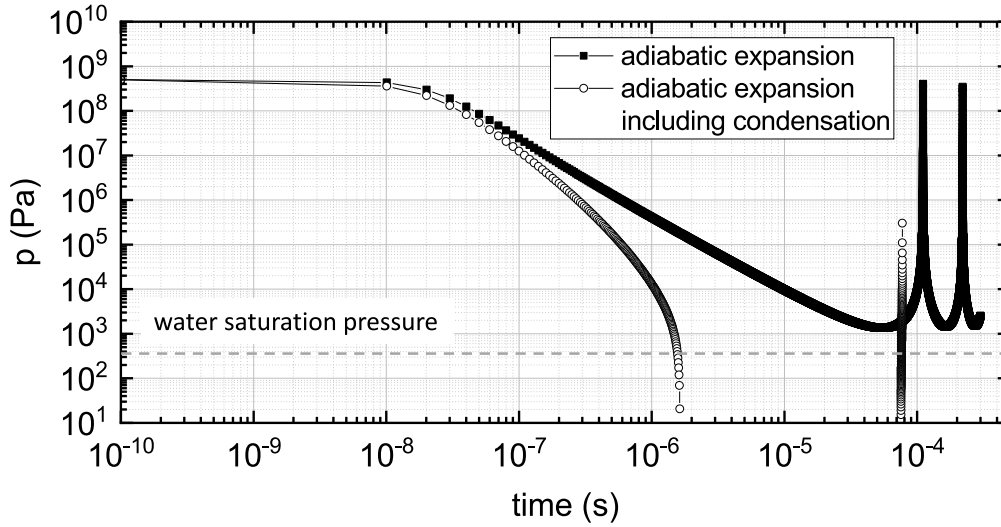


Figure 4.4.8: Temporal evolution of pressure during bubble expansion modelled according to Reyleigh-Plesset with (open circles) and without (solid circles) condensation. The initial pressure is $p_{0,gas} = 0.5$ GPa and the ambient pressure $p_{\infty} = 10^5$ Pa. The dashed grey line marks the water saturation pressure at 2.34 kPa. Adapted from [86].

In the early stage of the discharge, up to $1 \mu\text{s}$ after ignition, the two modelled pressures agree well. However, after $1 \mu\text{s}$, the pressure of the condensation model drops by several orders of magnitude lower than the model without condensation. The limit of this drop in pressure is assumed to be the water saturation pressure at 2.34 kPa where adsorption and desorption balance each other.

The inclusion of condensation into the model is consistent with the experimental observations. First, the development of a spherical cavitation bubble is visible from approximately $10 \mu\text{s}$ after plasma ignition. The pressure inside is presumably much lower than the surrounding due to condensation. A clear contrast is visible in the shadowgraphs. Second, a change in contrast is present in the early phase of the bubble expansion as shown in figure

4.4.9. This change in contrast correlates to a change in density within the discharge environment. Therefore, it is assumed that condensation sets in and a stronger contrast between gas channels and the surrounding liquid develops. The different shadowgraphs can be associated to different pressure stages. At 44 ns, the discharge environment corresponds to supercritical water vapour. Later, at 94 ns condensation starts and afterwards condensation is completed and the contrast between the gas environment and the surrounding liquid is stronger, represented by the shadowgraphs at 144 ns and 194 ns. Therefore, condensation is most likely to appear.

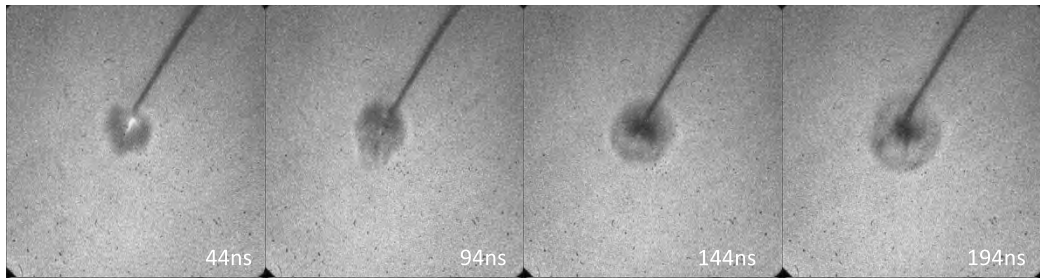


Figure 4.4.9: Shadowgraphs taken with a gate time of 70 ns for 20 kV applied voltage. Condensation of the water vapour inside the gas channels could be indicated by the change of contrast. Shadowgraphs from [80].

A comparison between cavitation theory and experimental observations can also be made concerning the initial pressure during ignition. The extrapolation of acoustic wave velocities from shadowgraphs can be used as an estimate for the initial pressure $\langle p_{initial} \rangle$ as presented in figure 4.4.4. This pressure times an initial volume $V_{initial}$ corresponds to an initial energy $E_{initial}$, which is deposited into the liquid environment during discharge ignition. This initial energy divided by the pulse length of $\Delta t = 15$ ns can be compared to the electrical power $P_{el} = U^2/R$ which is dissipated in the discharge, with a constant electrical resistance R which is estimated with the dissipated power taken from BCS data according to section 4.1.3. The dissipated energy for this measurement ($E_{diss} = 2.4$ mJ, $U = 20$ kV) during the whole pulse results in an electrical resistance of $R = U^2 \cdot \Delta t / E_{diss} = 2.5$ k Ω . Therefore, the initial pressure can be scaled with the applied voltage according to:

$$\langle p_{initial} \rangle = \frac{U^2}{R} \cdot \frac{\Delta t}{V_{initial}}. \quad (4.36)$$

The fitting pressure of $p_{0,gas}$ for cavitation theory is set in such a way that the expansion of the cavitation bubble can be described for an initial cavitation bubble radius R_0 of 25 μm . Those pressures are plotted in figure 4.4.10. Here, $\langle p_{initial} \rangle$ and $p_{0,gas}$ are in the same range, but show differences in

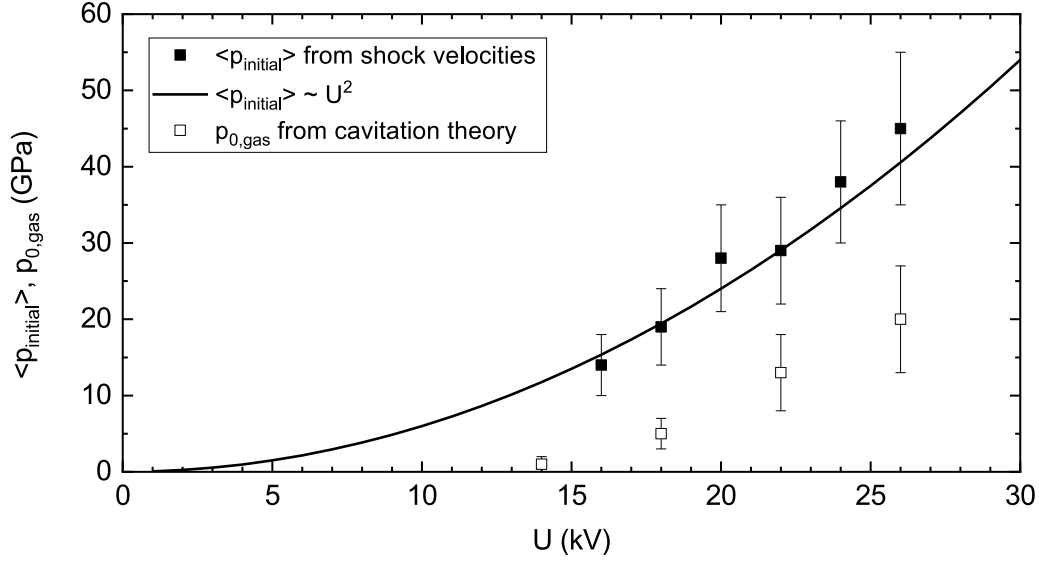


Figure 4.4.10: Averaged initial pressures $\langle p_{initial} \rangle$ of the discharge extrapolated from shock wave velocities within the first 44 ns (black squares) and fitting pressures $p_{0,gas}$ derived from cavitation theory for an initial bubble radius of $25 \mu\text{m}$ (open squares) for different applied voltages U . The solid line demonstrates the scaling of $\langle p_{initial} \rangle \propto U^2$ (solid black line). Adapted from [86].

absolute numbers. However, $p_{0,gas}$ describes the pressure inside the cavitation bubble at 10-20 ns after ignition, whereas $\langle p_{initial} \rangle$ denotes the average pressure during the first 44 ns after ignition. Due to an expected continuously decreasing pressure, it is comprehensible that $p_{0,gas}$ is systematically lower than $\langle p_{initial} \rangle$. In addition to that, the fitting of the initial pressure $p_{0,gas}$ and the initial volume V_0 from cavitation theory can be used to determine the potential energy E_0 that is dissipated by plasma generation:

$$E_0 = p_{0,gas} V_0 = p_{0,gas} \frac{4\pi}{3} R_0^3. \quad (4.37)$$

This energy drives the expansion of the cavitation bubble after plasma ignition. The maximum cavitation bubble radius R_{max} and the time of bubble collapse $t_{collapse}$ depending on the initial potential energy E_0 are presented in figure 4.4.11. The bubble radius R and the time of collapse $t_{collapse}$ derived from cavitation theory both scale with $\sqrt{E_0}$.

Finally, with the fitting parameter for the initial pressure $p_{0,gas}$ in a bubble with an initial radius of $25 \mu\text{m}$ and an ambient pressure p_∞ , the bubble radius evolution shown in figure 4.4.5 can be described with the parameters given in table 4.5.

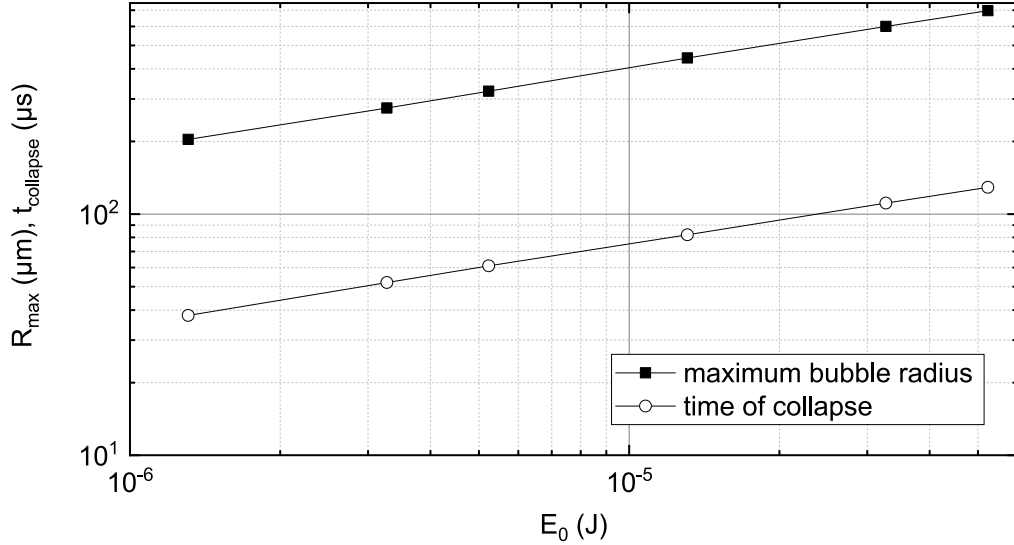


Figure 4.4.11: Maximal radius R_{max} and time of collapse $t_{collapse}$ depending on the initial potential energy E_0 . Adapted from [86].

It can be seen that the fitting with these parameters is in excellent agreement with the measured bubble radii shown in figure 4.4.5. It has to be noted that usually the ambient pressure should be 10^5 Pa (1 bar). However, small deviations within the fitting procedure have to be taken for the ambient pressure, ranging from $3\text{-}4.2 \cdot 10^5$ Pa in order to get a good fit. These deviations from atmospheric pressure can arise from the shock wave travelling from the point of ignition outwards relaxing into a sound wave. However, its movement is restricted by the outer walls of the plasma chamber, where the acoustic wave can be reflected which would lead to a propagation towards the expanding cavitation bubble. This reflection is possible for multiple times which would lead to an increase in ambient pressure and might lead to a slightly faster collapse of the cavitation bubble.

Table 4.5: Fitting parameters $p_{0,gas}$ and p_∞ for different applied voltages.

U (kV)	$p_{0,gas}$ (Pa)	p_∞ (Pa)
14	$1 \cdot 10^9$	$3 \cdot 10^5$
18	$5 \cdot 10^9$	$4 \cdot 10^5$
22	$13 \cdot 10^9$	$4.2 \cdot 10^5$
26	$20 \cdot 10^9$	$4.2 \cdot 10^5$

Summarising, the model depends sensitively on the initial pressure for the small initial gas bubble. This radius is assumed to be $25 \mu\text{m}$ estimated from the electrode tip dimension. However, the initial dissipated energy $p_{0,gas}V_0$ is the crucial parameter as a higher pressure and smaller bubble volume leads to the same modelling results. The modification of the model with a

higher initial pressure and a lower initial volume are theoretically possible and could be used as a boundary condition for the model. By applying this, the simulation faces numerical difficulties, because the initial velocities are then closer to the speed of sound. Hence, the initial radius of $25\ \mu\text{m}$ is used and an extrapolation to smaller radii is applied.

4.4.3 Model II: Plasma ignition

Model I can be applied to make assumptions about the ignition of the plasma inside the liquid. It is assumed that the cavitation bubble expands from an initial bubble with a radius of $25\ \mu\text{m}$. However, the bubble expansion can only start after the plasma, because the initial discharge is dominated by fast energy transport compared to mass transport in this phase.

Therefore, a bubble with $25\ \mu\text{m}$ radius describes only the system after the discharge and an even smaller region must be present at the beginning of the discharge. Nanopores formed previously to the discharge occur at negative pressure differences between electrode and liquid of $2.4 \cdot 10^7\ \text{Pa}$ [103]. This value can only be reached for tip curvatures of less than $5\ \mu\text{m}$ for an applied voltage of $20\ \text{kV}$. This is consistent with the observations of small protrusions on the tungsten surface from Lukes et al. [99, 120] and the previous section 4.2.1. Therefore, the formation of nanopores due to a local field pressure of $2.4 \cdot 10^7\ \text{Pa}$ is assumed [42] for an irregularity on the surface with a $5\ \mu\text{m}$ radius. The inertia of the liquid prohibits the liquid to move on the time scale of $10\ \text{ns}$. This is consistent with model I where $R(t)$ changes less than $1\ \mu\text{m}$ (see also the calculations of Tereshonok et al. [28]).

Whith the start of the ignition, the water is brought into the plasma state. It is assumed that the initial energy E_0 is constant over the whole pulse length of $10\ \text{ns}$ and only spreads by heat conduction. The initial energy $E_0 = 3.2 \cdot 10^{-5}\ \text{J}$ (equivalent to a power of $P = 3.3\ \text{kW}$ during a $10\ \text{ns}$ pulse) can be converted into a temperature if a species density of $3 \cdot 10^{28}\ \text{m}^{-3}$ water molecules is assumed. With these conditions two cases can be discussed seperately, *ignition* and the *beginning of bubble expansion*:

- i) *ignition*: The energy $E_0 = 3.2 \cdot 10^{-5}\ \text{J}$ is dissipated into the initial volume with a radius of $5\ \mu\text{m}$ during ignition, which corresponds to a particle energy of around $12.7\ \text{eV}$ for a species density of $3 \cdot 10^{28}\ \text{m}^{-3}$. This is above the ionisation energy of water molecules of $12.62\ \text{eV}$ and, therefore, an ionisation degree of 100% can be expected. This rough assumption can only be proceeded, because the energy of particles varies strongly with small changes in the number density of species.

This initial energy can be expressed as a temperature T_0 to estimate the initial pressure according to the ideal gas law $p_0 = n k_B T_0 \approx 60\ \text{GPa}$

with the species density n . This pressure is in agreement with the estimated initial pressure from the acoustic wave propagation averaged over the first 44 ns. Due to the averaging over 44 ns, an even higher pressure during the ignition is expected. Additionally, the heat conduction velocity equals to the speed of sound in water of 1435 m/s after plasma ignition. By assuming this, an initial bubble volume during ignition would expand to a volume with radius of 25 μm within 14 ns. This is in good agreement with the pulse length from the HV pulser.

- ii) *beginning of bubble expansion*: The bubble expansion is marked by a cavitation bubble radius of 25 μm . According to model I, temperature and pressure at that time are 1200 K and 0.5 GPa for $U=14$ kV, respectively. This upper limit for the radius of the cavitation bubble is restricted by an upper limit for the volume V_{limit} to which the initial energy spreads. This leads to the evaporation of water vapour. The cavitation bubble should be limited by an average temperature which is below the boiling temperature of $T_{limit}=373$ K. Therefore, the critical volume is $V_{limit} = E_0/(nk_B T_{limit}) = 2.07 \cdot 10^{-13} \text{m}^{-3}$ leading to an upper limit of the radius for the cavitation bubble of $r_{limit} = \sqrt[3]{3/4 \cdot V_0/\pi} = 37 \mu\text{m}$. This is very consistent with the starting condition of model I with $R_0 = 25 \mu\text{m}$ showing a good agreement of model I and model II.

4.4.4 Combination of model and experiment

It can be stated that model I describing *bubble expansion* is dominated by mass transport over energy transport. The bubble is driven by the adiabatic expansion of the hot trapped gas inside the cavitation bubble in first order. Hence, the energy transfer at the bubble-liquid interface occurs on a longer time scale. In contrast to that, model II specifying *plasma ignition* is characterised by faster energy transport than mass transport. Therefore, water is converted into plasma or hot gas during the pulse of approximately 10 ns. Nevertheless, a model on the molecular level is needed to include the possible formation of nanopores and the transport of energy and radiation after discharge ignition in more detail.

These two models concerning ignition and bubble expansion give a decent estimation of the processes in the early phase of the discharge. Also later times long after the discharge itself are consistent with experimental findings. This is illustrated in figure 4.4.12.

The temporal evolution of the discharge and post-discharge cavitation bubble development is presented for specific points in time. The powered electrode is shown by the grey bar coming from the top. The different time steps are marked by a)-g):

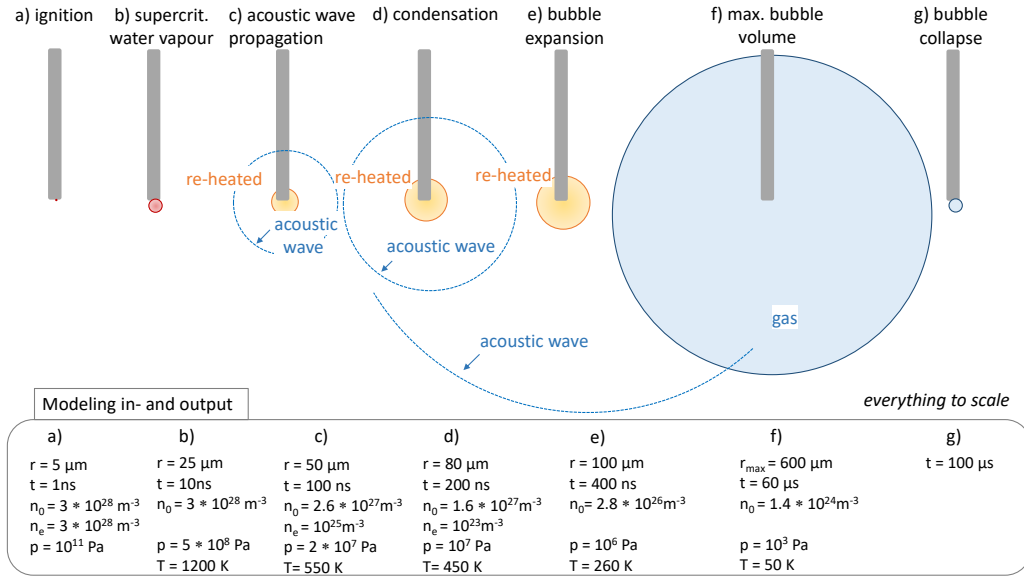


Figure 4.4.12: Temporal evolution of the discharge and the resulting processes such as shockwave propagation and cavitation bubble formation based on experimental findings and modelling.

Figure 4.4.12 a) The high voltage applied to the tip electrode leads to field ionisation of water molecules or field emission at protrusions on the tungsten surface, depending on the voltage pulse polarity. The generated electrons are presumably accelerated inside previously formed nanopores, created through a high negative pressure difference of 24 MPa between electrode and surrounding water. From the energy balance an ionisation of 100% of liquid water can be deduced at $3 \cdot 10^{28} \text{m}^{-3}$. These initial electrons are the start of the discharge. The estimation of the electron density during the initial pulse, however, is determined to be in the order of 10^{25}m^{-3} for the 12m long cable measurements. This results in a small ionisation degrees in the order of 10^{-3} . Therefore, it can be assumed that the species density is smaller. The electrical energy from the HV nanosecond source is dissipated in a small region with a radius of $5 \mu\text{m}$ and the liquid is converted into the plasma state. The energy transport is much faster than the mass transport during this stage due to the inertia of the liquid.

Figure 4.4.12 b) After the end of the pulse, the mass transfer dominates over the energy transport and the high initial pressure causes cavitation. The hot gas from the discharge drives the cavitation bubble expansion. The best fit is achieved for an initial bubble volume with a radius of $25 \mu\text{m}$ and initial pressures of the hot gas of $p_{0,gas} = 1-20 \cdot 10^9 \text{Pa}$. This boundary condition leads to an energy dissipated into the bubble by the discharge which can be estimated from the initial pressure

$p_{0,gas} = 0.5 \cdot 10^9 \text{ Pa}$ to $E_0 = p_{0,gas} V_0 = 3.2 \cdot 10^{-5} \text{ J}$ at $U=14 \text{ kV}$. Due to the particle energies resulting from this initial energy, full ionisation within the initial volume with a radius of $5 \mu\text{m}$ can be assumed. The temperature of the heated water/hot gas reaches 1200 K inside the cavitation bubble due to strong thermalisation. This stage corresponds to *supercritical water vapour*, because a phase transition from the initial liquid at 300 K to a hot water vapour at 1200 K at liquid water molecule density occurs. The expansion has not yet begun.

Figure 4.4.12 c) The adiabatic expansion of the cavitation bubble starts. Therefore, pressure and temperature inside the bubble decrease with increasing bubble radius. Furthermore, a sound wave is starting to propagate from the electrode tip into the liquid. The high initial pressure leads to a formation of an acoustic wave with fast velocities which relaxes to the speed of sound in water at ambient pressure. Compared to bubble expansion, the sound wave travels faster. Simultaneously, electron densities between $\approx 10^{23}\text{-}10^{25} \text{ m}^{-3}$ are observed which decay with a time constant of approximately 70 ns for measurements with the 3.4 m cable. This time constant agrees well with the ring-down time of the re-occurring HV pulses at the electrode of 60 ns . Each re-occurring HV pulse leads to a partial energy dissipation into the liquid and therefore an increase in electron density. This is observed experimentally.

Figure 4.4.12 d) During the expansion of the cavitation bubble, condensation at the inner walls of the bubble occurs. This causes the pressure to drop significantly during the time between 100 ns and $1 \mu\text{s}$.

Figure 4.4.12 e) The bubble expands further due to its inertia. During the expansion, the temperature decays by two orders of magnitude whereas the pressure drop is decreasing to 100 Pa when the maximum bubble size is reached (f).

Figure 4.4.12 f) The cavitation bubble has expanded to its maximum size with a radius of $1.2 \mu\text{m}$ reached at $100 \mu\text{s}$ for an applied voltage of 26 kV . At this point in time, energy dissipated into the bubble equals its potential energy.

Figure 4.4.12 g) The pressure of the surrounding liquid dominates over the inner pressure in the cavitation bubble. Condensation inside the bubble reverses its movement and a fast collapse occurs. The outer liquid pressure is slightly above 1 bar due to the reflected sound waves at the plasma chamber walls. The condensation of the hot gas inside the bubble leads to a small size after the bubble collapse. Without gas condensation, the collapsing bubble would compress the confined gas and an oscillation of the bubble size would appear over time. This is not observed in the measurements and, therefore, condensation seems to be a valid explanation.

The combination of model and experimental results show the efficiency of the in-liquid nanosecond plasma. With ignition, an area around the HV electrode tip is instantly converted into the plasma state and a supercritical state is reached. This supercritical fluid is characterised by a coupling of generated reactive species in the plasma and the surrounding liquid species. When the cavitation bubble is expanding, these reactive species condense at the bubble walls and diffuse into the liquid which leads to very efficient reactions inside the liquid. In comparison to that, plasmas ignited above liquids are less efficient due to the small Henry constants restricting the transfer of reactive species from the gas phase into the liquid. Furthermore, plasmas ignited inside liquids with HV pulses with long rise times would also result in a less efficient reactive species transfer because a cavitation bubble is then formed before ignition takes place and supercritical water may not occur inside the bubble.

4.5 Chemistry generated by nanosecond plasma in liquid

The analysis of the liquid chemistry induced by the plasma is challenging on these short timescales. After plasma ignition most of the species quickly recombine. Therefore, only longer lived species as H_2O_2 can be detected via optical absorption spectroscopy with a calorimetric method. The knowledge of the in-liquid chemistry is crucial for treatment of surfaces induced in the vicinity of the discharge inside the liquid.³

4.5.1 H_2O_2 production

The production of H_2O_2 after plasma treatment with the nanosecond pulsed discharge inside distilled water has been measured by Nenbankaeo [121] and Chauvet et al. [70]. The generation efficiency of H_2O_2 has been determined depending on the treatment time, frequency, electrode distance, and applied voltage. The concentration of H_2O_2 inside the treated liquid is analysed ex situ by optical absorption spectroscopy based on a calorimetric method as discussed in section 3.2.6. The continuous spectra generated by H_2O_2 between 215 nm and 375 nm can be measured directly with this experimental method [95]. However, the intensity of the H_2O_2 signal has been enhanced by analysing the liquid with a Spectroquant (R) (Merck KGaA) test kit. This test kit is based on the neocuproine copper(II) method described by Tüttem et al. [122] as explained in section 3.2.6. The different variations of parameters are shown in table 4.6:

³The measurements presented in this chapter are performed by C. Nenbankaeo during his Bachelor thesis [121] and are further published in [70].

4.5. CHEMISTRY GENERATED BY NANOSECOND PLASMA IN LIQUID

Table 4.6: Parameters applied for measurements of H_2O_2 production inside distilled water. One parameter is varied (rows) whereas the other parameters are kept constant (columns).

constant \ varied	$t_{treatment}$ (min)	f (Hz)	U_{appl} (kV)
$t_{treatment}$ (min)	3,5,10,20	15	20
f (Hz)	5	1-100	20
U_{appl} (kV)	10	15	15-30

The measurements showed a linear increase of H_2O_2 concentration with increasing treatment time and frequency. In addition, the variation of the applied voltage also showed an increase in H_2O_2 concentration as seen in figure 4.5.1. However, the data exhibits two different slopes. The first is

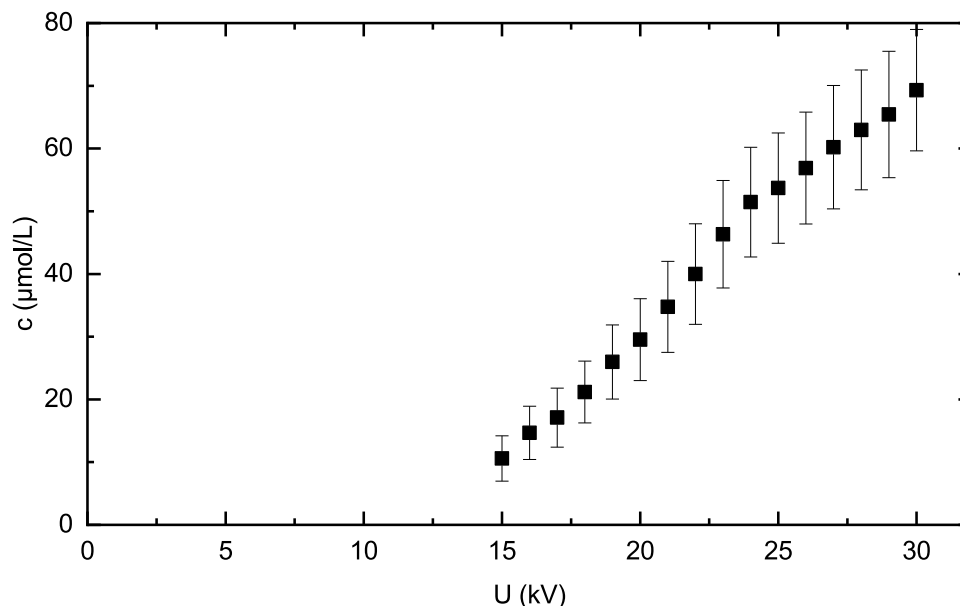


Figure 4.5.1: H_2O_2 concentration as a function of applied voltage with constant frequency of 15 Hz and 10 minutes treatment time. Adapted from [70].

more steep from 15 kV to 21 kV and a second one is more flat from 22-30 kV. H_2O_2 concentrations from 11 $\mu\text{mol/L}$ to 69 $\mu\text{mol/L}$ could be measured for the minimum and maximum applied voltages, respectively. During the whole measurement time of 160 min, it is observed that the length of the tungsten wire is decreasing due to small erosions of 2.5 mm. This leads to an erosion rate of 0.94 mm/h. This erosion could influence the energy dissipation into the discharge because an increasing distance between powered and grounded electrode should change the electric field strength.

Therefore, an additional variation of the electrode distance was performed to investigate the influence of the decreasing tungsten tip length on the H_2O_2 concentration. For a discharge ignited at 20 kV at 15 Hz with a liquid treatment time of 10 min, the distance between the electrodes was varied from 4.1 mm to 14.3 mm. The H_2O_2 concentrations are $37.5 \mu\text{mol/L}$ and $8 \mu\text{mol/L}$ for the minimum and maximum electrode distance, respectively. This can be linked to the variation of the electric field with changing electrode distance d : $E = -U/d$. The resistance $R = \rho d/A$ increases while d increases at constant applied voltage U . Therefore, the current I through the liquid must decrease according to Ohm's law $R = U/I$. For short electrode distances, the electric field and the current are higher compared to larger d . Hence, the dissipated power into the discharge should increase which can be quantified by the increasing H_2O_2 concentration at smaller distances. The larger dissipated energy also leads to a rise in temperature in the discharge which is correlated to an improved H_2O_2 production.

However, a small erosion of the electrode of 0.94 mm/h will not significantly influence the measurement of the H_2O_2 concentration because an intentional variation of the discharge by approximately 10 mm is leading to a change in concentration of about $30 \mu\text{mol/L}$. If this change is assumed to be linear, the erosion of about 1 mm is changing the concentration only by $3 \mu\text{mol/L}$ which lies within the error estimations.

In summary, the H_2O_2 concentration inside distilled water after plasma treatment increases with rising voltage and with smaller electrode distances. The small erosion rate of 0.94 mm/h has no significant influence on the production of H_2O_2 for one measurement of about 160 min.

4.5.2 Global chemistry model

It is not possible to measure the chemistry within the liquid during the discharge. Therefore, optical absorption spectroscopy is used to measure the H_2O_2 concentration inside distilled water after the discharge. The other created species are, however, not measured with this method. Furthermore, the discharge chemistry is left unidentified. Hence, a global chemistry model is applied to monitor the chemistry during the discharge and the following bubble expansion.

This model is adapted from the global chemistry model of Mededovic and Locke [69] describing a spark plasma with defined temperature zones of a hot plasma core and a cold recombination region [69, 123]. In comparison to the spark discharge, however, hot and cold regions are not separated in space but rather in time in the presented experiments. At high initial temperatures, the water gets dissociated into OH and H. The temperature drops and OH recombination to H_2O_2 starts during bubble expansion.

The set of reaction rates is listed in table C.2 in appendix C. These reaction rates can also be applied for the nanosecond plasma in liquid. The temperatures in the nanosecond plasma are assumed to be much higher than the temperature ranges within the set of reactions presented in table C. However, they can be used as an approximation, as the reaction rates at these high temperatures are dominated by the prefactor in the Arrhenius law. This is because the rate constant k is changing only slightly for high temperatures. Additionally, the temperature range given in table C.2 shows only the observation limit for experiments .

From the beginning of the discharge until the start of the cavitation bubble expansion, the pressures and temperatures are high which leads to efficient water dissociation. During the further expansion of the cavitation bubble the temperature drops until it reaches such small temperatures and pressures so that the chemistry is freezing inside the bubble. The total number of H_2O_2 species should stay constant after that. However, the decreasing rate of both, pressure and temperature, needs to be moderate in order to keep the three-body reaction rate of OH recombination for H_2O_2 production high enough.

For the global chemistry model, the starting conditions are taken from the cavitation model (section 4.4.2) and from the ideal gas law. The starting conditions of initial pressure $p_{0,gas}$, initial number of water molecules N_0 and initial temperature T_0 are:

- (i) $p_{0,gas}=10$ GPa for a discharge ignited at an applied voltage of 20 kV.
- (ii) N_0 estimated from the liquid water density ($n_{water} = 3 \cdot 10^{28} \text{m}^{-3}$) inside a spherical bubble with an initial radius of $R_0=25 \mu\text{m}$:

$$N_0 = n_{water} \cdot \left(\frac{4}{3}\pi R_0^3\right) = 2 \cdot 10^{15} \text{H}_2\text{O molecules.} \quad (4.38)$$

- (iii) $T_0 \approx 20000$ K estimated from the ideal gas law: $p_{0,gas}V_0 = N_0k_B T_0$.

In addition to these starting conditions it is assumed that the total number of all species does not change. The products OH, H_2O_2 , H, H_2 , O, O_2 and HO_2 are formed purely out of chemical reactions of H_2O .

Above this, a scaling factor $n_{scale} = p(t) T_0 / (T(t) p_{0,gas})$ is introduced to compensate the density decrease during bubble expansion, which affects the overall rate of two-body and three-body recombination. This coefficient scales with n_{scale}^2 and n_{scale}^3 for two-body and three-body recombinations, respectively. With all these conditions, the global chemical model can be applied which is illustrated in figure 4.5.2.

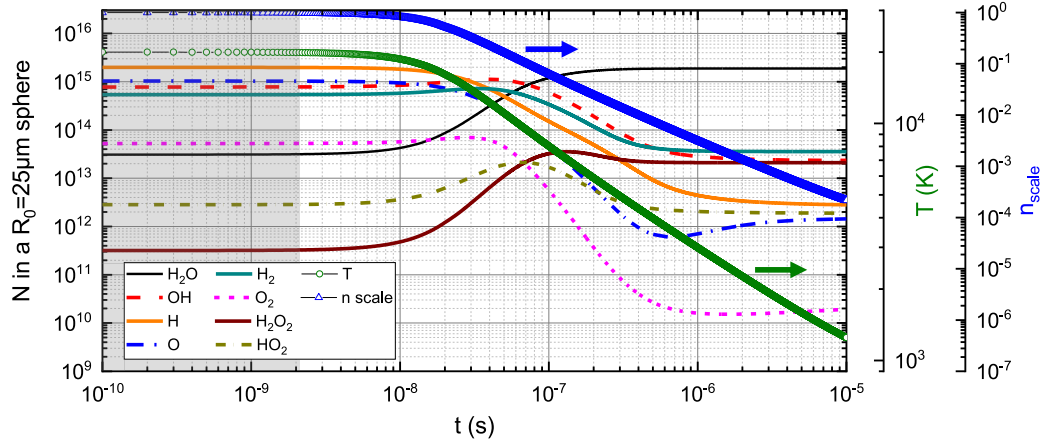


Figure 4.5.2: The solution of the global chemistry model with starting temperature $T_0=20000$ K and initial pressure $p_{0,gas}=10$ GPa. The grey area marks the time of the plasma pulse. Adapted from [70].

The global chemistry model shows a shift of the chemical equilibrium from water to H, OH, H_2 and O_2 during the 10 ns plasma pulse marked by the grey area. During this time, the water gets dissociated due to the dissipated energy and the resulting high temperature. After the plasma pulse, the cavitation bubble expands and the temperature drops rapidly. Simultaneously, the factor n_{scale} decreases due to the temperature and pressure drop. This process can be correlated to recombination during this phase: The number of OH species is dropping, whereas the number of H_2O_2 is increasing which indicates a recombination of two OH species to one H_2O_2 molecule. In addition, all other number of species decreases and the number of H_2O molecules is increasing again. The number of species does not change anymore at around $1 \mu s$ indicating a freezing of the chemistry inside the cavitation bubble. At this point, H_2 , OH, and H_2O_2 are the most dominant species.

The relation between different number of species can be expressed as molar ratios. These molar ratios are summarised in table 4.7.

Table 4.7: Molar ratios from global chemical model [70] after $10 \mu s$ compared to global kinetic model for spark discharge after one pulse from [69], table 7 of corrigendum.

author	$H_2 : H_2O_2$	$O_2 : H_2O_2$	OH : H_2O_2	$HO_2 : H_2O_2$
Chauvet et al. [70]	2:1	1:1000	1:1	1:10
Mededovic et al. [69]	2:1	1:1.5	1:3	1:3.5

The molar ratios of the nanosecond plasma and the spark discharge are different which can be explained by the temperature differences. The nanosecond

plasma starts with a much higher temperature and cools down quite fast during bubble expansion. The high starting temperature of 20000 K is leading to an efficient water dissociation compared to the hot core temperature of 5000 K of the spark plasma.

According to the nanosecond plasma global chemical model, water dissociation is most efficient above 10000 K with only little H₂ and O₂ generation. Additionally, the fast cooling of the chemistry inside the cavitation bubble limits the efficiency of back reactions and second-order reactions. These reactions, such as OH dissociation to O and H to form O₂ in a second step, are appearing on another time scale and are too slow for the fast freezing of the chemistry during bubble expansion.

This freezing of the chemistry inside the bubble is appearing at around 1 μs according to the model. This leads to the question, if the chemical species inside the cavitation bubble diffuse into the liquid and influence the liquid chemistry or not. Therefore, the Henry constant of each species should give insight into this question which are presented in table 4.8.

Table 4.8: Henry constants H for the different species in the global chemical model.

species	H ₂ O ₂	HO ₂	OH	H	H ₂	O ₂	O ₃
H (Pa/(mol·m ³))	$9 \cdot 10^2$	$3 \cdot 10^1$	$3 \cdot 10^{-1}$	10^{-6}	10^{-6}	10^{-5}	10^{-4}

The Henry constant of H₂O₂ is high compared to those of the other species. This indicates a complete solvation of the generated H₂O₂ from the cavitation bubble into the liquid during the whole process of expansion and bubble collapse at 100 μs. The measured data from the previous section is compared to the global chemical model. Figure 4.5.3 shows the concentration of H₂O₂ depending on the initial temperature for the measured data and the global chemical model.

For the latter, the concentration is calculated from the number of H₂O₂ species $N_{H_2O_2}$ in a constant initial volume V_0 . The initial temperature T_0 inside the bubble is changed in the experiment by varying the applied voltage leading to different energy dissipation in the system. The voltage $U_{applied}$ is then converted to a temperature via the ideal gas law with the dissipated power $E_{diss} = p_{0,gas}V_0$. This yields temperatures from 4000 K to 70000 K for applied voltages from 15 kV to 30 kV.

The comparison between model and data (solid line in figure 4.5.3(a)) shows good agreement except for the lowest and highest temperatures. There, the prediction from the global chemical model is underestimated. This discrepancy can be explained by the following points.

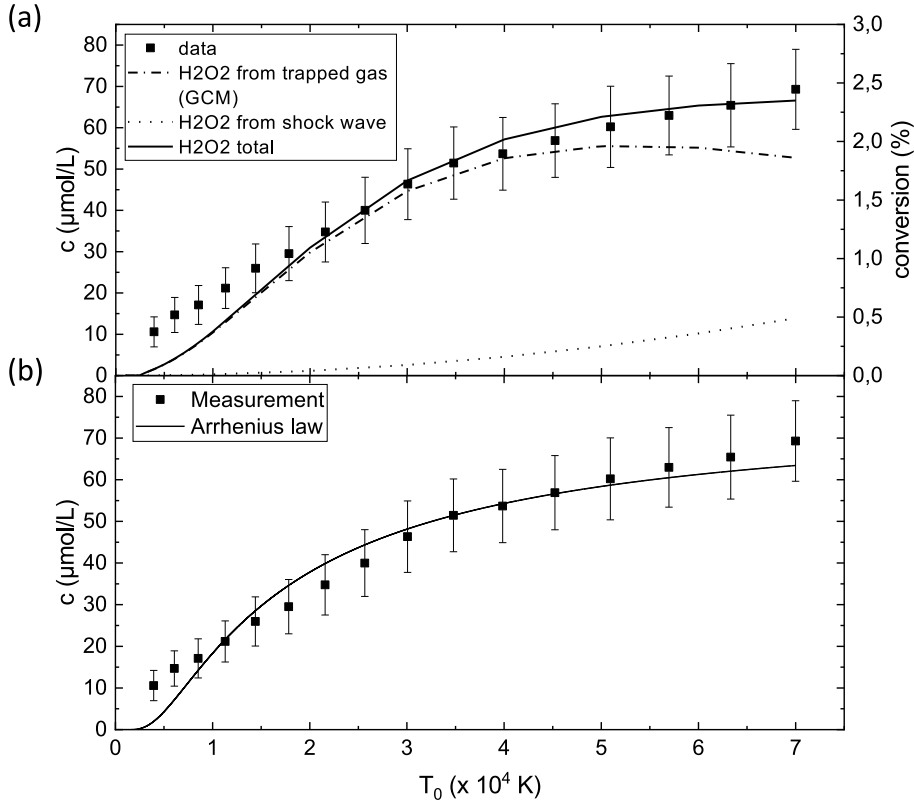


Figure 4.5.3: H₂O₂ concentration measured after plasma treatment depending on the initial temperature T_0 according to cavitation model compared with (a) H₂O₂ production from trapped gas inside bubble (dashed-dotted line), from the shock wave (dotted line) and the sum of both (solid line) and (b) H₂O₂ concentration compared with simple Arrhenius law (reaction enthalpy for H₂O₂ generation: 120.42 kJ/mol) (solid line). Adapted from [70].

Inaccuracies in rate coefficients: The main reaction for H₂O₂ creation is the recombination of OH ($OH + OH \rightarrow H_2O_2$). By setting this equation in the global chemistry model to zero, the concentration of H₂O₂ becomes negligible. At lower temperatures, the OH production could be underestimated due to an inefficient dissociation of H₂O disabling OH recombination to H₂O₂.

Inaccuracies in determination of T_0 : The estimation of the initial temperature is deduced from the dissipated energy into the discharge $E_0 = p_{0,gas}V_0$ with a constant initial spherical volume with a radius of 25 μm . However, the volume could also depend on the applied power. A smaller ignition volume at lower applied voltages would require a higher initial pressure and therefore the same dissipated energy. Simultaneously, the

number of water molecules in this volume decreases which results in a higher initial temperature T_0 . This would lead to a shift of the concentrations on the temperature scale leading to a better fit of the global chemical model. However, this is a rough assumption and an independent method for T_0 determination is required in order to validate this hypothesis.

The gas temperature is difficult to determine from the emission spectra. In general, the gas temperature could be estimated from Doppler broadening. This broadening might be present but Stark broadening is dominant and covers possible contributions from Doppler broadening. Only the temperature of the hot tungsten surface could be determined from the continuum radiation to ≈ 7000 K.

Neglecting e^- induced reactions: The electrons generated during this nanosecond discharge have a lifetime in the picosecond range [86]. Therefore, directly during ignition, dissociative attachment of electrons can contribute to water dissociation. This could balance the underestimation of H_2O_2 concentration below initial temperatures of 18000 K.

Neglecting H_2O_2 production by sonochemistry: Another source of H_2O_2 production which is not taken into account for the global chemistry model is sonochemistry. The shock wave generated during plasma ignition deposits energy into the liquid during its propagation. This can then lead to H_2O_2 formation directly in the liquid. The energy of the shock wave is proportional to $p_{0,gas}^2$ which corresponds to a quadratic scaling of the shock wave energy with the initial temperature T_0 . If the additional H_2O_2 production is proportional to the deposited energy by sonochemistry, a scaling according to the dotted line in figure 4.5.3(a) is given. The contribution of this H_2O_2 production path is scaled arbitrarily so that the sum of the global chemical model and the sonochemistry (solid line in figure 4.5.3(a)) fits well with the data for temperatures above 50000 K.

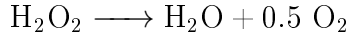
Despite all these approaches, the data seems to follow a simple Arrhenius reaction rate model (solid line in figure 4.5.3(b)). This model is based on a chemical equilibrium between forward and backward reactions inside the liquid. This is discussed in the following.

Global equilibrium model

The Arrhenius law describes the dependence on chemical reactions on the temperature for which a specific activation energy E_a is needed to be overcome for monomolecular reactions. The rate constant k in dependence on the temperature can be described as:

$$k = A \cdot e^{-\frac{E_a}{R \cdot T}}, \quad (4.39)$$

with the pre-factor A , the activation energy E_a , the gas constant $R = 8.314 \text{ J}/(\text{K mol})$ and the absolute temperature T . For the production of H_2O_2 the following reverse reaction is discussed:



The activation energy of this reaction corresponds to its free enthalpy of 120.42 kJ/mol . This energy can be converted into a temperature by dividing it by the gas constant R which results in a temperature of 14483 K . The concentration of H_2O_2 after a reaction time t can be described simply by:

$$c_{\text{H}_2\text{O}_2} = kt. \quad (4.40)$$

This can be combined with equation 4.39 resulting in:

$$c_{\text{H}_2\text{O}_2} = t A \cdot e^{-\frac{14483}{T}}. \quad (4.41)$$

This equation is applied for comparison with the measured H_2O_2 concentration in figure 4.5.3(b). The best fit for $A=0.13$ is in good agreement with the data. This simple Arrhenius law might be correct at high temperatures because then, reaction barriers loose their importance.

The generation of H_2O_2 by the nanosecond plasma in distilled water seems to result in high concentrations. The concentration can be converted into a production efficiency per energy in units of g/kWh to make a qualitative statement about the H_2O_2 production. Therefore, the dissipated energy of a discharge with an applied voltage of 20 kV is estimated by the BCS measurements discussed in section 4.1.3. The energy is about 4.5 mJ which yields a product efficiency of 2 g/kWh . This is in good agreement with the typical range discussed in literature for these in-liquid plasmas. Grymonpre et al. reported a yield of 3.64 g/kWh for a pulsed corona discharge at 60 Hz inside a potassium chloride solution with a low electrical conductivity of $7 \mu\text{S/cm}$ [124].

Therefore, the nanosecond plasmas ignited inside liquid can be assumed to provide a very good H_2O_2 production efficiency but at the same time no O_2 formation. The highly dynamic character of the discharge with the broad range of temperatures reached over a short time of a few tens of microseconds leads to these high H_2O_2 concentration inside the distilled water. This H_2O_2 inside the liquid could for example be used in plasma-driven biocatalysis.

4.5. *CHEMISTRY GENERATED BY NANOSECOND PLASMA IN
LIQUID*

“One never notices what has been done; one can only see what remains to be done.”

Marie Curie

5 | Summary and conclusion

In this work, the complex and highly dynamic nature of nanosecond pulsed plasmas inside distilled water is monitored and investigated. Especially the short rising times of only a few nanoseconds give the plasma its unique behaviour. These short time scales make it challenging to observe the exact time resolved behaviour of the discharge as well as measuring the generation of species inside the discharge and the liquid. This work is a first attempt to get an overall picture of the different processes on the discharge and post-discharge time scale.

The measurement of the voltage pulse inside the cable revealed multiple reflections due to a mismatched impedance at the plasma and the HV plugs before the discharge cell. Furthermore, the BCS measurements showed that only a small fraction of power is dissipated into the discharge in the order of a few mJ. The reflected pulses, however, provide reoccurring power input with each reflected pulse. The measured signal is only monitoring the voltage pulse at the position of the BCS. The real voltage applied at the electrode can be reconstructed from the initial and reflected pulses. This gives peak voltages approximately double the size of the measured BCS signal. Therefore, an even higher electric field is present at the electrode tip than the electric field assumed simply from the voltage pulse measured at the BCS.

The ignition of the nanosecond discharge inside distilled water was investigated. This is a highly discussed topic, because the ignition appears on such short time scales and in such small dimensions that it cannot be observed directly. Therefore, modelling is a helpful tool to analyse this process. With that, the assumption of nanopore formation due to a negative pressure gradient in tip vicinity during the rising edge of the voltage pulse was investigated in literature. In addition to that, this work also proposes that the generation of the first electrons leading to ignition is initiated by field effects, either as field emission or field ionisation depending on pulse polarity. Future experiments could analyse this by using a negative pulsed power supply with the exact same electrical characteristics (except pulse polarity). The field effects are assumed to appear for this discharges due to the high electric field at the electrode tip, or more precisely, at the protrusions on the electrode tip surface. The electric field strength exceeds the threshold for field emission

and field ionisation and therefore this should lead to electron tunneling into the liquid and towards the electrode, respectively. The choice of electrode material is also crucial. The structure of fine protrusions on the electrode tip is visible for tungsten, but is not present for all materials. This needs to be investigated further to correlate possible field effects with different electrode materials.

Optical diagnostics, such as ICCD imaging and optical emission spectroscopy, were applied to monitor the behaviour of the discharge and the spectroscopic line composition of its emission in a time-resolved manner. The accumulated light intensity of the ICCD images for each time step revealed a close correlation between voltage pulse and light emission. Two intensity peaks were observed during the rising and the falling edge of the voltage pulse. The ‘dark phase’ correlated to the plateau of the pulse could also be resolved showing a strong decrease in intensity. These findings are consistent with literature.

OES measurements were applied to gain time-resolved information of the spectral composition of the discharge from the ignition to the afterglow. Two cameras with different gate times were used for resolving the short time scales of ignition and discharge (2 ns gate time) and the longer time scales of afterglow and re-ignition due to reflected pulses inside the cable (30 ns gate time). The monitoring of the ignition revealed a broadband continuum which shifts to lower wavelengths with increasing time. This continuum radiation is associated with black body emission of the hot tungsten wire. Additionally, a hot spot can form on the tungsten surface contributing to the high energetic part of the continuum. As an alternative, radiation from radiative transitions can also result in very similar continuum contributions. Supposingly, both processes take place. However, the most dominant process needs to be revealed by increasing the UV sensitivity of the setup. Therefore, it can be distinguished whether the high energetic radiation is decreasing at smaller wavelengths again (black-body radiation) or if it keeps increasing towards smaller wavelengths (radiative transitions).

Strong broadening of emission lines was observed during the discharge phase as well as self-absorption for the early times of the discharge. The spectra could be well fitted by a two-region model consisting of an ionisation front (streamer head) and a recombination region (streamer channel). The general discharge propagation is assumed to be similar to discharges in gases. The large broadening of the emission lines of the H-Balmer series is induced by Stark broadening resulting from high electron densities. A maximum of electron density at the maximum voltage amplitude of $4.5 \cdot 10^{25} \text{ m}^{-3}$ is reached. The magnitude of the electron density is in good agreement with similar experiments in literature.

On longer time scales, the emission of the discharge and its afterglow is re-occurring for each reflected pulse inside the cable, but with lower amplitudes until the electric field is too weak for a discharge to ignite again. Hence, the dissipated power is less for the re-ignited discharge which results in decreased emission intensity and lower electron densities. It is assumed that the ignition physics also changes for the re-occurring pulses, because the first pulse is leaving a gaseous environment in the vicinity of the electrode tip instead of the pure liquid environment for the first pulse.

After the discharge disappeared, a cavitation bubble forms right after ignition which is monitored by shadowgraphs. An acoustic wave propagates through the medium away from the cavitation bubble. This wave is generated due to the high pressures in the range of tens of GPa at the time of ignition. The conclusions on this initial pressure can be drawn from analysing the wave velocity. Through extrapolation, initial acoustic wave velocities of 6-10 km/s were found for different applied voltages resulting in initial pressures of 15-45 GPa.

An agreement between model and measurement of the evolution of the cavitation bubble radius is found for an initial cavitation bubble radius of 25 μm and an initial temperature of 1200 K. Furthermore, the model shows that condensation should take place which leads to a fast drop in pressure inside the cavitation bubble. This process can be observed in shadowgraphs indicated by the change of contrast between 44-144 ns after the discharge. The initial pressure inside the bubble depends on the applied voltage and, therefore, on the dissipated power. Together with an ignition model indicating that the 25 μm radius cavitation bubble is formed in the first 14 ns, an overall picture of the discharge evolution from ignition to the collapse of the cavitation bubble was developed, combining experimental results and modelling.

The production of H_2O_2 was measured with optical absorption spectroscopy based on a calorimetric method. The H_2O_2 concentration for applied voltages between 15-30 kV ranges from 11-69 $\mu\text{mol/L}$ for a fixed frequency and treatment time of 15 Hz and 10 min, respectively. The measurements were then benchmarked with a global chemistry model describing the temporal evolution of different products created by the nanosecond discharge. The dependence of the H_2O_2 concentration of the initial temperature used in the model is similar to an Arrhenius law. Concluding, a product efficiency of H_2O_2 of 2 g/kWh can be achieved for a dissipated power of 4.5 mJ corresponding to an applied voltage of 20 kV. The use of the H_2O_2 produced by the nanosecond discharge for example in biocatalysis needs to be examined further.

In summary, the nanosecond discharge inside distilled water was investigated in depth showing the complex nature of this unique plasma igniting on very

short time scales in a liquid environment. The physics of this plasma is rather complex due to the different media of solid electrode tips, liquid propagation media and gaseous streamer channels as well as cavitation bubbles formed during and after the discharge. Therefore, not only the plasma physics of the discharge was addressed by determining the electron density from spectroscopic measurements and correlating the emission to the electrical properties, but also solid state physics and quantum physics such as electron tunneling from the solid electrode tip into the discharge through distorted potential barriers was depicted. This even enhances the complexity of these plasmas and makes them a fascinating object of research.

“The future interests me - I'm going to spend the rest of my life there.”

Mark Twain

6 | Outlook

In future, plasmas inside liquids can be used for a variety of applications. Next to their promising use in medicine, they can be combined with the fields of biology for biocatalysis and chemistry for CO₂ reduction via plasma electrolysis at catalytic surfaces.

In general, biocatalysis can be used to create valuable compounds by converting a precursor reacting with an enzyme to a valuable product, such as ibuprofene. For the reaction between enzyme and precursor, H₂O₂ is needed. However, the use of plasma treatment for H₂O₂ production usually inactivates the enzyme which disables the catalytic reaction [125]. Therefore, an immobilisation of enzymes through binding them to a carrier is investigated and this so-called beads show many positive effects. The beads can be used and re-used many times and through their higher mass, the enzyme-carrier combination are dragged down by gravity. For a plasma in liquid setup, the latter would be beneficial as the short-living aggressive species could not inactivate the carrier-bound enzyme. Then the more stable H₂O₂ created during the discharge could be used for the catalytic reactions leading to valuable products.

Additionally, discharges in liquids could be a useful application for environmental purposes. With their high production rate of radicals, these discharges can be used for plasma electrolysis combined with in-liquid CO₂ reduction reaction (CO₂RR) at catalytic surfaces to efficiently reduce CO₂ to more valuable compounds as for example ethanol. The principle of combining plasma electrolysis and surface catalysis may allow for a long lifetime of the catalytic surfaces, which usually get deactivated during longer use.

First measurements have been performed for investigating the influence of plasmas in liquids on catalytic surfaces, used for electrochemistry. Nanosecond discharge treatment of electropolished Cu foils in distilled water ($\sigma_{H_2O} = 5 \mu\text{S}/\text{cm}$) ignited at 16 kV with a frequency of 15 Hz showed a surface modification as shown in figure 6.0.1. The Cu foils were 99.9999% pure Cu from Sigma Aldrich cut into a 3x0.5 mm size and then electropolished in 85% ortho-phosphoric acid for 5 minutes at 3 V with subsequent rinsing in Milli-Q water (18 M Ω). Cubic structures have developed during the in-liquid plasma

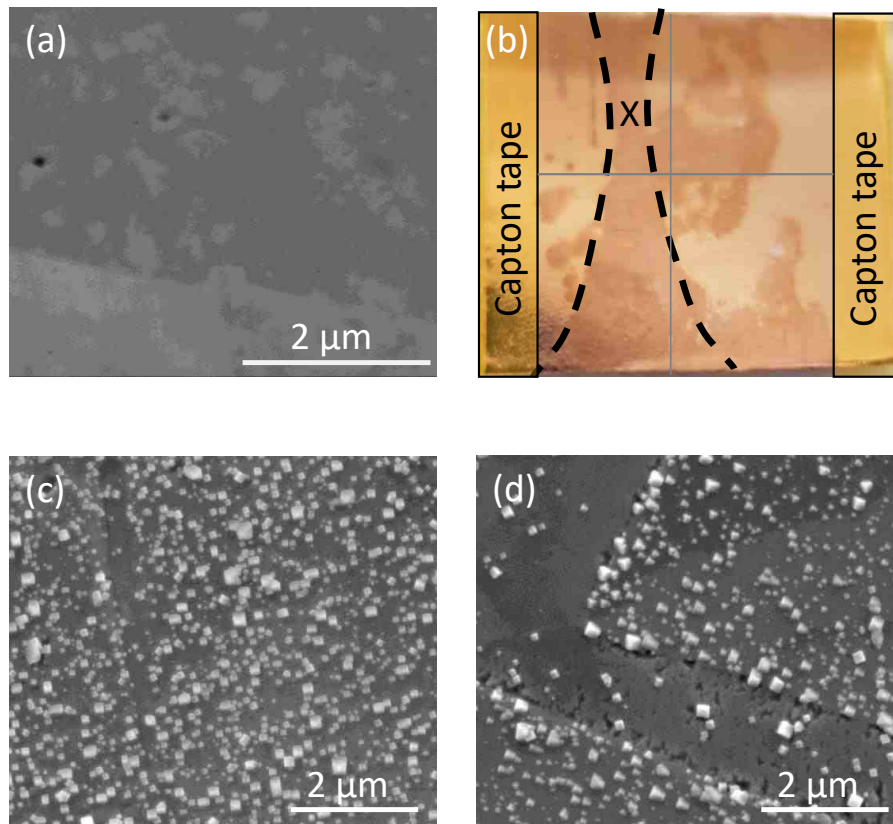


Figure 6.0.1: SEM images of electropolished Cu foil (a) before plasma treatment and (c),(d) after plasma treatment. An image of the treated electropolished Cu foil is shown in (b) with the ‘X’ indicating the position of the plasma in front of the Cu foil and the grey cross dividing the Cu foil in four quarters for orientation. The SEM image in (c) is taken in the upper left quarter and (d) is taken in the lower left quarter. SEM images taken by P. Grosse, FHI Berlin.

treatment of the electropolished Cu foil. These structures look very similar to CuO_x nanocubes, reported in literature [126]. Unfortunately, these measurements could not be reproduced until now. Therefore, it could be assumed that the discharge chamber could be contaminated from previous measurements with NaCl solutions, which could enhance the growth of CuO_x structures on the surface. However, the cubic structure of the particles is a strong indicator that these are CuO_x nanocubes as they preferably form in such a cubic form. Nevertheless, these treatments have been performed in order to monitor a general influence of the discharge on the Cu foil surface.

The aim is to use discharges in electrolytes to combine plasma and electrochemistry. Therefore, the 16 kV discharge at 15 Hz has also been tested in

0.1 M KHCO_3 solution. However, it was not possible to ignite the discharge in this solution which could result from the admixture of 0.1 M KHCO_3 , which increases the electrical conductivity. The resulting electric field might be too weak for a discharge to ignite. Only a lower concentration of KHCO_3 in the solution of 0.0035 M KHCO_3 made it possible to ignite the nanosecond discharge.

The liquid solution of 0.0035 M KHCO_3 without plasma treatment showed a modification of the exposed electropolished Cu foil. With increasing exposure time, a thicker nanoparticle layer formed on the surface but not in cubic structures. With plasma treatment, the surface roughness decreases with less pronounced areas of nanoparticle formation. But in conclusion, no clear trend and nanoparticle formation parameters could be determined.

Therefore, the treatment with nanosecond discharges in liquids is compared to μs pulsed discharges in liquid. The latter is characterised by longer pulses increasing the treatment time of the exposed surfaces. Also the chemistry could be different, because μs pulsed discharges tend to develop in cavitation bubbles generated before ignition due to their long pulse rise times. The pulse is approximately $5\ \mu\text{s}$ long with a rising time of several hundreds of ns. It is possible to ignite a plasma at 37.5 kV in 0.1 M KHCO_3 solution with these pulses. First measurements with electropolished Cu foils are shown in figure 6.0.2.

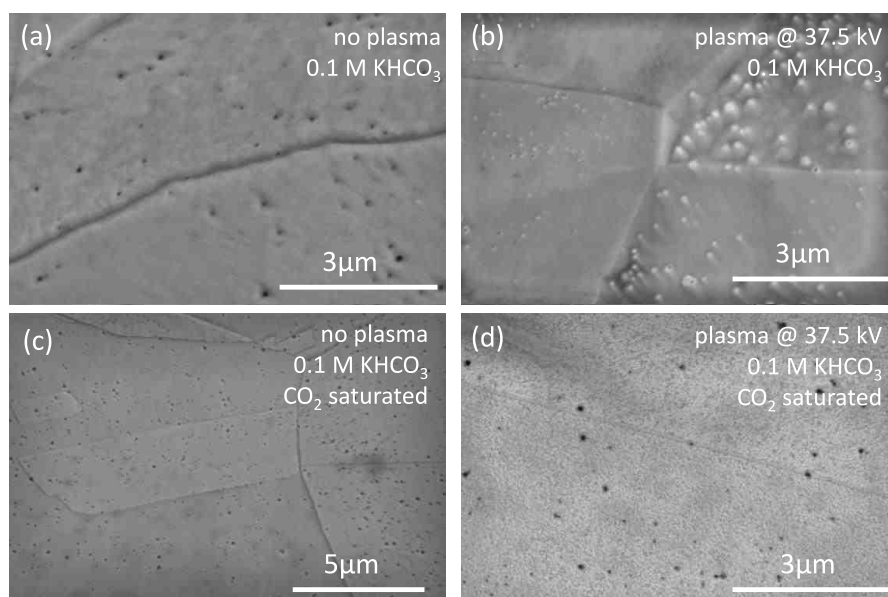


Figure 6.0.2: SEM images of electropolished Cu foil (a),(c) before and after (b),(d) a μs plasma treatment in 0.1 M KHCO_3 solution. The solution has been (a),(b) degassed and (c),(d) CO_2 saturated.

The surface structure seems to show only small changes. However, this measurement has not been performed with electrode distance variation, frequency variation and surface-plasma distance variation which all have an impact on surface modifications as shown in [127]. Furthermore, only unused, electropolished foils have been treated. The main goal is to increase the activity of CuO_x catalytic surfaces which have been used for CO_2RR in electrochemical cells. If the treatment of discharges in liquids increases the activity of used catalytic surfaces, an implementation of such a discharge into an electrochemical cell would be the next step. A prototype cell is in preparation. In conclusion, these in-liquid plasmas are a promising candidate among the applications for reducing excess CO_2 in the atmosphere by saturating the CO_2 into the treated liquid/electrolyte.

Bibliography

- [1] M. Moisan, J. Barbeau, M.-C. Crevier, J. Pelletier, N. Philip, and B. Saoudi, "Plasma sterilization. Methods and mechanisms," *Pure and Applied Chemistry*, vol. 74, pp. 349–358, Jan. 2002.
- [2] H. Baxter, G. Campbell, P. Richardson, A. Jones, I. Whittle, M. Casey, A. Whittaker, and R. Baxter, "Surgical Instrument Decontamination: Efficacy of Introducing an Argon:Oxygen RF Gas-Plasma Cleaning Step as Part of the Cleaning Cycle for Stainless Steel Instruments," *IEEE Transactions on Plasma Science*, vol. 34, pp. 1337–1344, Aug. 2006.
- [3] H. Akiyama, "Streamer discharges in liquids and their applications," *IEEE Transactions on Dielectrics and Electrical Insulation*, vol. 7, no. 5, pp. 646–653, 2000.
- [4] B. Jiang, J. Zheng, S. Qiu, M. Wu, Q. Zhang, Z. Yan, and Q. Xue, "Review on electrical discharge plasma technology for wastewater remediation," *Chemical Engineering Journal*, vol. 236, pp. 348–368, 2014.
- [5] M. Tichonovas, E. Krugly, V. Racys, R. Hippler, V. Kauneliene, I. Stasiulaitiene, and D. Martuzevicius, "Degradation of various textile dyes as wastewater pollutants under dielectric barrier discharge plasma treatment," *Chemical Engineering Journal*, vol. 229, pp. 9–19, Aug. 2013.
- [6] A. EL-Tayeb, A. EL-Shazly, M. Elkady, and A. Abdel-Rahman, "Simulation and Experimental Study for Degradation of Organic Dyes Using Dual pin-to-plate Corona Discharge Plasma reactors for Industrial Wastewater Treatment: Simulation and Experimental Study for Degradation of Organic Dyes Using Dual pin-to-plate Corona Discharge Plasma reactors for Industrial Wastewater T," *Contributions to Plasma Physics*, vol. 56, pp. 855–869, Oct. 2016.
- [7] W.-T. Shin, S. Yiacoumi, C. Tsouris, and S. Dai, "A Pulseless Corona-Discharge Process for the Oxidation of Organic Compounds in Water," *Industrial & Engineering Chemistry Research*, vol. 39, pp. 4408–4414, Sept. 2000.

- [8] M. A. Malik, A. Ghaffar, and S. A. Malik, "Water purification by electrical discharges," *Plasma Sources Science and Technology*, vol. 10, pp. 82–91, Feb. 2001.
- [9] W. H. Glaze, "Drinking-water treatment with ozone," *Environmental Science & Technology*, vol. 21, pp. 224–230, Mar. 1987.
- [10] H. Wang, "Effect of activated carbon addition on H₂O₂ formation and dye decoloration in a pulsed discharge plasma system," *Vacuum*, vol. 128, p. 7, 2016.
- [11] N. Saksono, T. Batubara, and S. Bismo, "Hydrogen production by plasma electrolysis reactor of KOH-ethanol solution," *IOP Conference Series: Materials Science and Engineering*, vol. 162, p. 012010, Nov. 2016.
- [12] P. Estifae, X. Su, S. K. Yannam, S. Rogers, and S. M. Thagard, "Mechanism of E. coli Inactivation by Direct-in-liquid Electrical Discharge Plasma in Low Conductivity Solutions," *Scientific Reports*, vol. 9, p. 2326, Dec. 2019.
- [13] L. Marsili, S. Espie, J. G. Anderson, and S. J. MacGregor, "Plasma inactivation of food-related microorganisms in liquids," *Radiation Physics and Chemistry*, vol. 65, pp. 507–513, Nov. 2002.
- [14] B. Geavlete, F. Stanescu, C. Iacoboaie, and P. Geavlete, "Bipolar plasma enucleation of the prostate vs open prostatectomy in large benign prostatic hyperplasia cases - a medium term, prospective, randomized comparison: Bipolar plasma enucleation vs open prostatectomy," *BJU International*, vol. 111, pp. 793–803, May 2013.
- [15] G. Fridman, G. Friedman, A. Gutsol, A. B. Shekhter, V. N. Vasilets, and A. Fridman, "Applied Plasma Medicine," *Plasma Processes and Polymers*, vol. 5, pp. 503–533, Aug. 2008.
- [16] K. D. Weltmann, E. Kindel, T. von Woedtke, M. Hähnel, M. Stieber, and R. Brandenburg, "Atmospheric-pressure plasma sources: Prospective tools for plasma medicine," *Pure and Applied Chemistry*, vol. 82, pp. 1223–1237, Apr. 2010.
- [17] A. A. Ashkarran, "A novel method for synthesis of colloidal silver nanoparticles by arc discharge in liquid," *Current Applied Physics*, vol. 10, pp. 1442–1447, Nov. 2010.
- [18] N. Sano, "Formation of multi-shelled carbon nanoparticles by arc discharge in liquid benzene," *Materials Chemistry and Physics*, vol. 88, pp. 235–238, Dec. 2004.

BIBLIOGRAPHY

- [19] P. Bruggeman and C. Leys, “Non-thermal plasmas in and in contact with liquids,” *Journal of Physics D: Applied Physics*, vol. 42, p. 053001, Mar. 2009.
- [20] S. Whitehead and E. B. Wedmore, *Dielectric Phenomena : Electrical Discharges in Liquids*. London: Ernest Benn Ltd., 1928.
- [21] M. Pekker and M. N. Shneider, “Initial stage of cavitation in liquids and its observation by Rayleigh scattering,” *Fluid Dynamics Research*, vol. 49, p. 035503, June 2017.
- [22] M. Shneider, M. Pekker, and A. Fridman, “Theoretical study of the initial stage of sub-nanosecond pulsed breakdown in liquid dielectrics,” *IEEE Transactions on Dielectrics and Electrical Insulation*, vol. 19, pp. 1579–1582, Oct. 2012.
- [23] H. M. Jones and E. E. Kunhardt, “Development of pulsed dielectric breakdown in liquids,” *J. Phys. D: Appl. Phys.*, vol. 28, no. 178, p. 12, 1995.
- [24] T. Lewis, “Breakdown initiating mechanisms at electrode interfaces in liquids,” *IEEE Transactions on Dielectrics and Electrical Insulation*, vol. 10, pp. 948–955, Dec. 2003.
- [25] M. N. Shneider and M. Pekker, “Dielectric fluid in inhomogeneous pulsed electric field,” *Physical Review E*, vol. 87, Apr. 2013.
- [26] M. N. Shneider and M. Pekker, “Pre-breakdown processes in a dielectric fluid in inhomogeneous pulsed electric fields,” *Journal of Applied Physics*, vol. 117, p. 224902, June 2015.
- [27] D. V. Tereshonok, “Cavitation in liquid dielectric under nanosecond high-voltage impulse,” *Journal of Physics D: Applied Physics*, vol. 50, p. 015603, Jan. 2017.
- [28] D. V. Tereshonok, N. Y. Babaeva, G. V. Naidis, V. A. Panov, B. M. Smirnov, and E. E. Son, “Pre-breakdown phenomena and discharges in a gas-liquid system,” *Plasma Sources Science and Technology*, vol. 27, p. 045005, Apr. 2018.
- [29] A. Starikovskiy, Y. Yang, Y. I. Cho, and A. Fridman, “Non-equilibrium plasma in liquid water: Dynamics of generation and quenching,” *Plasma Sources Science and Technology*, vol. 20, p. 024003, Apr. 2011.
- [30] Y. Seepersad, M. Pekker, M. N. Shneider, D. Dobrynin, and A. Fridman, “On the electrostrictive mechanism of nanosecond-pulsed breakdown in liquid phase,” *Journal of Physics D: Applied Physics*, vol. 46, p. 162001, Apr. 2013.

- [31] J. F. Kolb, R. P. Joshi, S. Xiao, and K. H. Schoenbach, "Streamers in water and other dielectric liquids," *Journal of Physics D: Applied Physics*, vol. 41, p. 234007, Dec. 2008.
- [32] M. Magureanu, D. Piroi, N. Mandache, V. David, A. Medvedovici, C. Bradu, and V. Parvulescu, "Degradation of antibiotics in water by non-thermal plasma treatment," *Water Research*, vol. 45, pp. 3407–3416, May 2011.
- [33] P. Šunka, "Pulse electrical discharges in water and their applications," *Physics of Plasmas*, vol. 8, pp. 2587–2594, May 2001.
- [34] W. An, K. Baumung, and H. Bluhm, "Underwater streamer propagation analyzed from detailed measurements of pressure release," *Journal of Applied Physics*, vol. 101, p. 053302, Mar. 2007.
- [35] K. Schoenbach, J. Kolb, S. Xiao, S. Katsuki, Y. Minamitani, and R. Joshi, "Electrical breakdown of water in microgaps," *Plasma Sources Science and Technology*, vol. 17, p. 024010, May 2008.
- [36] D. Dobrynin, Y. Seepersad, M. Pekker, M. Shneider, G. Fridman, and A. A. Fridman, "Non-equilibrium nanosecond-pulsed plasma generation in the liquid phase (water, PDMS) without bubbles: Fast imaging, spectroscopy and leader-type model," *Journal of Physics D: Applied Physics*, vol. 46, no. 10, p. 105201, 2013.
- [37] Y. Seepersad, A. Fridman, and D. Dobrynin, "Anode initiated impulse breakdown in water: The dependence on pulse rise time for nanosecond and sub-nanosecond pulses and initiation mechanism based on electrostriction," *Journal of Physics D: Applied Physics*, vol. 48, p. 424012, Sept. 2015.
- [38] M. Šimek, P. Hoffer, J. Tungli, V. Prukner, J. Schmidt, P. Bilek, and Z. Bonaventura, "Investigation of the initial phases of nanosecond discharges in liquid water," *Plasma Sources Science and Technology*, Apr. 2020.
- [39] R. Rataj, H. Höft, and J. F. Kolb, "Reillumination of submicrosecond pulsed corona-like discharges in water," *Plasma Sources Science and Technology*, vol. 28, p. 125002, Dec. 2019.
- [40] P. J. Bruggeman, M. J. Kushner, B. R. Locke, J. G. E. Gardeniers, W. G. Graham, D. B. Graves, R. C. H. M. Hofman-Caris, D. Maric, J. P. Reid, E. Ceriani, D. Fernandez Rivas, J. E. Foster, S. C. Garrick, Y. Gorbanev, S. Hamaguchi, F. Iza, H. Jablonowski, E. Klimova, J. Kolb, F. Krcma, P. Lukes, Z. Machala, I. Marinov, D. Mariotti, S. Mededovic Thagard, D. Minakata, E. C. Neyts, J. Pawlat, Z. L.

BIBLIOGRAPHY

- Petrovic, R. Pflieger, S. Reuter, D. C. Schram, S. Schröter, M. Shiraiwa, B. Tarabová, P. A. Tsai, J. R. R. Verlet, T. von Woedtke, K. R. Wilson, K. Yasui, and G. Zvereva, "Plasma-liquid interactions: A review and roadmap," *Plasma Sources Science and Technology*, vol. 25, p. 053002, Sept. 2016.
- [41] E. Spohr, "Molecular simulation of the electrochemical double layer," *Electrochimica Acta*, vol. 44, pp. 1697–1705, Jan. 1999.
- [42] Y. Seepersad, M. Pekker, M. N. Shneider, A. Fridman, and D. Dobrynin, "Investigation of positive and negative modes of nanosecond pulsed discharge in water and electrostriction model of initiation," *Journal of Physics D: Applied Physics*, vol. 46, p. 355201, Sept. 2013.
- [43] S. M. Korobeinikov, A. V. Melekhov, Y. N. Sinikh, and Y. G. Soloveichik, "Effect of Strong Electric Fields on the Behavior of Bubbles in Water," *High Temperature*, vol. 39, p. 5, June 2001.
- [44] V. Y. Shkadov and A. A. Shutov, "Drop and Bubble Deformation in an Electric Field," *Fluid Dynamics*, vol. 37, p. 12, Nov. 2002.
- [45] R. H. Fowler and L. W. Nordheim, "Electron emission in intense electric fields," *Royal Society*, vol. 119, pp. 173–181, May 1928.
- [46] R. Gomer, "Field emission and field ionization in condensed phases," *Accounts of Chemical Research*, vol. 5, pp. 41–48, Feb. 1972.
- [47] E. W. Plummer and A. E. Bell, "Field Emission Energy Distributions of Hydrogen and Deuterium on the (100) and (110) Planes of Tungsten," *Journal of Vacuum Science and Technology*, vol. 9, pp. 583–590, Mar. 1972.
- [48] M. Domke, G. Jähnig, and M. Drechsler, "Measurement of the adsorption energy on single crystal faces by field emission (hydrogen on tungsten)," *Surface Science*, vol. 42, pp. 389–403, Apr. 1974.
- [49] W. A. Schmidt, "Massenspektrometrische Untersuchung der Feldionisation von Wasserdampf an Spitzen aus Wolfram, Platin und Iridium," *Zeitschrift für Naturforschung A*, vol. 19, pp. 318–327, Mar. 1964.
- [50] H. M. Jones and E. E. Kunhardt, "Pulsed dielectric breakdown of pressurized water and salt solutions," *Journal of Applied Physics*, vol. 77, pp. 795–805, Jan. 1995.
- [51] D. R. Lide, G. Baysinger, S. Chemistry, L. I. Berger, R. N. Goldberg, and H. V. Kehiaian, "CRC Handbook of Chemistry and Physics," *CRC Press*, p. 2661, 2003.

-
- [52] X. Lu, Y. Pan, K. Liu, M. Liu, and H. Zhang, "Spark model of pulsed discharge in water," *J. Appl. Phys.*, vol. 91, p. 9, Dec. 2002.
- [53] V. S. Burakov, E. A. Nevar, M. I. Nedel'ko, N. A. Savastenko, and N. V. Tarasenko, "Spectroscopic diagnostics for an electrical discharge plasma in a liquid," *Journal of Applied Spectroscopy*, vol. 76, pp. 856–863, Nov. 2009.
- [54] P. H. Ceccato, O. Guaitella, M. R. Le Gloahec, and A. Rousseau, "Time-resolved nanosecond imaging of the propagation of a corona-like plasma discharge in water at positive applied voltage polarity," *Journal of Physics D: Applied Physics*, vol. 43, p. 175202, May 2010.
- [55] M. Šimek, M. Člupek, V. Babický, P. Lukeš, and P. Šunka, "Emission spectra of a pulse needle-to-plane corona-like discharge in conductive aqueous solutions," *Plasma Sources Science and Technology*, vol. 21, p. 055031, Oct. 2012.
- [56] B. Pongrác, M. Šimek, M. Člupek, V. Babický, and P. Lukeš, "Spectroscopic characteristics of H_{α} / O^I atomic lines generated by nanosecond pulsed corona-like discharge in deionized water," *Journal of Physics D: Applied Physics*, vol. 51, p. 124001, Mar. 2018.
- [57] R. P. Joshi and S. M. Thagard, "Streamer-Like Electrical Discharges in Water: Part I. Fundamental Mechanisms," *Plasma Chemistry and Plasma Processing*, vol. 33, pp. 1–15, Feb. 2013.
- [58] O. Lesaint, "Prebreakdown phenomena in liquids: Propagation 'modes' and basic physical properties," *Journal of Physics D: Applied Physics*, vol. 49, p. 144001, Apr. 2016.
- [59] M. Šimek, B. Pongrác, V. Babický, M. Člupek, and P. Lukeš, "Luminous phase of nanosecond discharge in deionized water: Morphology, propagation velocity and optical emission," *Plasma Sources Science and Technology*, vol. 26, p. 07LT01, June 2017.
- [60] I. Marinov, S. Starikovskaia, and A. Rousseau, "Dynamics of plasma evolution in a nanosecond underwater discharge," *Journal of Physics D: Applied Physics*, vol. 47, p. 224017, June 2014.
- [61] I. Marinov, O. Guaitella, A. Rousseau, and S. M. Starikovskaia, "Cavitation in the vicinity of the high-voltage electrode as a key step of nanosecond breakdown in liquids," *Plasma Sources Science and Technology*, vol. 22, p. 042001, June 2013.
- [62] A. Joshi, B. Locke, P. Arce, and W. Finney, "Formation of hydroxyl radicals, hydrogen peroxide and aqueous electrons by pulsed streamer corona discharge in aqueous solution," *Journal of Hazardous Materials*, vol. 41, pp. 3–30, Apr. 1995.

BIBLIOGRAPHY

- [63] T. Wang, H. Jia, X. Guo, T. Xia, G. Qu, Q. Sun, and X. Yin, "Evaluation of the potential of dimethyl phthalate degradation in aqueous using sodium percarbonate activated by discharge plasma," *Chemical Engineering Journal*, vol. 346, pp. 65–76, Aug. 2018.
- [64] A. J. Swallow and A. Charlesby, *Radiation Chemistry of Organic Compounds: International Series of Monographs on Radiation Effects in Materials*. 2016.
- [65] Y. Cao, G. Qu, T. Li, N. Jiang, and T. Wang, "Review on reactive species in water treatment using electrical discharge plasma: Formation, measurement, mechanisms and mass transfer," *Plasma Science and Technology*, vol. 20, p. 103001, Oct. 2018.
- [66] Jun Ma, Furong Wang, and Mehran Mostafavi, "Ultrafast Chemistry of Water Radical Cation, $\text{H}_2\text{O}^{\bullet+}$, in Aqueous Solutions," *Molecules*, vol. 23, p. 244, Jan. 2018.
- [67] L. C. Lei, Y. Zhang, X. W. Zhang, Y. X. Du, Q. Z. Dai, and S. Han, "Degradation Performance of 4-Chlorophenol as a Typical Organic Pollutant by a Pulsed High Voltage Discharge System," *Industrial & Engineering Chemistry Research*, vol. 46, pp. 5469–5477, Aug. 2007.
- [68] M. J. Kirkpatrick and B. R. Locke, "Effects of Platinum Electrode on Hydrogen, Oxygen, and Hydrogen Peroxide Formation in Aqueous Phase Pulsed Corona Electrical Discharge," *Industrial & Engineering Chemistry Research*, vol. 45, pp. 2138–2142, Mar. 2006.
- [69] S. Mededovic and B. R. Locke, "Primary chemical reactions in pulsed electrical discharge channels in water," *Journal of Physics D: Applied Physics*, vol. 42, pp. 049801–049801, Feb. 2009.
- [70] L. Chauvet, C. Nenbangkao, K. Grosse, and A. Keudell, "Chemistry in nanosecond plasmas in water," *Plasma Processes and Polymers*, Jan. 2020.
- [71] M. Dular and O. Coutier-Delgosha, "Thermodynamic effects during growth and collapse of a single cavitation bubble," *Journal of Fluid Mechanics*, vol. 736, pp. 44–66, Dec. 2013.
- [72] L. Rayleigh, "VIII. *On the pressure developed in a liquid during the collapse of a spherical cavity*," *The London, Edinburgh, and Dublin Philosophical Magazine and Journal of Science*, vol. 34, pp. 94–98, Aug. 1917.
- [73] Plesset, "The Dynamics of Cavitation Bubbles," *J Applied Mechanics*, p. 277, Sept. 1949.

- [74] F. Gilmore, "The growth or collapse of a spherical bubble in a viscous compressible liquid," Tech. Rep. 26-4, Hydrodynamic Laboratory, Caltech, Pasadena, California, 1952.
- [75] M. S. Plesset and A. Prosperetti, "Bubble Dynamics and Cavitation," *Ann. Rev. Fluid Mech.*, vol. 9, p. 145, 1977.
- [76] J. B. Keller and I. I. Kolodner, "Damping of Underwater Explosion Bubble Oscillations," *Journal of Applied Physics*, vol. 27, pp. 1152–1161, Oct. 1956.
- [77] J. B. Keller and M. Miksis, "Bubble Oscillations of Large Amplitude," *J. Acoust. Soc. Am.*, vol. 66, p. 628, Apr. 1980.
- [78] M. Greenspan and C. Tschiegg, "Speed of sound in water by a direct method," *Journal of Research of the National Bureau of Standards*, vol. 59, p. 249, Oct. 1957.
- [79] A. Vogel, S. Busch, and U. Parlitz, "Shock wave emission and cavitation bubble generation by picosecond and nanosecond optical breakdown in water," *The Journal of the Acoustical Society of America*, vol. 100, pp. 148–165, July 1996.
- [80] M. Kai, "Optical Analysis of a Nanosecond Plasma Inside Liquids," 2018.
- [81] H. R. Griem, *Principles of Plasma Spectroscopy*. Cambridge Monographs on Plasma Physics, Cambridge University Press, 2005.
- [82] R. D. Cowan and G. H. Dieke, "Self-Absorption of Spectrum Lines," *Reviews of Modern Physics*, vol. 20, pp. 418–455, Apr. 1948.
- [83] T. Stephens and A. Dalgarno, "Spontaneous radiative dissociation in molecular hydrogen," *Journal of Quantitative Spectroscopy and Radiative Transfer*, vol. 12, pp. 569–586, Apr. 1972.
- [84] B. P. Lavrov, A. S. Melnikov, M. Käning, and J. Röpcke, "Uv continuum emission and diagnostics of hydrogen-containing nonequilibrium plasmas," *Physical Review E*, vol. 59, pp. 3526–3543, Mar. 1999.
- [85] U. Fantz, B. Schalk, and K. Behringer, "Calculation and interpretation of the continuum radiation of hydrogen molecules," *New Journal of Physics*, vol. 2, pp. 7–7, Apr. 2000.
- [86] K. Grosse, J. Held, M. Kai, and A. von Keudell, "Nanosecond plasmas in water: Ignition, cavitation and plasma parameters," *Plasma Sources Science and Technology*, vol. 28, p. 085003, Aug. 2019.

BIBLIOGRAPHY

- [87] J. M. de Regt, J. van Dijk, J. A. M. van der Mullen, and D. C. Schram, “Components of continuum radiation in an inductively coupled plasma,” *Journal of Physics D: Applied Physics*, vol. 28, pp. 40–46, Jan. 1995.
- [88] L. M. Biberman, V. Vorobev, and L. Yakubov, “On the theory of ionization and recombination in a low-temperature plasma,” *Soviet Physics Jetp*, vol. 29, p. 1070, June 1969.
- [89] V. G. Artemov, A. A. Volkov, A. V. Pronin, and A. A. Volkov, “Electrical properties of water: A new insight,” *Biophysics*, vol. 59, pp. 520–523, Sept. 2014.
- [90] J. Bernardes and M. F. Rose, “Electrical Breakdown Characteristics of Sodium Chloride - Water Mixtures,” *4th IEEE Pulsed Power Conf. (Albuquerque, NM)*, p. 5, 1983.
- [91] H. Wang, R. J. Wandell, K. Tachibana, J. Voráč, and B. R. Locke, “The influence of liquid conductivity on electrical breakdown and hydrogen peroxide production in a nanosecond pulsed plasma discharge generated in a water-film plasma reactor,” *Journal of Physics D: Applied Physics*, vol. 52, p. 075201, Feb. 2019.
- [92] K. Kao, “Theory of High-Field Electric Conduction and Breakdown in Dielectric Liquids,” *IEEE Transactions on Electrical Insulation*, vol. EI-11, pp. 121–128, Dec. 1976.
- [93] K. Udagawa, S. Gorbato, F. Pliavaka, M. Nishihara, and I. Adamovich, “Experimental Study of a Fast Ionization Wave Discharge at High Pulse Repetition Rates,” in *46th AIAA Aerospace Sciences Meeting and Exhibit*, (Reno, Nevada), American Institute of Aeronautics and Astronautics, Jan. 2008.
- [94] M. Kotsonis, “Diagnostics for characterisation of plasma actuators,” *Measurement Science and Technology*, vol. 26, p. 092001, Sept. 2015.
- [95] H. C. Urey, L. H. Dawsey, and F. O. Rice, “The absorption spectrum and decomposition of hydrogen peroxide by light,” *Journal of the American Chemical Society*, vol. 51, pp. 1371–1383, May 1929.
- [96] D. R. Grymonpré, W. C. Finney, and B. R. Locke, “Aqueous-phase pulsed streamer corona reactor using suspended activated carbon particles for phenol oxidation: Model-data comparison,” *Chemical Engineering Science*, vol. 54, pp. 3095–3105, July 1999.
- [97] M. A. Gigosos, M. Á. González, and V. Cardeñoso, “Computer simulated Balmer-alpha, -beta and -gamma Stark line profiles for non-equilibrium plasmas diagnostics,” *Spectrochimica Acta Part B: Atomic Spectroscopy*, vol. 58, pp. 1489–1504, Aug. 2003.

-
- [98] V. Babicky, M. Clupek, and P. Lukes, "Determination of electrical characteristics of nanosecond discharge in liquid," in *2017 IEEE 19th International Conference on Dielectric Liquids (ICDL)*, (Manchester, United Kingdom), pp. 1–4, IEEE, June 2017.
- [99] P. Lukes, M. Clupek, V. Babicky, I. Sisrova, and V. Janda, "The catalytic role of tungsten electrode material in the plasmachemical activity of a pulsed corona discharge in water," *Plasma Sources Science and Technology*, vol. 20, p. 034011, June 2011.
- [100] A. R. Anway, "Field Ionization of Water," *The Journal of Chemical Physics*, vol. 50, pp. 2012–2021, Mar. 1969.
- [101] V. G. Andreev, V. A. Vdovin, and V. N. Kornienko, "Electrostrictive Mechanism of Liquid Breakdown in Strongly Nonhomogeneous Field under the Action of Nanosecond Voltage Pulse," *Journal of Communications Technology and Electronics*, vol. 63, pp. 908–914, Aug. 2018.
- [102] Y. Li, L. Li, J. Wen, J. Zhang, L. Wang, and G.-J. Zhang, "Towards an improved understanding of nanosecond-pulse discharge initiation in water: From cavitation to electron multiplication," *Plasma Sources Science and Technology*, June 2020.
- [103] E. Herbert, S. Balibar, and F. Caupin, "Cavitation pressure in water," *Physical Review E*, vol. 74, Oct. 2006.
- [104] Q. Zheng, D. J. Durben, G. H. Wolf, and C. A. Angell, "Liquids at Large Negative Pressures: Water at the Homogeneous Nucleation Limit," *Science*, vol. 254, pp. 829–832, Nov. 1991.
- [105] K. Grosse, V. Schulz-von der Gathen, and A. von Keudell, "Nanosecond pulsed discharges in distilled water: I. Continuum radiation and plasma ignition," *Plasma Sources Science and Technology*, vol. 29, p. 095008, Sept. 2020.
- [106] A. Bergner, F. H. Scharf, G. Kühn, C. Ruhrmann, T. Hoebing, P. Awakowicz, and J. Mentel, "Simulation of the hot core mode of arc attachment at a thoriated tungsten cathode by an emitter spot model," *Plasma Sources Science and Technology*, vol. 23, p. 054005, Sept. 2014.
- [107] H.-J. Kunze, *Introduction to Plasma Spectroscopy*. No. 56 in Springer Series on Atomic, Optical, and Plasma Physics, Berlin ; New York: Springer, 2009.
- [108] N. Konjević, M. Ivković, and N. Sakan, "Hydrogen Balmer lines for low electron number density plasma diagnostics," *Spectrochimica Acta Part B: Atomic Spectroscopy*, vol. 76, pp. 16–26, Oct. 2012.
- [109] H. Griem, *Plasma Spectroscopy*. McGraw-Hill, 1964.

BIBLIOGRAPHY

- [110] C. Allen, *Astrophysical Quantities*. New York: Athlone Press, 3rd ed. ed., 1973.
- [111] N. Konjević, “Plasma broadening and shifting of non-hydrogenic spectral lines: Present status and applications,” *Physics Reports*, vol. 316, pp. 339–401, Aug. 1999.
- [112] H. R. Griem, *Spectral Line Broadening by Plasmas*. Pure and Applied Physics 39, Academic Press, Inc, 1974.
- [113] A. von Keudell, K. Grosse, and V. Schulz-von der Gathen, “Nanosecond pulsed discharges in distilled water-Part II: Line emission and plasma propagation,” *Plasma Sources Science and Technology*, vol. 29, p. 085021, Sept. 2020.
- [114] V. A. Ankudinov, S. V. Bobashev, and E. P. Andreev, “Measurement of lifetimes of excited states of the hydrogen atom,” *Soviet Physics JETP*, vol. 21, p. 7, Jan. 1965.
- [115] H. R. Griem, “Shifts of hydrogen and ionized-helium lines from $\Delta n = 0$ interactions with electrons in dense plasmas,” *Physical Review A*, vol. 38, pp. 2943–2952, Sept. 1988.
- [116] D. B. Boercker and C. A. Iglesias, “Static and dynamic shifts of spectral lines,” *Physical Review A*, vol. 30, pp. 2771–2774, Nov. 1984.
- [117] K. Nagayama, Y. Mori, K. Shimada, and M. Nakahara, “Shock Hugoniot compression curve for water up to 1 GPa by using a compressed gas gun,” *Journal of Applied Physics*, vol. 91, p. 476, Jan. 2002.
- [118] M. H. Rice and J. M. Walsh, “Equation of State of Water to 250 Kilo-bars,” *The Journal of Chemical Physics*, vol. 26, pp. 824–830, Apr. 1957.
- [119] M. McLinden, E. Lemmon, and D. Friend, “Thermophysical Properties of Fluid Systems.,” Sept. 2018.
- [120] P. Lukeš, M. Člupek, V. Babický, P. Šunka, J. D. Skalný, M. Štefečka, J. Novák, and Z. Málková, “Erosion of needle electrodes in pulsed corona discharge in water,” *Czechoslovak Journal of Physics*, vol. 56, pp. B916–B924, Oct. 2006.
- [121] C. Nenbangkao, “Analysis of Hydrogen Peroxide Production in Nanosecond Pulsed Discharges in Water,” 2019.
- [122] E. Tutem, R. Apak, and F. Baykut, “Spectrophotometric Determination of Trace Amounts of Copper(I) and Reducing Agents With Neocuproine in the Presence of Copper(II),” *Analyst*, vol. 116, p. 6, 1991.

- [123] B. R. Locke and S. M. Thagard, "Analysis and Review of Chemical Reactions and Transport Processes in Pulsed Electrical Discharge Plasma Formed Directly in Liquid Water," *Plasma Chemistry and Plasma Processing*, vol. 32, pp. 875–917, Oct. 2012.
- [124] D. R. Grymonpré, A. K. Sharma, W. C. Finney, and B. R. Locke, "The role of Fenton's reaction in aqueous phase pulsed streamer corona reactors," *Chemical Engineering Journal*, vol. 82, pp. 189–207, Mar. 2001.
- [125] A. Yayci, Á. G. Baraibar, M. Krewing, E. F. Fueyo, F. Hollmann, M. Alcalde, R. Kourist, and J. E. Bandow, "Plasma-Driven in Situ Production of Hydrogen Peroxide for Biocatalysis," *ChemSusChem*, vol. 13, pp. 2072–2079, Apr. 2020.
- [126] D. Gao, I. Zegkinoglou, N. J. Divins, F. Scholten, I. Sinev, P. Grosse, and B. Roldan Cuenya, "Plasma-Activated Copper Nanocube Catalysts for Efficient Carbon Dioxide Electroreduction to Hydrocarbons and Alcohols," *ACS Nano*, vol. 11, pp. 4825–4831, May 2017.
- [127] F.-N. Seferoglu, "Surface modification of a copper substrate through the reaction chemistry generated by pulsed plasmas in water," 2019.
- [128] A. Kramida and Y. Ralchenko, "NIST Atomic Spectra Database, NIST Standard Reference Database 78," 1999.

Acknowledgements

Abschließend möchte ich mich ganz herzlich bei allen bedanken, die mich bei der Erstellung dieser Arbeit unterstützt haben. Die letzten Jahre waren eine spannende Zeit, die ich um nichts in der Welt missen möchte. Ein besonderer Dank geht an

... Prof. Dr. Achim von Keudell für die Möglichkeit, diese Dissertation am Lehrstuhl für Experimentalphysik 2 durchzuführen. Ich bin dankbar für alle Ideen, Fragen, Diskussionen und Kommentare während der vergangenen Jahre, die diese Arbeit vorangetrieben haben.

... Prof. Dr. Peter Awakowicz für die Übernahme der Zweitbetreuung und -korrektur, sowie den spannenden Diskussionen und dem Feedback während der Projekttreffen des SFB 1316.

... die Techniker des Lehrstuhls für Experimentalphysik 2, ohne die der experimentelle Aufbau nicht stehen und funktionieren würde. Ein besonderer Dank gilt Michael Konkowski, für seine Hilfe mit der komplizierten Elektrik dieses Aufbaus.

... alle Mitarbeiter des Lehrstuhls für Experimentalphysik 2, die immer hilfsbereit sind und für eine nette Atmosphäre am Lehrstuhl sorgen.

... Volker Schulz-von der Gathen für die guten Diskussionen über optische Aufbauten und die Analyse der Emissionsspektren.

... Julian Held für die Einführung und die tatkräftige Unterstützung mit den Spektrographen-Messungen, sowie der komplizierten Analyse der Spektren selbst.

... meine ehemaligen Bachelorstudentinnen Maike Kai und Fatma-Nur Seferoglu für die tolle Zusammenarbeit und ihren unermüdlichen Fleiß.

... Dr. Laura Chauvet und Chaiyasit Nenbankaeo für die sehr gelungenen optischen Absorptionsmessungen und die vielen hilfreichen Diskussionen.

... Dr. Marina Prenzel und Rahel Buschhaus, sowohl für das gründliche und hilfreiche Korrekturlesen, als auch für die aufbauenden Gespräche und die netten Kaffee-Runden.

... Sascha Thiemann-Monje für zahlreichen Tee-Runden, die Versuche uns zum Sport zu motivieren und die guten Gespräche.

... Patrick Preissing für die tolle Bürozeit und die entspannte Arbeitsatmosphäre.

... meinen Bruder Philipp Grosse für das Korrekturlesen dieser Arbeit und dem Beantworten aller chemischen Fragen, die währenddessen auftraten. Außerdem danke ich ihm für die Diskussionen und die gute gemeinsame Kooperation im Rahmen des SFB 1316.

... meine Eltern Bärbel und Karl Grosse, die mir das Studium ermöglicht und immer an mich geglaubt und mich unterstützt haben.

... Philip Laake, der mich immer aufgebaut hat, wenn die Arbeit zu viel wurde. Immer zugehört hat, wenn ich reden wollte. Und immer da war, wenn ich ihn brauchte.

Appendices

A | Line broadening calculations

Table A.1: Wavelength λ , statistical weight g_k times the Einstein coefficients A_{ik} , energies of lower level E_i and upper level E_k of transitions of H_α according to NIST data base [128].

$\lambda(nm)$	$g_k A_{ik}(s^{-1})$	$E_i(cm^{-1})$	$E_k(cm^{-1})$
656.270970	2.1551e+08	82 258.9191133	97 492.319433
656.272483	8.9792e+07	82 258.9543992821	97 492.319611
656.275181	4.2092e+06	82 258.9191133	97 492.221701
656.277153	4.4898e+07	82 258.9543992821	97 492.211200
656.2819	7.9382e+08	82 259.158	97 492.304
656.285177	3.8791e+08	82 259.2850014	97 492.355566
656.286734	4.3100e+07	82 259.2850014	97 492.319433
656.290944	8.4194e+06	82 259.2850014	97 492.221701

Table A.2: Wavelength λ , statistical weight g_k times the Einstein coefficients A_{ik} , energies of lower level E_i and upper level E_k of transitions of H_β according to NIST data base [128].

$\lambda(nm)$	$g_k A_{ik}(s^{-1})$	$E_i(cm^{-1})$	$E_k(cm^{-1})$
486.1278624	6.8752e+07	82 258.9191133	102 823.894250
486.1286949	3.8672e+07	82 258.9543992821	102 823.8943175
486.1288370	1.7188e+06	82 258.9191133	102 823.8530211
486.1297761	1.9337e+07	82 258.9543992821	102 823.8485825
486.1333	2.6942e+08	82 259.158	102 823.904
486.1361516	1.2375e+08	82 259.2850014	102 823.9094871
486.1365118	1.3750e+07	82 259.2850014	102 823.894250
486.1374864	3.4380e+06	82 259.2850014	102 823.8530211

Table A.3: Wavelength λ , statistical weight g_k times the Einstein coefficients A_{ik} , energies of lower level E_i and upper level E_k of transitions of H_γ according to NIST data base [128].

$\lambda(nm)$	$g_k A_{ik}(s^{-1})$	$E_i(cm^{-1})$	$E_k(cm^{-1})$
434.0426937	3.1419e+07	82 258.9191133	105 291.651993
434.0430904	8.5910e+05	82 258.9191133	105 291.63094
434.0433568	1.9793e+07	82 258.9543992821	105 291.65209
434.0437982	9.8968e+06	82 258.9543992821	105 291.62867
434.0471	1.2652e+08	82 259.158	105 291.657
434.0494419	5.6552e+07	82 259.2850014	105 291.659796
434.0495889	6.2836e+06	82 259.2850014	105 291.651993
434.0499857	1.7184e+06	82 259.2850014	105 291.63094

B | Time-resolved emission spectra

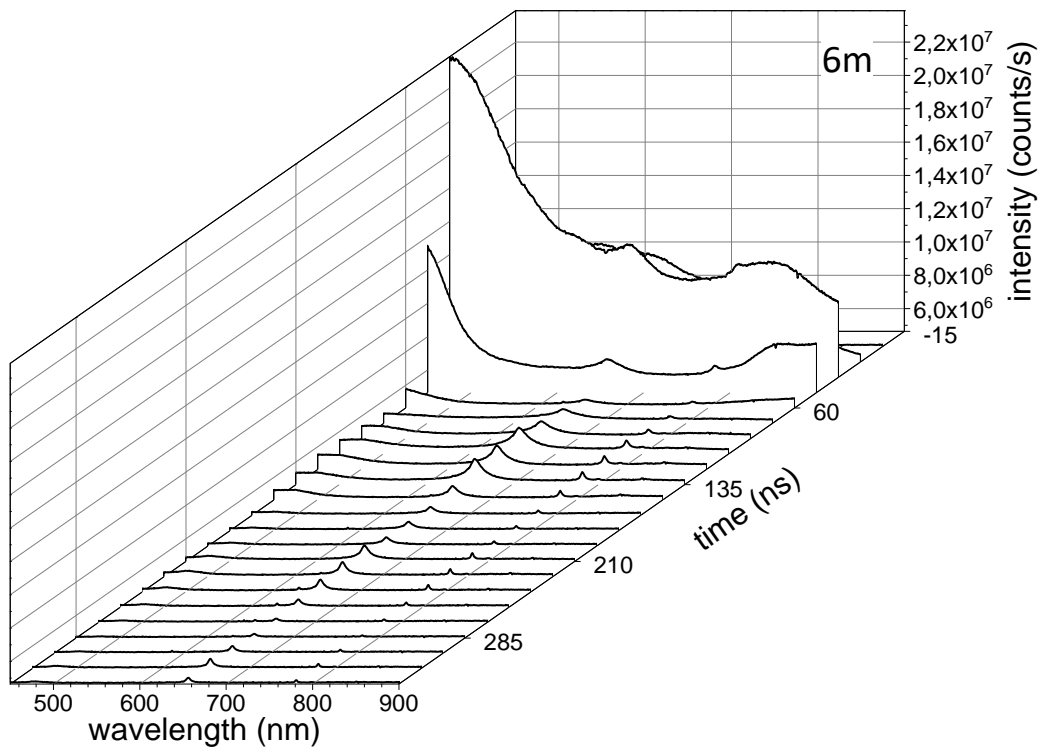


Figure B.0.1: Temporal evolution of optical emission spectra of 6 m long cable.

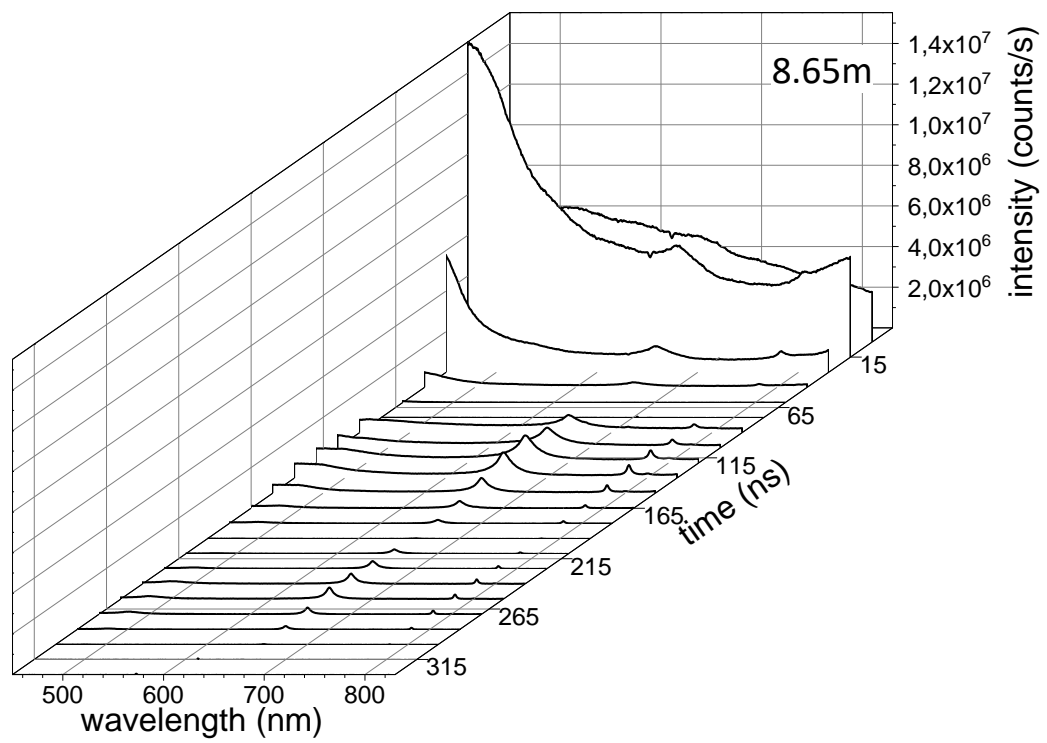


Figure B.0.2: Temporal evolution of optical emission spectra of 8.65 m long cable.

APPENDIX B. TIME-RESOLVED EMISSION SPECTRA

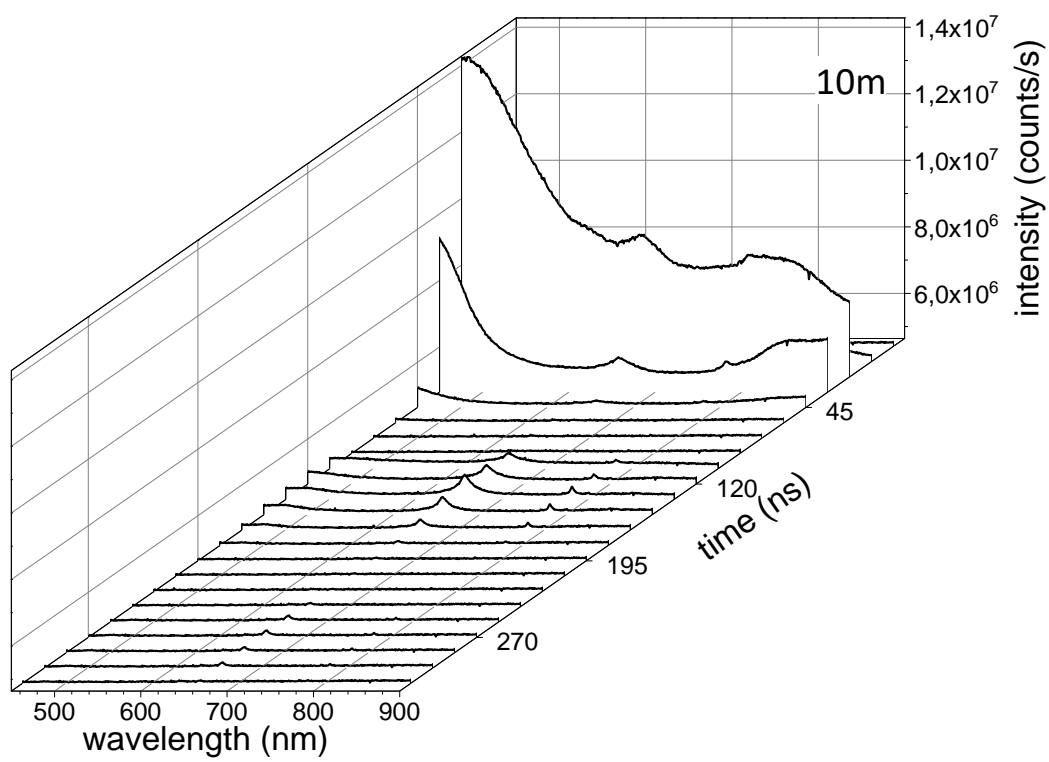


Figure B.0.3: Temporal evolution of optical emission spectra of 10 m long cable.

C | Global Chemistry Model

Table C.1: Temperatures and rate coefficients of the chemical reactions used in the global chemical model.

Reaction	Temperature	rate coefficient
H₂O reactions		
H ₂ O + M → H + OH + M	2000-6000 K	$k_{21} = 5.8 \cdot 10^{-9} \exp[-440000(RT)^{-1}]$
O₂ reactions		
O ₂ + M → O + O + M	200-10000 K	$k_{27} = 1.99 \cdot 10^{-10} \exp[-9500(RT)^{-1}]$
OH reactions		
OH + M → H + O + M	300-2500 K	$k_{22} = 4.09 \cdot 10^{-9} \exp[-416000(RT)^{-1}]$
OH + OH → H ₂ O + O	250-300 K	$k_{29} = 1.02 \cdot 10^{-12} (T/298)^{1.4} \exp[1660(RT)^{-1}]$
O + OH → O ₂ + H	250-5000 K	$k_{61} = 4.55 \cdot 10^{-12} (T/298)^{0.4} \cdot \exp[3090(RT)^{-1}]$
OH + H → H ₂ O	300-2100 K	$k_{62} = 2.69 \cdot 10^{-10} \exp[-620(RT)^{-1}]$
H + OH → O + H ₂	300-2500 K	$k_{63} = 6.68 \cdot 10^{-14} (T/298)^{2.8} \cdot \exp[-16210(RT)^{-1}]$
H ₂ O ₂ + OH → HO ₂ + H ₂ O	300-2500 K	$k_{64} = 2.91 \cdot 10^{-12} \cdot \exp[-1330(RT)^{-1}]$
O ₂ + OH → HO ₂ + O	300-2500 K	$k_{65} = 3.7 \cdot 10^{-11} \cdot \exp[-220000(RT)^{-1}]$
OH + OH → H ₂ O ₂	300-1500 K	$k_{66} = 1.51 \cdot 10^{-11} (T/298)^{-0.37}$
OH + OH → 2 O + 2H	300-2500 K	$k_{67} = 4.09 \cdot 10^{-9} \cdot \exp[-416000(RT)^{-1}]$
H₂O₂ reactions		
H ₂ O ₂ + O → HO ₂ + OH	300-2500 K	$k_{68} = 1.42 \cdot 10^{-12} (T/298)^2 \exp[-16631(RT)^{-1}]$
H ₂ O ₂ + H → OH + H ₂ O	300-2500 K	$k_{69} = 4.01 \cdot 10^{-11} \exp[-16630(RT)^{-1}]$
H ₂ O ₂ + H → HO ₂ + H ₂	300-2500 K	$k_{610} = 8 \cdot 10^{-11} \exp[-33260(RT)^{-1}]$
H ₂ O ₂ + O ₂ → 2 HO ₂	300-2500 K	$k_{611} = 9 \cdot 10^{-11} \exp[-166000(RT)^{-1}]$
HO₂ reactions		
HO ₂ + OH → H ₂ O + O ₂	300-2000 K	$k_{612} = 4.81 \cdot 10^{-11} \exp[2080(RT)^{-1}]$
HO ₂ + O → OH + O ₂	300-2500 K	$k_{613} = 2.91 \cdot 10^{-11} \exp[-1660(RT)^{-1}]$
HO ₂ + H → 2 OH	300-2500 K	$k_{614} = 2.81 \cdot 10^{-10} \exp[-3660(RT)^{-1}]$
HO ₂ + H → H ₂ + O ₂	300-2500 K	$k_{615} = 1.1 \cdot 10^{-10} \exp[-8900(RT)^{-1}]$
HO ₂ + HO ₂ → H ₂ O ₂ + O ₂	300-2500 K	$k_{616} = 3.01 \cdot 10^{-12}$
HO ₂ + H ₂ → H ₂ O ₂ + H	300-2500 K	$k_{617} = 5 \cdot 10^{-11} \exp[-109000(RT)^{-1}]$
HO ₂ + M → O ₂ + H + M	300-2200 K	$k_{618} = 2.41 \cdot 10^{-8} (T/298)^{-1.18} \exp[-2031000(RT)^{-1}]$
H reactions		
O + H + M → OH + M	300-2500 K	$k_{619} = 4.36 \cdot 10^{-32} (T/298)^{-1}$
H + H + M → M + H ₂	300-2500 K	$k_{620} = 6.04 \cdot 10^{-33} (T/298)^{-1}$
O ₂ + H → OH + O	500-2000 K	$k_{621} = 2.94 \cdot 10^{-10} \exp[-69680(RT)^{-1}]$
O ₂ + H + M → HO ₂ + M	200-2200 K	$k_{622} = 1.94 \cdot 10^{-32} (T/298)^{-1}$
H₂ reactions		
H ₂ + M → H + H + M	2500-8000 K	$k_{25} = 1.5 \cdot 10^{-9} \exp[-402000(RT)^{-1}]$
OH + H ₂ → H ₂ O + H	200-2400 K	$k_{623} = 2.97 \cdot 10^{-12} (T/298)^{1.21} \exp[-19710(RT)^{-1}]$
O + H ₂ → OH + H	300-2500 K	$k_{624} = 3.44 \cdot 10^{-13} (T/298)^{2.67} \exp[-26270(RT)^{-1}]$

O reactions		
$\text{O} + \text{O} + \text{M} \rightarrow \text{O}_2 + \text{M}$	200-4000 K	$k_{625} = 5.21 \cdot 10^{-35} \exp[7480(RT)^{-1}]$
$\text{O} + \text{H}_2\text{O} \rightarrow \text{OH} + \text{OH}$	300-2000 K	$k_{626} = 6.68 \cdot 10^{-13} (T/298)^{2.60} \exp[-63520(RT)^{-1}]$

Lebenslauf

Persönliche Daten

Name	Katharina Grosse
Geburtsdatum	17.05.1992
Geburtsort	Witten

Promotionsvorhaben

seit 03/2017	Promotionsvorhaben in der Physik an der Ruhr-Universität Bochum
seit 03/2017	Wissenschaftliche Mitarbeiterin am Lehrstuhl "Physik der reaktiven Plasmen", Ruhr-Universität Bochum

Studium

06/2014-11/2016	Studium der Physik (M.Sc.) an der Ruhr-Universität Bochum
09/2014-07/2015	Auslandssemester, University of York, York, Großbritannien
09/2011-06/2014	Studium der Physik (B.Sc.) an der Ruhr-Universität Bochum

Schulbildung

25.06.2011	Abitur
08/2002-06/2011	Geschwister-Scholl-Gymnasium, Wetter
08/1998-07/2002	Osterfeldschule, Wetter-Wengern

February 15, 2021